MANTAS LANDAUSKAS

APPLICATIONS OF *H*-RANKS IN NONLINEAR SYSTEMS AND CHAOS ANALYSIS

DAKTARO DISERTACIJA

Kaunas
2016

KAUNAS UNIVERSITY OF TECHNOLOGY

MANTAS LANDAUSKAS

APPLICATIONS OF *H*-RANKS IN NONLINEAR SYSTEMS AND CHAOS ANALYSIS

Doctoral dissertation
Physical sciences, Informatics (09P)

2016, Kaunas

UDK 530.182 + 517.938](043.3)

The research was accomplished during the period of 2011-2015 at Kaunas University of Technology, Faculty of Mathematics and Natural Sciences, Department of Mathematical Modelling. The research was supported by the Research Council of Lithuania.

Scientific Supervisor:
Prof. Dr. Habil. **Minvydas Kazys Ragulskis** (Kaunas University of Technology, Physical Sciences, Informatics – 09P).

Doctoral dissertation has been published in:
http://ktu.edu

The Lithuanian Language Editor:
Violeta Meiliūnaitė
Publishing house "Technologija"

The English Language Editor:
Armandas Rumšas
Publishing house "Technologija"

© M. Landauskas, 2016

ISBN 978-609-02-1187-8

KAUNO TECHNOLOGIJOS UNIVERSITETAS

MANTAS LANDAUSKAS

H-RANGŲ TAIKYMAI NETIESINIŲ SISTEMŲ IR CHAOSO TYRIMUOSE

Daktaro disertacija
Fiziniai mokslai, Informatika (09P)

2016, Kaunas

UDK 530.182 + 517.938](043.3)

Disertacija rengta 2011-2015 metais Kauno technologijos universiteto Matematikos ir gamtos mokslų fakultete Matematinio modeliavimo katedroje. Mokslinius tyrimus rėmė Lietuvos mokslo taryba.

Mokslinis vadovas:
Prof. habil. dr. **Minvydas Kazys Ragulskis** (Kauno technologijos universitetas, fiziniai mokslai, informatika – 09P).

Interneto svetainės, kurioje skelbiama disertacija, adresas:
http://ktu.edu

Lietuvių kalbos redaktorius:
Violeta Meiliūnaitė
Leidykla „Technologija“

Anglų kalbos redaktorius:
Armandas Rumšas
Leidykla „Technologija“

© M. Landauskas, 2016

ISBN 978-609-02-1187-8

TABLE OF CONTENTS

Nomenclature 11
Introduction 12
1. Literature Review 16
1.1. Linear Recurrence Sequences 19
1.2. Hankel Matrices and Their Ranks 21
1.3. Algebraic Decomposition of a Solution of a Discrete Map 21
1.4. The Role of *H*-rank in Nonlinear System Analysis 22
1.5. Short-term Series Forecasting 25
1.6. Basic Linear Algebra Subprograms and Linear Algebra PACKage 26
2. Computation of *H*-ranks and Their Patterns 30
2.1. Numerical Methods for Computing *H*-ranks and Their Analysis 30
2.1.1. The Algorithm for the Computation of the *H*-rank 30
2.1.2. Aspects of Floating Point Arithmetic for the Computation of *H*-ranks 31
2.1.3. Notes on Finding *H*-rank Using Floating Point Arithmetic 32
2.1.4. The Computation of Pseudoranks 35
2.2. Computational Reconstruction of the Patterns of *H*-ranks 36
2.2.1 Applications of *H*-ranks for the Circle Map 36
2.2.2. Selecting the Optimal Value of ε for Patterns of *H*-ranks 39
2.3. Conclusions 41
3. Manifolds of Convergence and Their Applicability for the Control of Nonlinear Systems 43
3.1. Stable Manifolds, Unstable Manifolds and Manifolds of Non-asymptotic Convergence 43
3.2. The Manifold of Non-asymptotic Convergence and the *H*-rank 44
3.3. The Quality of *H*-ranks Near the Manifolds of Convergence 47
3.4. Non-asymptotic Convergence and the Logistic Map 49
3.4.1. Classification of Manifolds for the Logistic Map 49
3.4.2. Non-asymptotic Convergence in the Logistic Map 50
3.5. Pseudo Manifolds in the Space of System Parameters 52
3.5.1. A pseudo-stable Structure in a Completely Invertible Bouncer System 52
3.5.2. Patterns of *H*-ranks for the Bouncer Model 56
3.6. Non-asymptotic Temporary Convergence 61
3.6.1. The Stable Manifold of the Bouncer Model 61
3.6.2. The Pseudo-stable Structure of the Bouncer Model 61
3.7. Controlling of Discrete Dynamical Systems 65
3.7.1. Temporary Stabilization of the Unstable Period-1 Attractor 65
3.7.2. The Sensitivity of the Temporary Stabilization Technique to External Noise 67
3.7.3. Controlling of Period-2 Unstable Orbits in a Bouncer System 69
3.7.4. Improvement of the Control Strategy by Utilizing the Gaussian Noise . 72
3.7.5. *H*-pseudoranks as a Tool for Controlling the Circle Map 72
3.8. Controlling of Continuous Dynamical Systems 75
3.8.1. Clocking Convergence to a Limit Cycle 75
3.8.2. Control of Transient Processes 79

3.9. Conclusions 81
4. *H*-ranks for Time Series Analysis 83
4.1. Onset of Chaos in the Dynamical System 83
4.1.1. Algebraic Decomposition of a Solution of a Discrete Map 83
4.1.2. Numerical Experiments with the Logistic Map 86
4.1.3. Numerical Experiments with Real-world Time Series 93
4.2. The Reconstruction of Skeleton Sequences Based on the *H*-rank 94
4.2.1. Weighted Moving Average and the Order of LRS 98
4.2.2. WMA and Real-world Time Series 100
4.2.3. Preprocessing 100
4.2.4. The Optimization Strategy 100
4.2.5. Computational Experiments 102
4.3. Time Series Forecasting Based on the Algebraic WMA 103
4.3.1. The Forecasting Algorithm 103
4.3.2. Computational Experiments 104
4.4. Applications of *H*-ranks in Real World Magnetometer Data 106
4.4.1. Magnetometer Data Formats of the Intensity of a Magnetic Field 106
4.4.2. Algebraic Reconstruction of the Magnetic Field Intensity Based on *H*-ranks 107
4.5. Conclusions 110
Final Conclusions 112
References 113
List of Scientific Publications on the Theme of the Dissertation 123

LIST OF FIGURES

Fig. 1. Numerical reconstruction of Arnold tongues for the circle map 17
Fig. 2. The bifurcation diagram of the mathematical pendulum 18
Fig. 3. The bifurcation diagram for the circle map at $K = \pi/2$ 37
Fig. 4. Pseudoranks of the circle map 37
Fig. 5. Maps of pseudoranks in the zoomed area of the widest Arnold tongue for various parameter values 38
Fig. 6. Maps of pseudoranks for a variety of parameter values ($0 \le \Omega \le 1, 0 \le K \le \pi$ and $\theta_0 = 0.5$) 39
Fig. 7. Maps of pseudoranks for a variety of initial conditions ($0 \le \Omega \le 0.4$, $0 \le \theta_0 \le 0.4$ and $K = \pi/2$) 40
Fig. 8. The relationship between the absolute root mean square difference E and the ε value at $m = 30$ 40
Fig. 9. The relationship between the absolute root mean square difference E and the ε value at $m = 30$ 41
Fig. 10. The construction of the manifold of non-asymptotic convergence to the stable period-1 regime 45
Fig. 11. The bifurcation diagram of the circle map is shown in part (a) at $\Omega = 0.15$. The manifold of non-asymptotic convergence to the period-1 regime is illustrated in part (b). The map of pseudoranks is shown in (c). All computations are performed at $\Omega = 0.15$ 46
Fig. 12. (a) The stable (solid line) and the unstable (dashed line) manifolds for the circle map at $K = \pi/2$. (b) The manifold of non-asymptotic convergence to the period-1 regime at $K = \pi/2$ 48
Fig. 13. The comparison of the manifold of non-asymptotic convergence (to the period-1 regime) to the plot of accuracy loss detection ($\varepsilon = 10^{-16}, K = \pi/2, k = n!/2$) 49
Fig. 14. Backward iterative steps for the Logistic map 50
Fig. 15. The manifold of the non-asymptotic convergence for the Logistic map 50
Fig. 16. Three different types of transient processes for the non-invertible Logistic map 51
Fig. 17. The eigenvalues of the Jacobian matrix for $\left(x^{(1)}, y^{(1)}\right)$ (part (a)) and $\left(x^{(2)}, y^{(2)}\right)$ (part (b)) 55
Fig. 18. The bifurcation diagram for the bouncer model; $\alpha = 0.1$ 56
Fig. 19. Patterns of *H*-ranks computed for the bouncing ball model at a variety of values of β 57
Fig. 20. Numerical reconstruction of the slope of separatrices $S(\beta)$ 58
Fig. 21. Patterns of *H*-ranks in a periodic sheared band computed at a variety of values of β. The parameter α is fixed at 0.1 59

Fig. 22. The evolution of the pattern of *H*-ranks for the continuous variation of β in horizontal (a) and vertical (b) sections of sheared bands of *H*-ranks; parameter α is fixed at 0.1 60
Fig. 23. The stable (a) and the unstable (b) manifolds of the bouncer model at $\alpha = 0.1$ and $\beta = 2.5$ 61
Fig. 24. The evolution of a transient process starting from the initial conditions coinciding with the center of the second upper tulip in the pattern of *H*-ranks..... 62
Fig. 25. Schematic diagram illustrating the skeleton-type structure of the pattern of *H*-ranks 63
Fig. 26. The control strategy illustrated at $\alpha = 0.1$ and $\beta = 2.5$ 66
Fig. 27. Control strategy illustration for the bouncer model 67
Fig. 28. The evolution of transient processes perturbed by the Gaussian noise at: $b = 0.0001$ (parts (a) and (b)); $b = 0.001$ (parts (c) and (d)); $b = 0.01$ (parts (e) and (f))..... 68
Fig. 29. Bifurcation diagrams of the bouncer system..... 69
Fig. 30. Patterns of *H*-ranks..... 69
Fig. 31. The control of the unstable period-2 orbit for the bouncer model 70
Fig. 32. The control of the unstable period-2 orbit..... 71
Fig. 33. The control strategy illustrated for the bouncer model 71
Fig. 34. Control of the unstable period-2 orbit for the bouncer model..... 72
Fig. 35. Pseudoranks of the circle map..... 73
Fig. 36. The adjusting of Ω^* 74
Fig. 37. The pattern of *H*-ranks for the system $\ddot{x} + b\dot{x} + \sin x = 2.048\cos(2t/3)$; $x(0) = 0$ is fixed for all initial conditions..... 76
Fig. 38. The pattern of *H*-ranks for system $\ddot{x} + b\dot{x} + \sin x = 2.048\cos(2t/3)$; $x(0) = 0$ is fixed for all the initial conditions..... 77
Fig. 39. The pattern of *H*-ranks for the system $\ddot{x} + b\dot{x} + \sin x = 2.048\cos(2t/3)$; $\dot{x}(0) = 0$ is fixed for all the initial conditions..... 78
Fig. 40. Asymptotic versus non-asymptotic convergence to the stable limit cycle in the stroboscopic representation of the transient data of the system $\ddot{x} + b\dot{x} + \sin x = 2.048\cos(2t/3)$ 78
Fig. 41. The pattern of *H*-ranks for the system $\ddot{x} + b\dot{x} + \sin x = 2.048\cos(2t/3)$ on the phase plane $x_0 - \dot{x}_0$ 79
Fig. 42. The control of the transient process based on a single external impulse 80
Fig. 43. Algebraic decomposition of transient processes of the Logistic map at $a = 3.59$ and $x_0 = 0.5$ at $\varepsilon = 10^{-10}$ (a, b); at $\varepsilon = 10^{-19}$ (c, d) and at $\varepsilon = 10^{-30}$ (e, f) 87
Fig. 44. The minimization of extrapolation errors for the Logistic map at $r = 3.59$ and $x_0 = 0.5$ 88
Fig. 45. Algebraic decomposition of transient processes of the Logistic map at $r = 3.55$ and $x_0 = 0.01$ (a, b); $x_0 = 0.25$ (c, d) and $x_0 = 0.5$ (e, f) 89

Fig. 46. Algebraic decomposition of iterated sequences produced by the Logistic map at $r = 3.55$ and $x_0 = 0.5$ as the 5 initial steps are omitted (a, b) and first 500 steps are omitted (c, d)..... 90
Fig. 47. The distribution of roots of the characteristic algebraic equation for the Logistic map in the range $0 < r < 3.6$ 90
Fig. 48. The variation of the rank of the algebraic representation of the solution of the Logistic map (a) and extrapolation errors (b) in the range $0 < r < 3.6$ 91
Fig. 49. The distribution of roots of the characteristic algebraic equation for the Logistic map in the range $3.3 < r < 3.6$ 92
Fig. 50. The variation of the rank of the algebraic representation of the solution of the Logistic map (a) and extrapolation errors (b) in the range $3.3 < r < 3.6$ 92
Fig. 51. Algebraic extrapolation of real-world time series: the normalized monthly mean temperatures in the southwestern mountain region over a time period starting in the year 1932 (a, b) and an excerpt from normalized daily net retail sales (c, d). 93
Fig. 52. The continuous convergence of ε-*H*-spectrum to the *H*-spectrum as $\varepsilon \to 0$ 97
Fig. 53. The geometrical shape of the target function N_ε in respect to weight coefficients w_1 and w_2 101
Fig. 54. A near optimal set of weight coefficients for the Gaussian noise; the width of the observation window is 10..... 102
Fig. 55. A near-optimal set of weight coefficients for the synthetic time series contaminated with noise; the width of the observation window is 10..... 103
Fig. 56. The schematic diagram of AWMA prediction..... 104
Fig. 57. The application of AWMA to *erppc* series at $L = 4$; $\varepsilon = 0.04$ 105
Fig. 58. A near-optimal set of weight coefficients for *erppc* at the first prediction step; $L = 4$ 105
Fig. 59. Software created for extracting the magnetic field data, calculating the spectrograms, the power of a signal and for filtering the signal of the magnetic field intensity 107
Fig. 60. Spectrograms for the time period of 1h on 21st of December 2014 107
Fig. 61. Variation of the magnetic field and its power (classical squared RMS approach) for the time period of 1h on the 21st of December 2014..... 108
Fig. 62. The title page of www.healthmath.lt..... 108
Fig. 63. The process of finding the optimal rank of the series representing the magnetic field intensity 109
Fig. 64. Algebraic extrapolation of the magnetic field intensity..... 110
Fig. 65. Algebraic extrapolation of the magnetic field intensity..... 110

LIST OF TABLES

Table 1. A number representation in double format 31
Table 2. Multiplication in floating point arithmetic..... 33
Table 3. Addition in floating point arithmetic 33
Table 4. Multiplication in floating point arithmetic..... 33
Table 5. Multiplication in floating point arithmetic..... 33
Table 6. Multiplication in floating point arithmetic..... 34
Table 7. Summary on the number of operations..... 34
Table 8. A comparisson of the speed of computation for patterns of *H*-ranks 38
Table 9. RMSE as a function of the observation window for MA prediction 105
Table 10. The data structure of magnetometer recordings..... 106

NOMENCLATURE

$\mathbb{C}$ – the set of complex numbers.

$d^{(m)}$ – determinant of Hankel matrix of order m.

$E(\varepsilon)$ – the absolute root mean square difference between two consecutive patterns of *H*-ranks.

ϕ – the argument of ρ.

$H^{(m)}$ – Hankel matrix of order m.

HrS – *H*-rank of sequence S.

$Hr(i,j)$ – digital image of the pattern of *H*-ranks.

$\binom{j}{k}$ – the number of different k-combination in a set of j elements.

ξ – a random value distributed by the Gaussian white noise.

LRS – linear recurrence sequence.

$\overline{m}$ – the upper limit for the *H*-rank (pseudorank) of the sequence.

MAPE – mean absolute percentage error.

$\mathbb{N}$ – the set of natural numbers.

N_{ε} – the number of SVD eigenvalues greater than ε.

$\mathbb{R}$ – athe set of real numbers.

RMSE – root mean square error.

ρ_k – the *H*-eigenvalues of the sequence.

$\mathbb{Q}$ – the set of irrational numbers.

$x_{n+1} = f(x_n)$ – a discrete nonlinear map.

WMA – weighted moving average.

$\mathbb{Z}$ – the set of integers.

INTRODUCTION

Relevance of the topic

Although nonlinear dynamical systems represent a classical research area, this field is being constantly developed. Almost every real world phenomenon is described as a nonlinear system. Hence the theory of nonlinear dynamical systems possesses a broad range of practical application. Engineering systems are becoming increasingly complex in nature. Thus the demand for control methods to obtain the desired system dynamics is highlighted. This also implies the rise of dynamical systems. Application of nonlinear dynamical systems has become interdisciplinary, and it spans research areas from physics to engineering, from economics to psychology and from medicine to biology.

Extensive academic interest has been recently dedicated to the satellite industry. Problems concerning Satellite formation flying (SFF) (i.e. when several satellites work together to save the cost of a single space mission) or Tethered Satellite System (special satellites for the exploration of space) are an increasingly common topic in the latest scientific papers. The dynamics of these systems is described as highly nonlinear and sensitive to the environment. The orbits of the satellites are modelled by limit cycles in nonlinear dynamics.

Complex systems described by large numbers of processes and highly nonlinear dynamics are often investigated in biology and medicine. Their examples include cancer progression, response to the treatment of a disease, molecular phenomena and hypoxia to name just a few. Some systems are intricately coupled and, evidently, are difficult to approach by restricting the research within only experimental methods. Nonlinear dynamical models and advanced computer simulations provide crucial insight into such systems and their dynamics.

Population dynamics, epidemic modeling or the study of disease spreading have always been in the center of attention. Nonlinear iterative maps, ordinary or partial differential equation models as well as difference equation models describe the evolution of real world systems. Corresponding modelling approaches are capable of providing applicable control or analytical strategies. The ultimate aim may be to conserve endangered species, to control the outbreak of a disease or to limit the consumption of natural resources. Without the analysis of nonlinear effects in dynamical systems it would hardly be possible to investigate the above mentioned problems.

Chaotic nonlinear systems were first considered by Henri Poincaré more than a century ago, and the famous term ‘butterfly effect’ was coined by Edward Lorenz in 1972. But the peak in the research of the dynamics of nonlinear systems occurred during the last decade of the 20th century. This resulted in extensive application of the *Chaos theory* in practice taking place. The improvement of key properties of computers has also made an important contribution towards the implementation of new methods of nonlinear dynamics in a wide variety of fields. For example, the performance of a modern computer enables to model the thermal denaturation of DNA molecules and to control biological neural networks. Combined with the

innovative methods of nonlinear dynamics, this may lead to advanced understanding of our nature.

New algorithms for the analysis of nonlinear systems and previously unknown properties are being created and discovered. What concerns matrices of special form (*Hankel* matrices in this case), their extensive recent applications in time series forecasting, system identification or algebraic analysis have yielded major benefits. The Hankel matrix preserves the algebraic structure of the sequence, which makes it possible to use this type of matrix for the development of special methods for nonlinear systems.

It must be emphasized that this work mostly focuses on the application and the use of *H*-ranks in the identification of the properties of nonlinear systems rather than on constructing new algorithms. In this respect, *H*-ranks act as a rich computational tool in nonlinear systems analysis. *H*-rank based algorithms enable researchers to reveal and solve a set of new system identification, forecasting and control problems. The development of the theory of *H*-ranks is the main value of this work.

The object of the research:

Patterns of *H*-ranks and their application for the identification, forecasting and control of nonlinear dynamical systems.

The aim of the research:

To use and develop *H*-rank based techniques for the analysis of nonlinear systems and real world time series.

The aim is achieved by solving the following problems:

1. To develop the strategy for constructing patterns of *H*-ranks for discrete and continuous nonlinear dynamical systems. To consider the quality of these patterns regarding numerical aspects of floating point arithmetic.
2. To employ patterns of *H*-ranks for the identification of manifolds of convergence in nonlinear systems.
3. To construct and implement the control algorithm based on the patterns of *H*-ranks for discrete and continuous nonlinear dynamical systems.
4. To propose an algebraic approach based on the rank of the sequence for the analysis of the onset of chaos in discrete nonlinear dynamical systems.
5. To construct and implement a short-term time series forecasting technique based on the properties of skeleton sequence of a time series.
6. To perform algebraic analysis of the data from the real world magnetometer representing the intensity of the local magnetic field.

The methods and software for the research:

1. Techniques of mathematical and statistical analysis were used for the research. Algebraic analysis took an important role in this work in developing the theory of *H*-ranks. Practical application tools were developed. Methods originating from the dynamical systems theory were employed for nonlinear models used in the research.
2. Throughout the entire thesis, principles of digital image processing were applied. Some aspects of floating point arithmetic were considered.
3. Matlab and its standard toolboxes (Image processing toolbox, Parallel Computing Toolbox, Statistics Toolbox, Signal Processing Toolbox,

Symbolic Math Toolbox), C++ programming language and LAPACK libraries (mainly on Linux platform for better performance) served as the programming tools used for the research.

4. A set of programming tools and applications was also created by the author of the thesis.

Scientific novelty and practical significance of the research:

Manifolds of convergence cannot be found directly for nonlinear maps. Previously existing computational tools (e.g. *Dynamics* or *XPP* software) comprising numerical algorithms largely differ in application areas and/or performance. Identification methodology of manifolds of convergence by using *H*-rank based techniques for both discrete and continuous dynamical systems is developed in this work. Considerations of using *LAPACK* package (which is a standard for high performance computations) enabled to implement the algorithms presented in this work efficiently in comparison with the Matlab package.

Development of novel control techniques based on *H*-ranks is presented in this work. Patterns of *H*-ranks were used for this purpose. Examples with two discrete nonlinear systems and one continuous nonlinear system are considered.

New forecasting techniques for short time series are proposed and applied to real world time series.

Practical significance of the research was accomplished by applying the algebraic analysis discussed in this work to the real world magnetometer data.

Information provided for the defense:

1. Computation strategy for the construction of patterns of *H*-ranks.
2. Computation strategy for the identification of manifolds of non-asymptotic convergence.
3. Computation strategy for the control of unstable orbits in discrete and continuous dynamical systems.
4. Novel methodology for time series forecasting based on the algebraic properties of the *H*-rank.

Approval of the results:

The results of the dissertation were presented in 7 publications including 3 papers in international journals indexed in the Institute for Scientific information (ISI) as the main list of publications with citing indexes and 2 papers in ISI indexed American Institute of Physics (AIP) proceedings. The topics covered in the dissertation were presented in 4 international and 2 national conferences including "International Conference on Numerical Analysis and Applied Mathematics 2012 (ICNAAM 2012)", "International Conference on Numerical Analysis and Applied Mathematics 2013 (ICNAAM 2013)", "International Conference on Recent Advances in Pure and Applied Mathematics (ICRAPAM 2014)" and "8th Chaotic Modeling and Simulation International Conference (CHAOS 2015)".

The experiments presented in the final chapter were performed by using the data of a real world magnetometer which is the only one of the kind in Europe; it is located in central Lithuania. The results were also used while carrying out the project "Research on the relations between Earth's magnetic field, human's and animal's cardiovascular systems (GEOMAG)" funded by R&D and Innovation Fund

of Kaunas University of Technology. The time period of the project spanned from March 2014 to December 2014.

The structure and length of the dissertation:

This doctoral dissertation consists of an introduction, 4 major sections, conclusions, a list of references and a list of the author's publications. The total length of the dissertation is 124 pages. The thesis features 65 figures, 10 tables and a list of 162 cited sources.

1. LITERATURE REVIEW

Control of Nonlinear systems

Depending on the problem to be solved, it is important to measure the amount of uncertainty in a system in order to predict or to control it. The classical approach to controlling chaos is to reduce the amount of uncertainty in dynamical systems. An efficient method of chaos elimination as the control method for a system (*OGY* method) was suggested by Ott, Grebogi and Yorke in (Ott, Grebogi and Yorke, 1990). One of the parameters of a system is the state of being perturbed in the form of feedback. The perturbation here is time-dependent. Another approach towards chaos control called *Pyragas* method was suggested 2 years later in (Pyragas, 1992). *OGY* method and its variations have been broadly applied for the solution of scientific (Akhmet and Fen, 2012) and engineering problems (Ferreira, Savi and de Paula, 2014; Gritli, Belghith and Khraief, 2014). Stabilization of unstable periodic orbits has also been employed as in OGY scheme. The difference of the methods stems from *Pyragas* method using time continuous perturbation with the help of an external oscillator or delayed self-controlling feedback. Delayed feedback control also appears in various practical applications such as the stabilization of traffic flow (Jin and Hu, 2013) or the elimination of contact loss in the clearance joint (Olyaei and Ghazavi, 2012) to name a few.

The application of both methods mentioned above does not require *a priori* information about the analytics of the system's dynamics. *H*-rank based techniques are rather different because they are non-feedback control methods and require the system's dynamics or its realization in time to be known *a priori*. Thus feedback control methods are primarily used in experimental problems whereas *H*-rank possesses a stronger potential in analytical applications.

A chaotic system can be controlled by synchronizing it with a system of harmonic oscillators. This idea was proposed by (Olyaei and Wu, 2015). The uniqueness of the method is the fact that it does not change the solution of the system. It stabilizes the periodic behavior of solutions by applying small perturbations. Examples under consideration include the well-known Duffing oscillator which is a real word physical system. The scheme can be implemented experimentally even if the analytical expression of the dynamical system is not known. The application of the technique requires the knowledge of the fundamental frequency of the desired motion. If the quantity is not known, it still can be approximated by using, for example, the phase space reconstruction.

Nonlinear models and chaos analysis

The circle map is used to model cardiac arrhythmias and the so-called pacemaker of the human heart (Glass and Shrier, 2014). The circle map is represented by the one-dimensional iterative map:

$$\theta_{n+1} = f\left(\theta_n\right) = \theta_n + \Omega - \frac{K}{2\pi} \cdot sin\left(2\pi\theta_n\right); \tag{1}$$

where θ is a polar angle ($\theta \in [0;1)$); K is the coupling strength; Ω is the driving phase and $n = 0,1,\ldots$. For small to intermediate values of K ($0 < K < 1$), and for certain values of Ω, the circle map exhibits a phenomenon called phase locking (also known as entrainment). In the phase-locked region, values θ_n advance essentially as a rational multiple of n.

The phase-locked regions in $\Omega - K$ parameter plane are called Arnold tongues (Boyland, 1986). Fig. 1 shows the numerical reconstruction of these phase-locked regions. Arnold tongues are observed in a variety of nonlinear physical models whenever the effect of phase locking occurs in those systems (Boyland, 1986; Escalona, José and Tiesinga, 2002; McGuinness, Hong, Galletly and Larsen, 2004; Rosa, Correia and Rech, 2009; Schilder and Peckham, 2007).

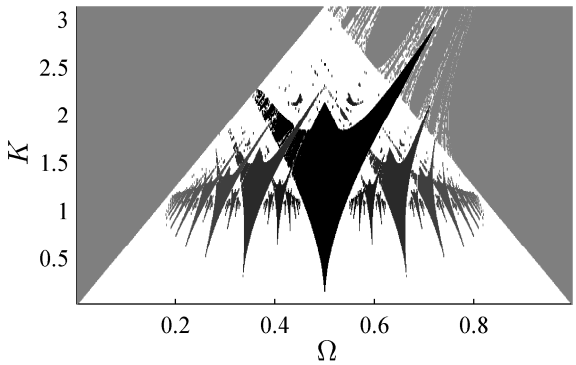

Fig. 1. Numerical reconstruction of Arnold tongues for the circle map. For K values greater than 1, the regions start to overlap each other

The circle map is exploited in numerous models of nonlinear dynamical systems whenever the effects of quasiperiodicity are encountered (Boyland, 1986; Escalona et al., 2002; Rosa et al., 2009; Schilder and Peckham, 2007).

The existence of Arnold tongues in the circle map has already been known for more than five decades (Arnold, 1961). There exist a number of computational techniques for the visualization of Arnold tongues. The universal algorithm for the identification of Arnold tongues is based on two simple steps. At first, the system must be iterated far away from initial conditions until all transient processes cease down. Secondly, one must identify the effect of the phase locking in the discrete stationary attractor. Different modes of the phase locking are then visualized by different colors.

Limit cycles and natural phenomena

A wide range of oscillators in biological systems experience limit cycle behavior. A network of driven coupled oscillators (e.g. neurons) could be regarded as a simple circadian system. Analysis and simulation of a circadian clock is presented in (Bordyugov, Granada and Herzel, 2011). Exploiting limit cycles of nonlinear dynamical systems allowed us to describe the events of the cell cycle and to understand why these events occur (Ferrell, Tsai and Yang, 2011; Gérard and

Goldbeter, 2012). There are more applications involving, e.g. pacemaker cells (González-Miranda, 2012) or calcium oscillations (Ji and Lu, 2013).

One of the most practically important problems related to limit cycles is the presence of noise in the system. It is a classical topic in circuit analysis. The nonlinear analysis of noise in free running oscillators affected by white Gaussian noise sources was performed by (Traversa and Bonani, 2011). Adding the noise blurs the phase-lock behavior of the system. In the case of the limit cycle oscillator, the noise makes its orbit irregular. This may also shift the phase. Academic researches showed that phase-locking to the every possible rational ratio is observed only in the limit cycle oscillator (Mitarai, Alon and Jensen, 2013).

A periodically driven pendulum

A periodically driven pendulum is a paradigmatic model in the study of oscillations and other phenomena in physics and nonlinear dynamics (Bhattacharjee and Kumar, 2014; Sakthivel and Rajasekar, 2012). It has deserved much attention, from many viewpoints, including different model complexity, forcing and damping aspects. It is also one of the simplest physical systems whose dynamical description can be reduced to a circle map (Jensen, Bak and Bohr, 1983; Jensen, Bak and Bohr, 1984; Ostlund, Rand, Sethna and Siggia, 1983). In turn, the circle map is used in numerous models of nonlinear dynamical systems whenever the effects of quasiperiodicity are encountered (Boyland, 1986; Escalona et al., 2002; McGuinness et al., 2004; Schilder and Peckham, 2007).

The model reads:

$$\frac{d^2x}{dt^2} + b\frac{dx}{dt} + \sin x = f\cos(\omega t). \tag{2}$$

where t is time; x is the angular coordinate; b is the linear damping coefficient ($b > 0$); f and ω is the amplitude and the angular frequency of the harmonic forcing. Eq. (2) exhibits rich chaotic behavior at $b = 1$; $f = 2.048$ and $\omega = \frac{2}{3}$ (Hilborn, 2000): strobing at the drive frequency produces a cascade of period doubling bifurcations at $1 \le b \le 1.05$ (Fig. 2).

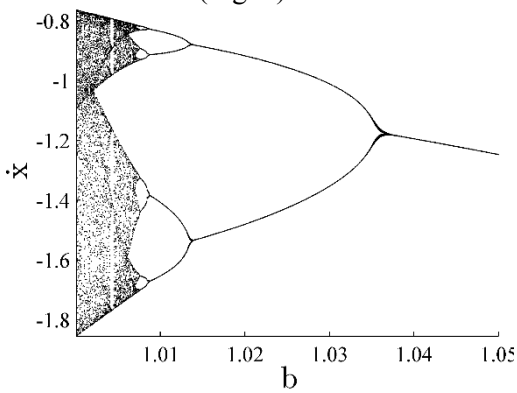

Fig. 2. The bifurcation diagram of the mathematical pendulum

The bouncing ball problem

A particle falling down in a constant gravitational field on a moving platform is called a bouncing ball problem, or a bouncer. This model was suggested more than thirty years ago (Pustilnikov, 1983; Zaslavsky, 1978) as an alternative simplification to the Fermi–Ulam model (Lieberman and Lichtenberg, 1972) of cosmic ray acceleration (Fermi, 1949). Many different approaches to the bouncer model have been studied theoretically and experimentally (Chirikov, 1979; Everson, 1986; Lichtenberg, Lieberman and Cohen, 1980; Pierański and Malecki, 1986). It has been proven to be a useful model for experimental exploration of several new nonlinear effects (Guo and Luo, 2011; Kowalik, Franaszek and Pieranski, 1988; Luo and Guo, 2013; Wiesenfeld and Tufillaro, 1987). Moreover, it has been implemented in a number of engineering applications (Hongler, Cartier and Flury, 1989; Hongler and Figour, 1989; Luo and Han, 1996).

The bouncer model can be briefly characterized by the following basic statements:

(i) Maps derived for the bouncer model can be exactly iterated for any number of iterations into the future (Pierański and Malecki, 1986; Wiesenfeld and Tufillaro, 1987).

(ii) The ball-platform collisions can be characterized by a coefficient of restitution α changing from $\alpha = 1$ for a perfectly elastic case to $\alpha = 0$ for a completely inelastic situation.

(iii) The chaotic bouncer can be easily used to relate theoretical predictions to experimental results, (Kowalik et al., 1988; Wiesenfeld and Tufillaro, 1987) which renders it into a paradigmatic model in nonlinear dynamics.

The bouncer model is a discrete dynamical system as the time evolution of the dynamics of the system is discontinuous at collisions. If the impact between the table and the ball is inelastic, the velocity of the ball just after the impact can be represented with the help of a discrete map which is called the bouncer system (Guckenheimer and Holmes, 1983; Holmes, 1982; Joseph, Ines and Sanjuan, 2012)

$$\begin{cases} x_{n+1} = F_B\left(x_n, y_n\right) = x_n + y_n; \\ y_{n+1} = G_B\left(x_n, y_n\right) = \alpha y_n + \beta cos\left(x_n + y_n\right); \end{cases} \tag{3}$$

where the variable x_n is the time interval between the ($n-1$)-th and the n -th collisions of the ball while y_n is the velocity of the ball immediately after the n -th impact. The parameter $\alpha \in \left(0,1\right]$ is the coefficient of restitution and the parameter β is associated with the table frequency. If the coefficient of restitution is $\alpha = 1$ then Eq. (3) is reduced to the standard map. We should note that the bouncer system described as Eq. (3) is a good approximation of the bouncing ball (Guo and Luo, 2011).

1.1. Linear Recurrence Sequences

An order n linear homogeneous recurrence relation with constant coefficients is an equation of the following form:

$$x_j = \alpha_{n-1}x_{j-1} + \alpha_{n-2}x_{j-2} + \ldots + \alpha_0 x_{j-n}\,, \tag{4}$$

where coefficients α_k, $k = 0,1,\ldots,n-1$ are constants. A sequence which satisfies a relation of this form is a linear recurrence sequence (LRS). The initial values x_k, $k = 0,1,\ldots,n-1$ uniquely determine the evolution of this LRS (Kurakin, 2001; Park and Elden, 2003; V. L. Kurakin and Nechavev, 1995). The auxiliary polynomial to Eq. (4) reads:

$$P(\rho) = \rho^n - \alpha_{n-1}\rho^{n-1} - \alpha_{n-2}\rho^{n-2} - \cdots - \alpha_0 \tag{5}$$

whose n roots describe the sequence satisfying the recurrence. If roots $\rho_1, \rho_2, \ldots, \rho_n$ are all distinct, then the recurrence takes the form:

$$x_j = \mu_1\rho_1^j + \mu_2\rho_2^j + \ldots + \mu_n\rho_n^j, \tag{6}$$

where the coefficients $\mu_1, \mu_2, \ldots, \mu_n$ are determined in order to fit the initial conditions of the recurrence. We should note that all the roots are real or complex conjugate only if LRS is real. If – though – some roots coincide then the recurrence reads as:

$$x_j = \sum_{k=1}^{r}\sum_{l=0}^{n_k-1}\mu_{kl}\binom{j}{l}\rho_k^{j-l}, \tag{7}$$

where r is the number of distinct roots and n_k is the multiplicity index of the k-th root; $n_1 + n_2 + \cdots + n_r = n$.

An interesting property of LRS has been recently discovered. It was shown that there exists a prime number p together with the set of integers $x_1, \ldots, x_d$ such that no element of the linear recurrence sequence $X = \{x_n\}_{n=1}^{\infty}$ is divisible by p (Dubickas and Novikas, 2014). In other words, it is possible to construct a LRS not containing zeros. Also, for any non-negative integer s there is a prime number $p > 3$ and the set of integers $x_1, \ldots, x_d$ so that every element of the sequence $X = \{x_n\}_{n=1}^{\infty}$ modulo p belongs to the set $\{s+n\}_{n=1}^{p-2s-1}$ (Dubickas and Novikas, 2014).

LRS applications in pseudorandom number generators

The underlying algebraic structure of a linear recurrence sequence has been known for its successful application in cryptography. Fibonacci numbers were employed in the ciphering algorithm in (Gandhi, Sekhar and Srilakshmi, 2011) as the coefficients of LRS or order 2. Secrecy is ensured by the key, and the key matrix is obtained by using LRS.

A minimal polynomial of the sequence is its characteristic polynomial of the least degree. Minimal polynomials are used in solving cryptography problems related to the encryption key security. As an auxiliary result of the so called Berlekamp–Massey algorithm, a minimal polynomial of a linear recurrent sequence

in a field is produced (Shih et al., 2013). The minimal polynomial of a sequence then comes from the Wiedemann's algorithm applied to assess the immunity to algebraic attacks.

The problem of image encryption and decryption with the objective to protect the images from unauthorized viewing is treated in (Aissa, Nadir and Ammar, 2014). The encryption scheme is constructed by using the stream cipher system based on the nonlinear combination generator. The authors proposed a pseudorandom number generator whose results are combined with the data of a secret image during the process of encryption. The pseudorandom number sequence from the proposed generator is a linear recurrence sequence. Extensive research proved the scheme to be simple and highly efficient.

1.2. Hankel Matrices and Their Ranks

A Hankel matrix is a matrix in which element a_{ij} depends only on the sum of $i+j$. In other words, it is a square matrix with constant skew diagonals. Such matrices are also called persymmetric matrices (Muir, 2003).

Older literature refers to the determinants of Hankel matrices as orthosymmetric determinants (Aitken and Aitken, 1956).

The definition of the Hankel rank was coined in 2007. It describes the algebraic relations among the elements of a sequence.

Let S be a sequence of real numbers:

$$S := \left(x_0, x_1, x_2, \ldots\right) \tag{8}$$

The Hankel transform of S yields a sequence of determinants of Hankel catalectican matrices:

$$d_n := \det\left(x_{i+j-2}\right)_{1\le i,j\le n+1}; n = 0,1,2,\ldots \tag{9}$$

The *H*-rank of the sequence S is equal to *m*; $m \in \mathbb{N}$ if:

$$d_{m+k-1} = 0 \tag{10}$$

for all $k \in \mathbb{N}$, but $d_{m-1} \neq 0$ (Ragulskis and Navickas, 2011). The existence of the *H*-rank is denoted by $HrS = m$.

1.3. Algebraic Decomposition of a Solution of a Discrete Map

Let us assume that the rank of the sequence *S* exists: $HrS = m$; $m < +\infty$. Then S is a deterministic algebraic sequence and its elements are expressed in the following form (Navickas and Bikulčienė, 2006):

$$x_n = \sum_{k=1}^{r}\sum_{l=0}^{n_k-1}\mu_{kl}\binom{n}{l}\rho_k^{n-l}; n = 0,1,2,\ldots \tag{11}$$

where the *H*-eigenvalues of the sequence $\rho_k \in \mathbb{C}$; $k = 1,2,\ldots,r$ can be determined from the Hankel characteristic equation

$$\begin{vmatrix} x_0 & x_1 & \cdots & x_m \\ x_1 & x_2 & \cdots & x_{m+1} \\ & & \cdots & \\ x_{m-1} & x_m & \cdots & x_{2m-1} \\ 1 & \rho & \cdots & \rho^m \end{vmatrix} = 0; \tag{12}$$

where the recurrence indexes of these roots n_k ($n_k \in \mathbb{N}$) satisfy the equality $n_1 + n_2 + \cdots + n_r = m$. It is clear that $\sum_{k=1}^{r} n_k = m$. Coefficients $\mu_{kl} \in \mathbb{C}$; $k = 1,2,\ldots,r$; $l = 0,1,\ldots,n_k - 1$ can be determined from a system of linear algebraic equations which can be formed from equalities Eq. (11) assuming the expressions of elements $x_{n_1}, x_{n_2}, \ldots, x_{n_m}$ of the sequence S where indexes of these elements satisfy inequalities $0 \le n_1 < n_2 < \cdots < n_m < +\infty$. Moreover, such a system of linear algebraic equations has one and only one solution. The subsequence $\left(x_0, x_1, x_2, \ldots, x_{2k-3}, x_{2k-2}\right)$ is then called the base fragment of sequence *S*.

If all the roots are different, Eq. (11) reduces to:

$$x_n = \sum_{k=1}^{m} \mu_{k0} \rho_k^n \,;\; n = 0,1,2,\ldots. \tag{13}$$

Algebraic progressions generalize arithmetic as well as geometric progressions and provide an insight into the dynamical process governing the evolution of the discrete sequence.

It can be noted that a chaotic sequence does not have a rank. Otherwise it would be an algebraic progression, and it could be decomposed into an algebraic form comprising roots and coefficients according to Eq. (11). The dynamics of the sequence would be deterministic, yet this contradicts the definition of a chaotic sequence.

1.4. The Role of *H*-rank in Nonlinear System Analysis

Clocking convergence

Clocking convergence is an important tool for investigating various aspects of nonlinear systems, especially chaotic maps. The rate of convergence to the critical attractor when an ensemble of initial conditions is uniformly spread over the entire phase space may provide some insight into the fractal nature and the scale invariance of the dynamical attractor (De Moura, Tirnakli and Lyra, 2000; Tonelli and Coraddu, 2006). Numerical convergence of the discrete Logistic map gauged with a finite computational accuracy is investigated in (Ragulskis and Navickas, 2011) where forward iterations are used to identify self-similar patterns in the region before the onset of chaos.

A computational technique based on the concept of the *H*-rank is proposed in (Ragulskis and Navickas, 2011) for measuring the convergence of iterative chaotic

maps. Computation and visualization of *H*-ranks in the space of a system's parameters and initial conditions provides some insight into the embedded algebraic complexity of the nonlinear system and reveals three overlapping manifolds of discrete iterative maps: the stable manifold, the unstable manifold and the manifold of the non-asymptotic convergence. It is shown in (Ragulskis and Navickas, 2011) that the computation of *H*-ranks can be effectively used to identify and assess the sensitivity of nonlinear systems to initial conditions and can be used as a simple and effective numerical tool for qualitative investigation of the onset of chaos for discrete nonlinear iterative maps. One of the aims of this work is to show the use of *H*-rank as a control tool for a discrete dynamical system.

The convergence to Arnold tongues is studied by using computational techniques based on ranks of Hankel matrices (*H*-ranks). The ranks of Hankel matrices carry important physical information about transient processes taking place in discrete nonlinear iterative maps. In this work it will be shown that the measurements of the convergence rate to Arnold tongues can reveal important physical information on the properties of the iterative system. Moreover, such enriched representation of Arnold tongues produces aesthetically beautiful pictures.

Numerical convergence of the discrete Logistic map gauged with a finite computational accuracy is investigated in (Ragulskis and Navickas, 2011) where forward iterations are used to identify self-similar patterns in the region before the onset to chaos. An alternative technique based on the concept of the *H*-rank is proposed in (Ragulskis and Navickas, 2011) for clocking the convergence of iterative chaotic maps. The *H*-rank also reveals three manifolds of the discrete iterative map: the stable manifold, the unstable manifold and the manifold of the non-asymptotic convergence.

Limit cycles in nonlinear systems

One of the main objectives of this work is to investigate the applicability of the concept of *H*-ranks for the assessment of the convergence processes to stable limit cycles. There exists a broad range of analytical and numerical techniques for the analysis of the stability of limit cycles. The techniques include the spectrum of Lyapunov exponents (Christiansen and Rugh, 1997; Habib and Ryne, 1995), averaging methods (Sanders, Verhulst and Murdock, 2007).

Floquet exponents (Chicone, 1999; Giesl, 2004; Traversa and Bonani, 2012) are successfully used for studying various properties of limit cycles. There are a range of scientific and engineering applications such as: the investigation of the dynamic characteristics of a rolling element bearing independence from the rotor system (Srinath, Sarkar and Sekhar, 2014); a numerical method intended to compute fundamental matrix solutions of non-autonomous linear differential equations with periodic coefficients is introduced in (Castelli and Lessard, 2013). Some problems in physics include (Krents, Anchikov, Molevich and Pahomov, 2014; Li, Chong, Yang, Kevrekidis and Daraio, 2014).

Floquet analysis was also used in assessing the reliability of crystal oscillators. Reference timing signals in electronic systems often use crystal oscillators. Crystal oscillators are sensitive to such deterministic interferences as electromagnetic interferences or power supply line fluctuations. As a result, predicting the

deterioration of the oscillator response due to deterministic signals has become a major concern (Maffezzoni, Zhang and Daniel, 2014). It is also known that high quality crystal oscillators exhibit very long transient responses before reaching the steady states. Thus simulating such a system may be an extremely time consuming process without applying such special techniques as Floquet analysis.

The knowledge of the stable and unstable manifolds of hyperbolic equilibria plays a central role in the understanding of many global, dynamical issues for autonomous maps. For a given nonlinear dynamical system, the only general way of studying such stable and unstable manifolds is by computing them numerically. Consequently, a number of different algorithms have been developed for computing the stable and unstable manifolds for autonomous maps (Broer, Osinga and Vegter, 1997; Dellnitz and Hohmann, 1997; Goodman and Wróbel, 2011; Hobson, 1993; Kostelich, Yorke and Zhiping, 1996; Krauskopf and Osinga, 1998; Moore and Hubert, 1999; Nusse and Yorke, 1998).

The onset of chaos

The onset of chaos is a classical research area exploring different physical, mathematical and engineering aspects of nonlinear dynamical systems. The period-doubling onset of chaos is described by using formal techniques in (Feigenbaum, 1982). The multifractal scaling structure at the onset of chaos is explored in (Jensen, 1987). The onset of chaos is explored in various nonlinear systems – in differential delay equations (Hale and Sternberg, 1988), in nuclear states of molecules (Tennyson and Farantos, 1985; Von Brentano and Zamfir, 1992) or in the Logistic map driven by colored noise (Choi and Lee, 1995). A variety of period-doubling universality classes in multi-parameter analysis of transition to chaos is explored in (Kuznetsov, Kuznetsov and Sataev, 1997). Chaotic attractors generated by iterated function systems and the emergence of chaotic behavior is studied in (Bahar, 1997); the cobweb model is used to illustrate the instability and the onset of chaos in (Chiarella, 1988). A route to ergodicity breakdown and statistical descriptions of nonlinear systems at the onset of chaos are investigated in (Coraddu, Lissia and Tonelli, 2006; Robledo, 2004). Fibonacci order in the period-doubling cascade to chaos and the comparison of recurrence quantification methods for the analysis of temporal and spatial chaos is discussed in (Linage, Montoya, Sarmiento, Showalter and Parmananda, 2006; Mocenni, Facchini and Vicino, 2011); the transition from maps to turbulence is discussed in (Lan, 2010). The applicability of Hamiltonian geometrical criterion for the exploration of chaos determined by the dynamical curvature of a conformal metric for a nonlinear Hamiltonian system is discussed in (Wu, 2009). A computer-algebraic criterion based on the autocorrelation function and Laplace-Borel transformation for the onset of chaos in nonlinear dynamical systems is proposed in (Ünal, 1989).

The system identification problem

Hankel matrices and the system identification problem are closely related. In the system identification theory, Hankel matrices are often constructed before the implementation of the model itself. One can form a Hankel matrix directly from the input-output data. The indirect approach is also possible by, for example, evaluating Markov parameters in the first place (Ma, Ahuja and Rowley, 2011). Usually the

aim is to construct the model of the lowest dimensionality possible. Here the Hankel matrix plays an important role because a state-space model can be obtained from its factorization. This can also be done by singular value decomposition (SVD).

Singular value decomposition of a real matrix H results in the product $H = USV^T$, where U is comprised of ortonormal eigenvectors of HH^T ; V consists of ortonormal eigenvectors of $H^T H$ and S is a diagonal matrix whose elements are sorted square roots of eigenvalues of $H^T H$ (singular values of H).

The first so-called state space realization algorithm was proposed in 1965 (Ho and Kálmán, 1966). It was an entirely revolutionary method at the time, and it incorporated the factorization of a Hankel matrix into two other matrices. It is not necessary to fix the dimension of a system before applying the method. The only requirement is set that it must be finite.

As Ho and Kálmán predicted, their method evolved into a number of applications in science and engineering (de Jong, 1978; Jafarzadeh, Lascu and Fadali, 2012; Lee and Yeom, 2012).

Minimizing the rank of a matrix

The matrix rank minimization problem arises whenever the complexity of a model is related to the rank of an appropriate matrix. Thus reducing the rank of such a matrix is equivalent to the reduction of the relative complexity of the model. The rank of a matrix can be minimized by minimizing the norm of that matrix. Application of this strategy to the Hankel matrix is proposed in (Fazel, Pong, Sun and Tseng, 2013). The methodology is applicable to (but not limited to) matrices with a linear structure including Hankel and Toeplitz matrices. The minimization of a norm is achieved by employing several first-order methods: alternating direction methods of multipliers, proximal point algorithms and gradient projection methods.

Minimization of the rank of a Hankel matrix can also be widely applied in the linear time-invariant (LTI) system theory. This theory originated from applied mathematics and features applications in many fields ranging from engineering to finance. For example, it has direct applications in such technical areas as NMR spectroscopy (Glass and Shrier, 2014), circuits (Baylis and Marks, 2012), signal processing (Monti, Meyer, Tschudin and Luise, 2012), etc. An LTI model can be fitted to the observed data and produce various optimization problems including minimization of the Hankel matrix rank.

1.5. Short-term Series Forecasting

MA techniques are widely used in signal smoothing (Manikandan and Soman, 2012) and time series forecasting applications (Holt, 2004). It is well known that MA(1) (MA at $L = 1$, or naïve prediction techniques) are one of the best predictors for highly random and complex time series (Sauer, Yorke and Casdagli, 1991).

Predicting short-time series is quite a challenging task as every proposed technique appears to be superior in some respect. It is admitted that a forecasting model is worth applying if it is better than the persistence model also known as the naïve prediction. In fact, the naïve prediction is an analogue to the moving average of the averaging window length equal to 1. The model draws a prediction being equal to the present value. For example, the ANN model for predicting the wind

speed proposed in (Ma, Hu and Xu, 2013) is less than 10.77% in terms of root mean square error compared with the persistence model. Short-term wind speed prediction has attracted lots of attention thus recently creating a separate niche for short-time series predictions in sustainable engineering (Nan, Li, Qiu, Zhao and Guo, 2013). Applications as the hourly scheduling of the generators is important in balancing the power production and demand (Dong-xiao, Hui-feng and Desheng, 2012). Apart from applications in engineering, scientific research on techniques for short-time series forecasting include (Ragulskis, Lukoseviciute, Navickas and Palivonaite, 2011), (Palivonaite and Ragulskis, 2014) or (Easton, Stephens and Angelova, 2014) to mention just a few. An interesting conclusion was drawn in (Chen, 2011) about naïve predictions and various combination models in forecasting the tourism demand. The naïve method might be the optimal method depending on the type of the error estimator considered even despite the fact that the overall performance of the naïve method is lower if compared to that of the combination models.

A time series forecast can also be achieved by reconstructing the underlying skeleton sequence. In this work, the *H*-rank based strategy is employed for the reconstruction of the skeleton sequence. Only one value is predicted forward; this makes it a short-time forecasting model. Previous findings showed that algebraic models could be successfully applied in forecasting (Ragulskis et al., 2011). The demand for improved or specialized techniques in the field of time series forecasting led to various other approaches such as the use of Hybrid Monte Carlo algorithm (Dong-xiao et al., 2012), decomposing time series using wavelets (Jia, Wei, Wang and Yang, 2014) or using a linear combination of forecasters (Firmino, de Mattos Neto and Ferreira, 2014).

Data often needs to be preprocessed in order for some forecasting method to be efficiently applied. The overview of preprocessing importance for the data of track irregularity could be found in (Jia et al., 2014). The time series could also be decomposed into a finite number of separate primitives, then each primitive could be predicted separately. Such preprocessing might improve the results as in (Wang, Hu, Ge, Ren and Zhao, 2014). In this work, the weighted moving average is found in the preprocessing stage. The goal is to find weight coefficients leading to the decomposition of the series to the skeleton sequence being the lowest order linear recurrence sequence. While the skeleton sequence is used for the search of the optimal algebraic decomposition, the actual predicted value comes from the application of the weighted moving average. The proposed algorithm is compared to standard time series models in terms of MAPE.

1.6. Basic Linear Algebra Subprograms and Linear Algebra PACKage

It is essential to make the optimal use of computer resources while performing a huge amount of computations.

Basic Linear Algebra Subprograms (BLAS) and Linear Algebra PACKage (LAPACK) are a set of tools for vector and matrix operations considered as industry standard. Initially implemented in Fortran, BLAS and LAPACK routines have also been used in Matlab (Skalicky, Lopez, Lukowiak, Letendre and Gasser, 2013). The operations are categorized into three main groups: scalar, vector and vector-vector

operations are called Level-1 BLAS routines; Matrix-vector and matrix-matrix operations are called Level-2 and Level-3 BLAS operations respectively. For more efficient computations, higher level routines are preferred (Gustavson, Waśniewski, Dongarra, Herrero and Langou, 2013). LAPACK uses Level 3 BLAS operations in order to benefit from the capabilities of modern computers. Some of the most important linear algebra algorithms in the scientific and numerical fields implemented in LAPACK are: matrix factorizations such as LU (PLU), QR or SVD; least-squares solutions of linear systems of equations and eigenvalue problems. The algorithms are implemented as block algorithms. Block algorithms are comprised of two successive phases: forming of sequence of Gaussian elimination-like operations (being very rich in Level 2 BLAS operations) and update of the trailing submatrix (leading to Level 3 BLAS operations) (Ltaief, Luszczek and Dongarra, 2012). Discussion of block algorithms is available at (Gustavson, Herrero and Morancho, 2014).

LAPACK functions have prefixes S, D, C, or Z depending on the selected type of arithmetic to be used. The prefixes correspondingly represent single real, double real, single complex, or double complex floating point arithmetic.

Solving linear algebra problems with LAPACK is extremely time efficient (Gray, Stewart and Tenesa, 2012; Lin, Gao, Sun, Cheng and Sorensen, 2012; Ordonez, Mohanam, Garcia-Alvarado, Tosic and Martinez, 2012; Peña, Núñez and Medina, 2014). Some improvements and alternatives to the standard LAPACK routines include (Aurentz, Vandebril and Watkins, 2013; Castaldo, Whaley and Samuel, 2013; Deadman, Higham and Ralha, 2013). Other discussions on the efficiency of the implemented standard functions include (Frison and Jorgensen, 2013; Gustavson, Waśniewski and Herrero, 2012).

A large amount of computations forms the need for building more processing time-efficient applications. GPU- (Graphics processing unit) based applications have been recently attracting lots of attention. One of the most difficult linear algebra algorithms to parallelize is the LU factorization. The current standard for an LU factorization is the one implemented in LAPACK (Donfack, Tomov and Dongarra, 2014). It is the function GETRF. A hybrid CPU/GPU computing approach to LU factorization efficiently balancing the workload between the CPUs and the GPUs was proposed in (Donfack et al., 2014) while another approach is presented in (Horton, Tomov and Dongarra, 2011). The algorithm was compared with such state-of-the-art libraries as MKL (Math Kernel Library for multicore) and MAGMA (Matrix Algebra on GPU and Multicore Architectures), and significant performance improvements were noted. The approach is also applicable to other linear algebra algorithms.

LAPACK block LU factorization of matrix M is expressed with the form $M = PLU$ where L is a unit lower triangular matrix; here U is the upper triangular matrix whereas P is the permutation matrix. Factorization is achieved by using functions *DGETF2* or *DGETRF* (which is the more time-efficient version). The algorithm in LAPACK is based on the sequence of row interchanges for Gaussian elimination (Kurzak, Luszczek, Faverge and Dongarra, 2013). The formation of such a sequence of operations is referred to as *panel factorization*. Hence, repeated

application of the procedure and descending down the diagonal of the matrix operations of the form $C = C - A \times B$ takes place. Here A is the panel (i.e. a set of columns) without the top n_k rows, B is the top n_k rows of the trailing submatrix, and C is the trailing submatrix without the top n_k rows; k is the iteration index. Panel factorizations would dominate the execution time of the application compared to the execution time of matrix-matrix multiplications. Thus panel factorization delivers performance which is inadequate for LU implementation on hybrid CPU/GPU systems. Usually, it is preferred in order to minimize the work performed by the CPUs in order to prevent GPUs idleness. A fast alternative equivalent to the DGETRF function is proposed in (Kurzak et al., 2013).

It may be noted that decomposing some algorithm into a number of procedures may result in faster implementation provided these procedures are performed by standard functions. An example of this case is a solution of the system of equations of the form $Tx = b$ where $T \in \mathbb{R}^{n \times n}$ is a symmetric block – a Toeplitz matrix and $x, b \in \mathbb{R}^n$. The generalized Schur algorithm which is usually used when solving such systems may be modified so that to parallelize *matrix – matrix* multiplications (Alonso, Arguelles, Ranilla and Vidal, 2013; Alonso, Argueso, Cortina, Ranilla and Vidal, 2013). As a result, the efficiency of BLAS level 3 operations is benefited from.

A number of digital image processing problems such as the estimation of the homography between two sets of points on different planes or the linear method to calibrate a camera from images of planes could be described as the problem of finding the minimal singular value of matrix A of dimensions $m \times n$ (Gerardo de la Fraga, 2015). A new procedure was suggested in (Gerardo de la Fraga, 2015). The paper claims that the novel procedure is faster than the traditional function of LAPACK when calculating the SVD. However, this approach is only applicable for finding no more than one (minimal) singular value. There are many performance improvements for SVD, e.g. (Akhtar and Khan, 2013; Foster, Mahadevan and Wang, 2012; Gunta, Khan, Saha and Pau, 2013). In this framework, it originally takes $O\left(mn^2\right)$ time to compute SVD thus making it a time-costly operation for large matrices.

The most commonly used SVD algorithm on CPU is the QR-iteration (Feng, Jin, Zheng and Zhu, 2014). That is why it is natural for this factorization to be so frequently discussed. Whenever a particular procedure contains a QR operation it is considered as a significant limiter of the performance (Gates, Haidar and Dongarra, 2015). A comprehensive research of QR factorization procedure, its performance and realization in LAPACK could be found in (Van Zee, van de Geijn and Quintana-Orti, 2013). A recursive approach striving to parallelize QR factorization is proposed in (Kaagstrom, Kressner and Shao, 2012). An alternative parallelization strategy is discussed in (Kuznetsov, 2013). A specialized QR procedure delivering eigenvalues in exact pairs or quadruples is suggested by (Salam and Watkins, 2011).

In this work, LAPACK is utilized so that to perform huge amounts of determinant calculations. Standard function DGETRF is referenced via the *dll* (dynamic link library) in C++ code. Algorithms producing patterns of *H*-ranks are

rich in *for* loops. This fact prompted us to use C++ for better performance of the algorithms. Thus executions of C++ codes were carried out on Linux system as Linux is a rather popular choice in the field of science (Stpiczyński, 2015; Xia and Xue-dong, 2012).

2. COMPUTATION OF *H*-RANKS AND THEIR PATTERNS

2.1. Numerical Methods for Computing *H*-ranks and Their Analysis

2.1.1. The Algorithm for the Computation of the *H*-rank

The *H*-rank of a sequence is an effective computational tool for the investigation of the convergence of nonlinear dynamical systems to critical attractors. *H*-ranks computed for initial solutions in the space of a system's parameters and the initial conditions may reveal important physical information about the peculiarities of a system's behavior (Landauskas and Ragulskis, 2012; Ragulskis and Navickas, 2011).

The concept of the *H*-rank of a sequence $\left(p_j; j=0,1,\ldots\right)$; $p_j \in \mathbb{R}$ has been introduced in (Ragulskis and Navickas, 2011).

Let *S* be an infinite sequence of real or complex numbers: $S := \left\{x_r\right\}_{r=0}^{+\infty}$.

A finite subsequence comprising the initial $2k-1$ elements $\left(x_0, x_1, x_2, \ldots, x_{2k-3}, x_{2k-2}\right)$ can be rearranged into the Hankel matrix $H^{(k)}$:

$$H^{(k)} := \left[x_{r+s-2}\right]_{1\le r,s\le k} = \begin{bmatrix} x_0 & x_1 & \cdots & x_{k-1} \\ x_1 & x_2 & \cdots & x_k \\ & & \cdots & \\ x_{k-1} & x_k & \cdots & x_{2k-2} \end{bmatrix} \tag{14}$$

where the superscript k denotes the order of the Hankel matrix. The Hankel transform of the sequence of matrices $\left\{H^{(k)}\right\}_{k=2}^{+\infty}$ yields a sequence of determinants $\left\{\det\left(H^{(k)}\right)\right\}_{k=2}^{+\infty} = \left\{d^{(k)}\right\}_{k=2}^{+\infty}$.

The rank of a discrete sequence is defined in (Ragulskis and Navickas, 2011). It is a natural number m satisfying the following condition (as long as the rank exists): $d^{(m+n)} = 0$ for all $n \in \mathbb{N}$ if only $d^{(m)} \neq 0$. The thesis uses the following notation:

$$HrS = Hr\left\{x_r\right\}_{r=0}^{+\infty} = m. \tag{15}$$

If it is shown that this kind of number m does not exist, it is determined that sequence S does not have a rank: $HrS := +\infty$. Yet if the rank of a discrete sequence does exist, an explicit mathematical model governing the evolution of that sequence can be derived. It is defined that $Hr\left(0,0,0,\ldots\right) = 0$. We should note that $Hr\left(p_0,\ldots,p_m,0,0,0,\ldots\right) = m+1$ if only $p_m \neq 0$ for $m = 0,1,2,\ldots$.

It should be remarked that a chaotic sequence does not have a rank. Otherwise, the dynamics of that sequence would be deterministic because an algebraic model of

this sequence could be derived, which contradicts the definition of a chaotic sequence.

It could be proven that the Hankel rank of a solution of a discrete iterative map can only decrease if a part or the whole transient process from the initial condition is omitted (Ragulskis and Navickas, 2011).

2.1.2. Aspects of Floating Point Arithmetic for the Computation of *H*-ranks

All real numbers are stored in the computer memory as a closest binary number (Kahan, 1996):

$$x = (-1)^s \cdot (1 + Fraction) \cdot 2^{Exp-Bias}.$$

A floating point double word length number is comprised from the *sign bit*, 11 bits for the *Exp* part and 52 bits for the fraction (or the *mantissa*) in 32bit system. The *Bias* is set to 1023; thus the largest power of 2 is $\sum_{i=0}^{10} 2^i - 1023 = 2^{11} - 1 - 1023 = 1024$ while the smallest power of 2 is $0 - 1023 = -1023$. The fraction part is represented as a binary number. Thus the least significant bit equals to $2^{-52} \approx 2.22 \cdot 10^{-16}$. It is usually called the *machine epsilon*. In this case the 16th digit of the mantissa of a real number is approximate.

According to the IEEE Standard for Floating-Point Arithmetic (IEEE 754) technical standard, a number in the 32bit word length system can be referred as the single, double or quadruple format. The formats have the structure of bits for different parts of the binary number as 1-8-23, 1-11-52 and 1-15-112 respectively.

Let us consider the case of number $x = 3.5$. The mantissa inevitably starts with 1 – hence, $x \cdot 2^{-1} = 1.75$ gives $Exp - Bias = 1$ and 0.75 as the fraction. $0.75 = 1 \cdot 2^{-1} + 1 \cdot 2^{-2} + 0 \cdot 2^{-3} + \ldots$. The obtained number is positive, so $s = 0$ and the result is the sequence of bits 0110… in the computer memory (double format in a 32bit system).

Table 1. A number representation in double format

1 (sign)	2-12 (Exp)	13-64 (Fraction)
0	1000...0	11000...0

Finding the exponent involves dividing or multiplying by 2 till the number gets smaller than 2 but larger than or equal to 1. For example, $x \cdot 2^{-n} = \overline{1.b_1 b_2 \ldots b_k} < 2$; it is less than $1 + 2^{-1} + \ldots + 2^{-52} = 2 - 2^{-52}$. The smallest n must be found so that to satisfy this inequality and thus to determine the power n.

$$2^n > \frac{x}{2} \Rightarrow n > \log_2 \frac{x}{2} = \frac{\ln \frac{x}{2}}{\ln 2}. \tag{16}$$

A more efficient way to determine the bits of the mantissa is as follows. 0.75 is greater than 2^{-1} thus 1 goes to the binary representation; $0.75 - 0.5 = 0.25$; 0.25 is greater than or equal to 2^{-2} thus 1 is taken again; $0.25 - 0.25 = 0$; 0 is smaller than

2^{-k}, $k > 2$, thus all bits starting at k are equal to 0. This principle is related to the fact that at a particular position the sum of the mantissa (as of a diminishing geometrical progression) obtained by removing that bit is always less than that particular bit. For example, $1/2$ is more than $1/2^2 + 1/2^3 + \ldots$. The nearest binary representation is used if the mantissa does not have enough bits to exactly represent a particular number.

One more important fact must be mentioned here. Let us consider two floating point numbers differing less than the machine epsilon (for example 2^{-21} and 2^{-20}). It is, of course, possible to perform the arithmetic operations here. Yet, one must be extremely careful while working with the detection of convergence or similar problems. The number might converge and become constant (if the machine epsilon is fixed as being equivalent to zero) in the computer memory; however, the difference between two adjacent numbers might still exist and be less than the machine epsilon. Thus there are problems where certain properties of computer arithmetic are important.

2.1.3. Notes on Finding *H*-rank Using Floating Point Arithmetic

Let us investigate a sequence of numbers: 2.5; -1; 0.25; -0.06; -0.25; 0.1; 0.25; 0.1. Let these numbers be the orbit of a particular map of interest. The corresponding sequence of Hankel matrices is:

$$H^{(1)} = [2.5];\ H^{(2)} = \begin{bmatrix} 2.5 & -1 \\ -1 & 0.25 \end{bmatrix};\ H^{(3)} = \begin{bmatrix} 2.5 & -1 & 0.25 \\ -1 & 0.25 & -0.06 \\ 0.25 & -0.06 & -0.25 \end{bmatrix};$$

$$H^{(4)} = \begin{bmatrix} 2.5 & -1 & 0.25 & -0.06 \\ -1 & 0.25 & -0.06 & -0.25 \\ 0.25 & -0.06 & -0.25 & 0.1 \\ -0.06 & -0.25 & 0.1 & 0.25 \end{bmatrix}.$$

Firstly Matlab was used to find the determinants for each of the matrices above. Calculations resulted in: $d^{(1)} = 2.5$; $d^{(2)} = -0.375$; $d^{(3)} = 0.099125$; $d^{(4)} = 0.07683046$. Usually such results can be considered of acceptable accuracy because here the last digits are much greater than $2^{-52} \approx 2.22 \cdot 10^{-16}$ which is the number represented by the least significant bit in double format.

The floating point arithmetic was simulated here by writing the C++ code for performing "+"; "-"; "*" operations and calculating the determinant of a matrix by performing the product of first row elements and corresponding lower order determinants. The purpose of this course of actions is to find out where computational accuracy is lost and, more importantly, to discover whether that correlates to the properties of the map.

Only for illustrative purposes a custom floating point type is chosen here. 1 bit is dedicated to the sign of a number, 5 bits for the exponent and 6 bits for the

mantissa. Setting 5 bits for the exponent enables us to use $2^{\pm(31-1)/2} = 2^{\pm 15}$ as a maximal factor (because $2^0 + 2^1 + \ldots + 2^4 = 31$). Analogously, one can find the limits for a mantissa.

Table 2. Multiplication in floating point arithmetic

2.5_{10} *	1. 0 1 0 0 0 0	$\cdot 2^1$
0.25_{10}	1. 0 0 0 0 0 0	$\cdot 2^{-2}$
0.625_{10}	1. 0 1 0 0 0 0	$\cdot 2^{-1}$

The trace of this experiment is as follows. $d^{(2)} = -0.34375$ is obtained by performing $2.5 \cdot 0.25 - (-1) \cdot (-1)$.

The result is exact and the accuracy is not lost. The $(-1) \cdot (-1)$ is rather trivial so the next operation is considered.

Table 3. Addition in floating point arithmetic

-1_{10} +	1 1. 0 0 0 0 0	$\cdot 2^0$
0.625_{10}	0. 1 0 1 0 0 0	$\cdot 2^0$
-0.34375_{10}	1. 0 1 1 0 0 0	$\cdot 2^{-2}$

As it is evident, the Matlab result differs more than 0.03 from the one obtained. To continue, $d^{(3)}$ is calculated as follows:

$$2.5 \cdot \left(0.25 \cdot (-0.25) - 0.06 \cdot 0.06\right) -$$
$$-(-1) \cdot \left(-1 \cdot (-0.25) - (-0.06) \cdot 0.25\right) +$$
$$+0.25 \cdot (-1 \cdot (-0.06) - 0.25 \cdot 0.25).$$

Again, some operations do not lose the required accuracy:

Table 4. Multiplication in floating point arithmetic

0.25_{10} *	1. 0 0 0 0 0 0	$\cdot 2^{-2}$
0.25_{10}	1. 0 0 0 0 0 0	$\cdot 2^{-2}$
0.625_{10}	1. 0 0 0 0 0 0	$\cdot 2^{-4}$

However, some operations result in:

Table 5. Multiplication in floating point arithmetic

0.06_{10} *	1. 1 1 1 0 0 0	$\cdot 2^{-5}$
0.06_{10}	1. 1 1 1 0 0 0	$\cdot 2^{-5}$
0.0035095_{10}	1. 1 1 0 0 1 0 1	$\cdot 2^{-9}$

In this case, the resulting number has a longer mantissa than 6 positions. The remaining bit $2^{-7} \cdot 2^{-9} = 2^{-16}$ will not be stored in the resulting number. Depending on the hardware used for the calculations, this remaining bit will most probably be lost. Such accuracy loss is the price for the length of the mantissa being insufficient. Another operation is performed as:

Table 6. Multiplication in floating point arithmetic

0.25_{10} *	1. 0 0 0 0 0 0	$\cdot 2^{-2}$
0.06_{10}	1. 1 1 1 0 0 0	$\cdot 2^{-5}$
0.0146484375_{10}	1. 1 1 1 0 0 0	$\cdot 2^{-7}$

It is not difficult to notice that in certain cases the two added numbers can differ more than the length of a normalized mantissa. By performing addition and normalizing the mantissas in the first place one of the operands becomes zero in the mantissa. Thus it does not act in the operation, and the result will be the greater number of the two. To sum up, the operation in fact lies beyond the machine epsilon and is successfully performed. In other words, operations lie in the exponent. However, the accuracy of the result is lost.

It was decided to fix the number of acceptable accuracy losses while performing calculations of *H*-ranks. $k = n!/2$ proved to be the most informative and universal value obtained experimentally. Here n is the order of the determinant being calculated. Nevertheless, this number is approximately equal to the half of arithmetic operations in calculating the determinant by expanding it to the sum of the product of one row elements and corresponding lower order determinants.

Let us suppose that one needs to calculate the determinant by performing the actions outlined above. If the determinant of order 2 is calculated as the difference of the products of the diagonal elements then there is one subtraction operation. The order 3 determinant requires 2 sums of cofactors and $3 \cdot 1$ subtractions inside each of them. The order 4 determinant requires $3 + 4 \cdot 2$ sums and $4 \cdot 3 \cdot 1$ subtractions and so on. In this respect, the order n determinant requires $(n-1) + n \cdot ((n-2) + (n-1) \cdot ((n-3) + (n-2) \cdot \ldots \cdot 3 \cdot 1))$ sums and $n!/2$ subtractions.

Table 7. Summary on the number of operations

Order n	Total sums of cofactors	Total subtractions of products	Total number of +- operations	$\frac{n!}{2}$
2	0	1	1	1
3	$3 \cdot 0 + 2 = 2$	3	5	3
4	$4 \cdot 2 + 3 = 11$	$4 \cdot 3 = 12$	23	12
5	$5 \cdot 11 + 4 = 59$	$5 \cdot 4 \cdot 3 = 60$	119	60

As seen from the table, $n!/2$ is approximately half of the sum and subtraction operations involved in finding the cofactor expansion for a particular determinant. The total number of these operations is $n!-1$.

2.1.4. The Computation of Pseudoranks

In order to determine the rank of the sequence, one needs to find such a matrix dimension ($\overline{m}+1$) that the determinant of the Hankel matrix is equal to zero. In practice it is sufficient to compute determinants up to certain precision ε like the machine epsilon. Calculating a determinant of a square real matrix requires a fair amount of computer resources if the dimension of a matrix is large. Moreover, the determinant, despite being a conventional notion theoretically, rarely finds a useful role in numerical algorithms (Trefethen and Bau III, 1997).

Plotting patterns of *H*-ranks requires massive computations of determinants of Hankel matrices. Thus instead of using the standard straightforward function *det* in Matlab, here C++ and the LAPACK package are employed to perform the computation of the determinants of Hankel matrices.

LAPACK is installed as a set of DLLs. In order to use the libraries in the C++ code, LAPACK must be linked to them. Linking is performed by passing arguments to the compiler. Additionally, function headings with word extern must be defined at the beginning of the file. The word extern tells the compiler that the corresponding functions are defined in another file. The compiler will find that file via #include statement and the linked libraries.

Although LAPACK can be considered as being state-of-the-art in linear algebra, it does not feature a standard subroutine for the computation of the determinant. Instead, the standard PLU decomposition (function *dgetrf()*) of a matrix into the lower triangular matrix *L* (having 'ones' on the main diagonal), the upper triangular matrix *U* and the permutation matrix *P* is performed. LAPACK's function *dgetrf()* produces three matrices:

$$L=\begin{bmatrix} 1 & 0 & \dots & 0 \\ l_{21} & 1 & \dots & 0 \\ \dots & \dots & \ddots & \dots \\ l_{m1} & l_{m2} & \dots & 1 \end{bmatrix};\ U=\begin{bmatrix} u_{11} & u_{12} & \dots & u_{1m} \\ 0 & u_{22} & \dots & u_{2m} \\ \dots & \dots & \ddots & \dots \\ 0 & 0 & \dots & u_{mm} \end{bmatrix};\ P_{piv}=\begin{bmatrix} p_1 \\ p_2 \\ \vdots \\ p_m \end{bmatrix}. \tag{17}$$

In fact, L and U are stored in one matrix, which is possible due to their triangular structure. P_{piv} elements represent the index of row p_i to be interchanged with row i. Thus P_{piv} could be transformed into permutation matrix P having single 'ones' in each line. The original matrix H now is decomposed as $H=LUP$.

$$\left|d^{(m)}\right|=|LUP|=|L|\cdot|U|\cdot|P|=1\cdot|U|\cdot 1=\prod_{i=1}^{m}u_{ii}\ . \tag{18}$$

The absolute value of the determinant of the original matrix equals to the product of elements on the main diagonal of U (Eq. (18)). The number of permutations determines the sign of the determinant of the original matrix. But since the main interest lies in the absolute value of the determinant only, it suffices to compute the product of the diagonal elements of U. An alternative approach could be counting the number of non-zero diagonal elements. The computation of determinants continues until the absolute value of the product of diagonal elements of matrix U is less than ε . In this respect, such computations reveal not the rank but rather the pseudorank of a sequence instead.

It must be noted that the leading dimension is the second dimension in LAPACK. Consequently, all matrices must be transposed while defining the initial data or analyzing the final results.

The combination of the speed of C++ in performing loops (opposite to Matlab) and the mathematical precision of LAPACK resulted in significantly faster formation of images of H-ranks in various phase planes. It can be noted that the final visualization is performed by using the functionality of Matlab graphical functions.

The selection of a particular value of ε requires additional attention and is discussed in the next section.

2.2. Computational Reconstruction of the Patterns of *H*-ranks

2.2.1 Applications of *H*-ranks for the Circle Map

Computational techniques based on the ranks of Hankel matrices (H-ranks) are used so that to study the convergence to Arnold tongues in the circle map. It appears that the process of convergence to the phase-locked mode of the discrete stationary attractor is far from being trivial. Figures of pseudoranks of Hankel matrices constructed from transient solutions of the circle map carry important physical information about complex nonlinear processes and are also beautiful from the aesthetic point of view.

The main objective of this chapter is to show that the concept of the H-rank can be effectively used for the investigation of convergence properties of the circle map. The insight into the embedded algebraic complexity of the nonlinear system is revealed by computing and visualizing H-ranks in the space of a system's parameters and the initial conditions. It is shown in (Ragulskis and Navickas, 2011) that the computation of Hankel ranks can be successfully used in order to identify and assess the sensitivity of nonlinear systems to initial conditions and can be used as a simple and effective numerical tool for qualitative investigation of the onset of chaos for discrete nonlinear iterative maps.

The discrete iterative circle map is used here to illustrate the process of convergence to stationary states. The circle map is a paradigmatic model of a nonlinear iterative dynamical system used for the study of the dynamical behavior of a beating heart (Glass, Guevara, Shrier and Perez, 1983). It is shown here that the study of the convergence rate to a periodic orbit of the circle map can produce beautiful and appealing patterns. Moreover, these graphical pictures contain important information on the stability of the periodic orbits of the circle map. This information could be useful whenever the manipulation or control of quasiperiodic

nonlinear systems could be considered (Landauskas, Ragulskienė and Ragulskis, 2012; Landauskas and Ragulskis, 2013).

The main purpose of this section is to investigate the properties of the *H*-rank of a solution of a discrete iterative map when transient processes are omitted and the system approaches a periodic or a quasiperiodic orbit.

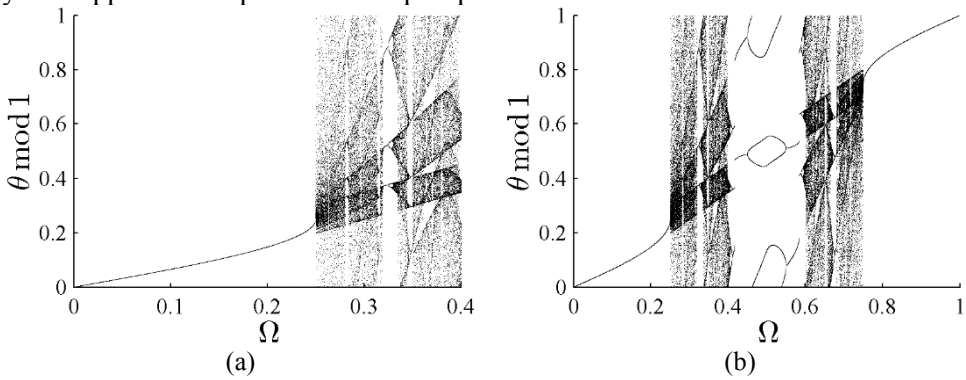

Fig. 3. The bifurcation diagram for the circle map at $K = \pi/2$. The first 10000 orbit points are omitted

The circle map $\theta_{n+1} = f(\theta_n)$ defined previously as Eq. (1) is used in this section. Fig. 3 shows the bifurcation diagram for the circle map. The symmetry of the bifurcation diagram can suggest that we should perform a research into the subset of the domain of Ω. However, this may not apply to the transients – and it is important when clocking convergence.

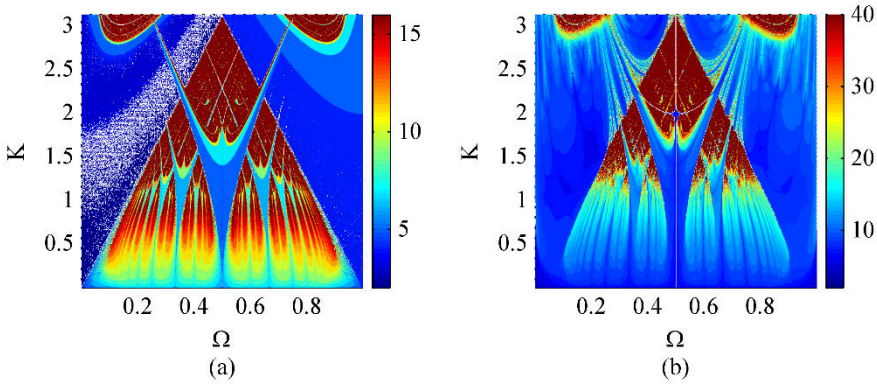

Fig. 4. Pseudoranks of the circle map. Part (a) was constructed while omitting transient processes, and the initial phase was set at $\theta_0 = 0.5$; part (b) was constructed without omitting transient processes

The *H*-rank as the computational tool for the reconstruction of Arnold tongues will be used here. At first, *H*-ranks in the region $0 \le \Omega \le 1$ and $0 \le K \le \pi$ are computed. For each and every pair of Ω and K, the iterative process is started and the sequence $\{\theta_j\}$; $j = 0,1,\ldots$; is constructed; the initial condition θ_0 is set at the level of 0.5. Then the *H*-rank of the obtained sequence is calculated. As shown in

(Ragulskis and Navickas, 2011), the *H*-rank of a chaotic sequence does not exist (then we consider *H*-rank as equalling infinity). Therefore, the upper limit for the *H*-rank $\overline{m} = 40$ is set. If the sequence of determinants does not vanish until $m = 40$, the process is terminated assuming that $Hr\{p_j\} = \overline{m}$; $j = 0,1,\ldots$. The obtained results are shown in Fig. 4(b).

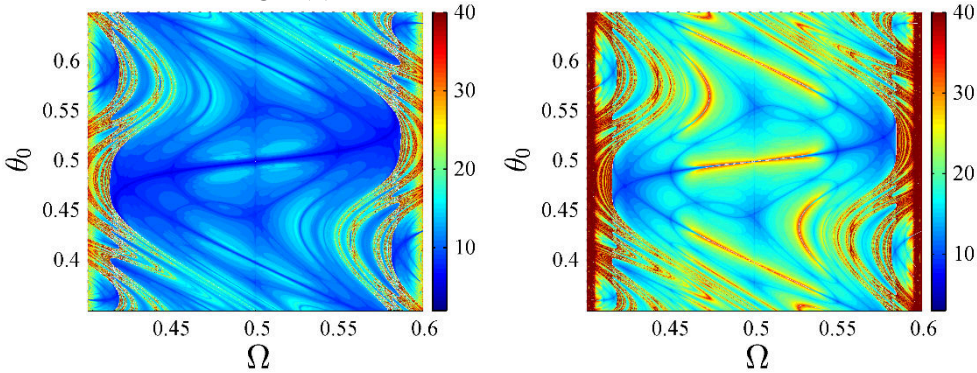

(a) (b)

Fig. 5. Maps of pseudoranks in the zoomed area of the widest Arnold tongue for various parameter values ($0.4 \le \Omega \le 0.6$, $0.35 \le \theta_0 \le 0.65$ and $K = 0.5\pi$) at (a): $\varepsilon = 2.22 \cdot 10^{-16}$; (b): $\varepsilon = 10^{-50}$; $\overline{m} = 40$

The more elements of the sequence $(\theta_j; j = 0,1,\ldots)$ are considered (leading to possible higher *H*-ranks of the sequence), the more the resulting picture is alike to the well-known shape of Arnold tongues in the circle map (Schilder and Peckham, 2007).

Previously discussed aspects of computer arithmetic in the performed computations could be noticed when comparing Fig. 5(a) and (b). The floating point standard was explored in order to explain the fact of successful calculations down below the limit of the machine epsilon, and Fig. 5(b) is a clear proof of that. By decreasing the value of ε, some values of *H*-ranks increase. This results in higher order determinants being considered in the Hankel transform. The *H*-ranks in between those obtained by using machine epsilon (Fig. 5(a)) and $\overline{m}$ suggest that one will get interpretable results by using ε smaller than the machine epsilon.

The pattern from Fig. 5(a) is used here in order to demonstrate the use of the LAPACK package in computations. The dimensions of the pattern are fixed to 800×800 .

Table 8. A comparison of the speed of computation for patterns of *H*-ranks

Software	Platform	Approximate relative time, %
C++ with LAPACK	Linux Arch on *VirtualBox*	7
Matlab	Windows 8.1	100
Matlab (parfor, 2 workers)	Windows 8.1	28

Matlab (parfor, 3 workers)	Windows 8.1	36
Matlab (parfor, 4 workers)	Windows 8.1	41

Table 8 summarizes the experiment of computing a large number of patterns of *H*-ranks for the circle map. The employed computer had a 2.1 GHz *Intel i7* processor with 4 cores and 8 GB of random access memory. The results actually speak for themselves by showing the C++ and the LAPACK approach as being the fastest. Matlab's parallel loop *parfor* decreases in terms of performance if the number of workers is increased. This is due to the complexity of the algorithm and the resulting communication between the threads. The LAPACK approach was also compiled on the Windows platform but that did not outperform the Linux approach.

2.2.2. Selecting the Optimal Value of ε for Patterns of *H*-ranks

As mentioned previously, the structure of Arnold tongues in the circle map is well-known. The computation of pseudoranks for different initial conditions ($0 \le \Omega \le 1$, $0 \le K \le \pi$ and $\theta_0 = 0.5$) is performed for a variety of ε. The obtained results are illustrated in Fig. 6. The evolution of more interesting patterns of pseudoranks can be observed as the value of ε decreases (we should note that the maximum rank in colorbars is detected automatically and depends on ε).

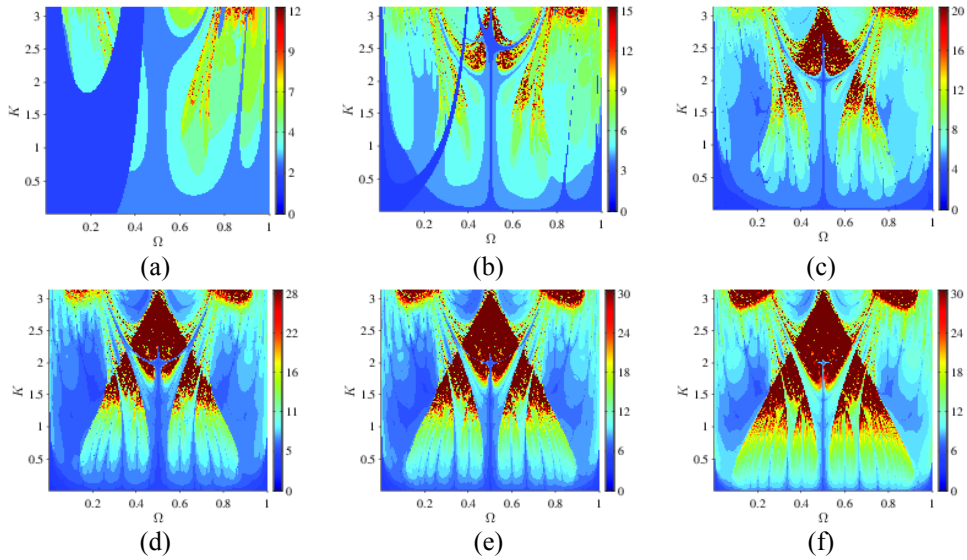

Fig. 6. Maps of pseudoranks for a variety of parameter values ($0 \le \Omega \le 1$, $0 \le K \le \pi$ and $\theta_0 = 0.5$) at (a): $\varepsilon = 10^{-1}$; (b): $\varepsilon = 10^{-2}$; (c): $\varepsilon = 10^{-4}$; (d): $\varepsilon = 10^{-8}$; (e): $\varepsilon = 10^{-12}$; (f): $\varepsilon = 10^{-20}$

The naked eye cannot see principal differences between Fig. 6(e) and Fig. 6(f). At this point, one can only fix the value of ε and use it for the construction of maps of pseudoranks. An analogous selection could be made by using, for example, the phase plane $0 \le \Omega \le 0.4$, $0 \le \theta_0 \le 0.4$ and $K = \pi/2$ (Fig. 7). It depends on which parameters the *H*-ranks need to be computed in that respect.

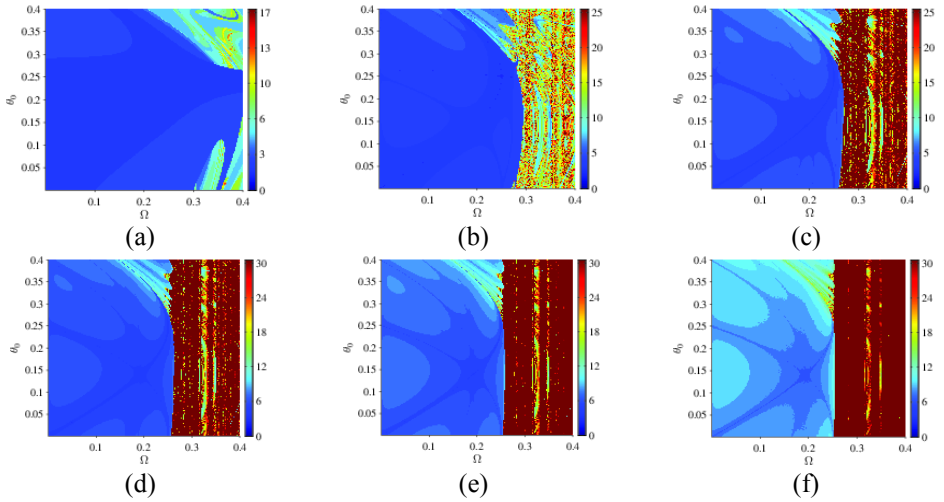

Fig. 7. Maps of pseudoranks for a variety of initial conditions ($0 \le \Omega \le 0.4$, $0 \le \theta_0 \le 0.4$ and $K = \pi/2$) at (a): $\varepsilon = 10^{-2}$; (b): $\varepsilon = 10^{-5}$; (c): $\varepsilon = 10^{-10}$; (d): $\varepsilon = 10^{-16}$; (e): $\varepsilon = 10^{-25}$; (f): $\varepsilon = 10^{-50}$

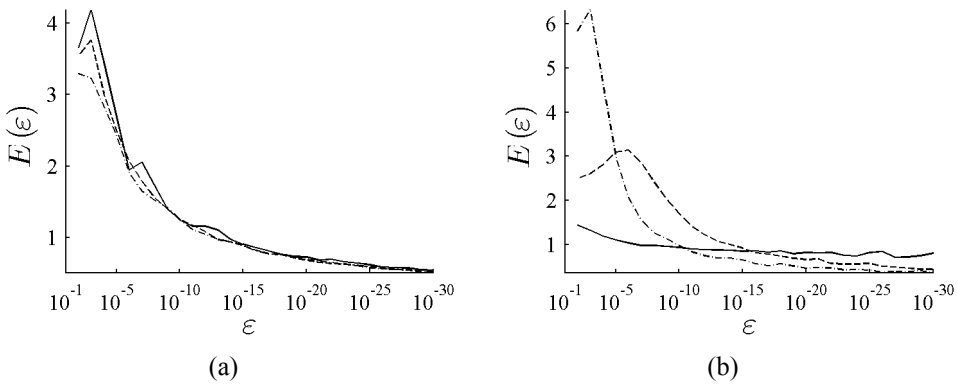

Fig. 8. The relationship between the absolute root mean square difference E and the ε value at $m = 30$. The calculations were performed by using parameter plane $\Omega - K$ of dimensions $[0;1]\times[0;\pi]$ (a) (here, the solid line represents the variation of E at $\theta_0 = 0.25$; the dash line shows values at $\theta_0 = 0.5$; the dott-and-dash line presents results at $\theta_0 = 0.75$) and $\Omega - \theta_0$ of dimensions $[0;1]\times[0;1]$ (b) (the solid line represents the variation of E at $K = 0.25\pi$; the dash line shows the variation at $K = 0.5\pi$; the dot-and-dash line depicts the results at $K = 0.75\pi$)

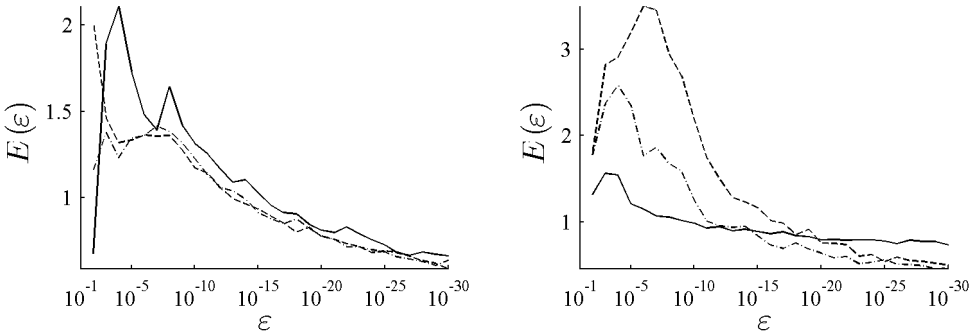

(a) (b)

Fig. 9. The relationship between the absolute root mean square difference E and the ε value at $m = 30$. The calculations were performed by using the parameter plane $\Omega - K$ of dimensions $[0;0.4]\times[0;0.5\pi]$ (a) (the solid line represents the variation of E at $\theta_0 = 0.25$; the dash line represents the level $\theta_0 = 0.5$; the dot-and-dash line describes $\theta_0 = 0.75$) and $\Omega - \theta_0$ of dimensions $[0;0.4]\times[0;0.4]$ (b) (the solid line represents the variation of E at $K = 0.25\pi$; the dash line represents the level $K = 0.5\pi$; the dot-and-dash line describes $K = 0.75\pi$)

Any particular selection of the value for ε must be valid. In order to achieve this, the graph representing the absolute root mean square difference E between consecutive maps of pseudoranks in Fig. 6 is constructed. Let us denote $Hr_1(i,j)$ the value of the pseudorank at the i-th row and the j-th column of the map of pseudoranks computed at ε_1 (analogously, $Hr_2(i,j)$ is the pseudorank at ε_2). Then, difference E is defined as Eq. (19).

$$E(\varepsilon_2) = \sqrt{\frac{1}{mn}\sum_{i=1}^{n}\sum_{j=1}^{m}\left(Hr_1(i,j) - Hr_2(i,j)\right)^2}\ ; \tag{19}$$

where m is the number of rows and n is the number of columns in maps of pseudoranks. Relationship $E(\varepsilon)$ is shown in Fig. 8. It can be clearly seen that maps of pseudoranks do not change considerably beyond $\varepsilon = 10^{-25}$ and that the limit of accuracy of double floating point arithmetic is reached.

The graph representing E between consecutive maps of pseudoranks on the subset of the parameter plane $\Omega - K$ at $[0;0.4]\times[0;0.5\pi]$ (Fig. 6) was also constructed. In this case, the detail of the parameter plane improves more after the limit of accuracy of double floating point arithmetic.

2.3. Conclusions

The floating point arithmetic of computation of a determinant was explored in this chapter.The obtained results provided explanatory insight into the fact that *H*-rank computations are performed successfully below the limit of accuracy of double floating point arithmetic. This not-so-trivial fact was demonstrated by performing

numerical experiments. It was shown that choosing the error value as approximately equal to the machine epsilon is optimal in terms of the visual quality of the patterns of *H*-ranks for the circle map. The optimal error value for other nonlinear systems might be different and should be determined separately.

The method discussed in this section consists of two steps and can be used for visualizing Arnold tongues themselves. Firstly, the system is iterated for a predetermined number of steps from the initial conditions. Then one does not need to search for the effect of the phase locking. Then, simple computation of the *H*-rank of the stationary signal is performed and Arnold tongues occur in the patterns of pseudoranks. Thus the quality of phase diagrams is crucial whenever the manipulation or control of quasiperiodic nonlinear systems is considered.

A much more interesting question arises concerning the convergence properties of the circle map to Arnold tongues. It has been shown previously that pseudoranks of transient processes may reveal important physical information about the properties of a discrete system. For example, it has been shown in (Boyland, 1986) that one can observe the stable, the unstable manifold and the manifold of nonasymptotic convergence in the plotted phase diagrams of the Logistic map. In this section, the *H*-rank of the transient processes of the circle map was used for the visualization of the rate of convergence to the Arnold tongues. The optimal selection of ε value was considered.

3. MANIFOLDS OF CONVERGENCE AND THEIR APPLICABILITY FOR THE CONTROL OF NONLINEAR SYSTEMS

The algorithm for the computation of the *H*-rank of a sequence and its properties was investigated in previous sections. In order to achieve its objectives, the present chapter is organized as follows. Section 3.1 deals with the most general issues of the Chapter. The concept of the manifold of non-asymptotic convergence is introduced in Section 3.2. Computational aspects of the patterns of *H*-ranks near the manifold of non-asymptotic convergence are discussed in Section 3.3. Then, pseudo manifolds in the bouncer system and manifolds of convergence in a stroboscopic representation of a nonlinear mathematical pendulum's solution are investigated. The obtained pseudo manifolds were later used for controlling unstable periodic orbits and clocking convergence to a limit cycle. Methods for the control of discrete as well as continuous dynamical systems are discussed in Sections 3.7 and 3.8. Concluding remarks are outlined in the last section.

3.1. Stable Manifolds, Unstable Manifolds and Manifolds of Non-asymptotic Convergence

Let us consider a discrete iterative system. The manifold of non-asymptotic convergence is defined as a set of initial conditions leading to a periodic regime in a finite number of forward iterations. We should note that the entire set of initial conditions can be classified into the subset of initial conditions converging asymptotically to a stable periodic attractor (if only such an attractor exists) and into the subset of initial conditions converging non-asymptotically to a periodic regime (either stable or unstable) (Ragulskis and Navickas, 2011). One of the primary objectives of this chapter is to explore whether the manifold of non-asymptotic convergence does exist in the stroboscopic representation of the model of a periodically driven pendulum.

Convergence to a stable limit cycle of a periodically driven nonlinear pendulum is analyzed in this chapter. The concept of the *H*-rank of a scalar sequence is used for the assessment of transient processes of the system. The circle map is used to illustrate the complex structure of the manifold of non-asymptotic convergence to a fixed point. The pattern of *H*-ranks in the space of a system's parameters and initial conditions is used for the demonstration that the manifold of non-asymptotic convergence exists in the stroboscopic representation of the transient data of the periodically driven nonlinear pendulum. This manifold is used for the construction of a simple method based on a short external impulse for the control of transient processes when the transition time to stable limit cycles must be minimized.

The Hankel rank (*H*-rank) of a scalar sequence reveals the complexity of the algebraic model describing the evolution of that sequence. The *H*-rank has been successfully used for the identification of manifolds of non-asymptotic convergence and for qualitative investigation of the onset of chaos for discrete nonlinear iterative maps.

3.2. The Manifold of Non-asymptotic Convergence and the *H*-rank

As mentioned previously, the main objective of this chapter is to show that the manifold of non-asymptotic convergence exists in the stroboscopic representation of the transient data of the periodically driven nonlinear pendulum. But before continuing with the model of the nonlinear pendulum, the functionality of the *H*-rank technique on the iterative circle map $\theta_{n+1} = f(\theta_n)$ is demonstrated (see Eq. (1)). Initially, the circle map will be investigated here when Ω is set at 0.15.

Let us investigate the stable period-1 regime:

$$\theta^* = f(\theta^*); \tag{20}$$

where θ^* is the stable period-1 phase at $\Omega = 0.15$ and $K = 1$ (the stable period-1 regime exists in this case). The convergence to the stable period-1 regime can be asymptotic ($\lim_{n\to\infty}\theta_n = \theta^*$) or non-asymptotic (when a finite number of forward iterations brings the system into the stable period-1 regime (Bresten and Jung, 2009)). The non-asymptotic convergence to the stable period-1 regime can be explored by solving the inverse relationship

$$\theta_n = f^{-1}(\theta_{n+1}); \tag{21}$$

assuming that $\theta_{n+1} = \theta^*$. We should note that Eq. (21) can be iterated backwards for any number of steps. Iterative nonlinear root finding algorithms (the bisection method and Matlab software) are exploited for solving Eq. (21) since it is a transcendental equation. One backward step yields the value of θ_n bounded in the interval:

$$\theta_n \in \left[\theta^* - \Omega - \frac{K}{2\pi}; \theta^* - \Omega + \frac{K}{2\pi}\right]. \tag{22}$$

If Eq. (21) has the only solution $\theta_n = \theta^*$ then the manifold of the non-asymptotic convergence is an empty set. Such a situation is illustrated in Fig. 10 where Fig. 10(a) shows one backward iteration from $n = 0$ to $n = -1$. The root finding process of Eq. (21) is illustrated in Fig. 10(b) – there other roots do not exist except for θ^* at $\Omega = 0.15$ and $K = 1$.

The situation becomes much more complex at $\Omega = 0.15$ and $K = 1.25$ (Fig. 10(c)). It can be seen that Eq. (21) produces 3 roots; we should note that the root finding process is illustrated only for $n = -1$ in Fig. 10(d). One root corresponds to the stable period-1 regime (the black line connecting the step number -1 with the step number 0 in Fig. 10(c)). Another two roots represent such values of θ_{-1} which evolve into $\theta_0 = \theta^*$ in one forward step (the gray lines in Fig. 10(c)). It is of interest to note that the continuation of backward iterations produces new roots grouped into two branches which tend to converge as the number of backward iterations increases. Thus the manifold of non-asymptotic convergence is an infinite countable

set of discreet initial conditions which lead to the stable period-1 regime in a finite number of forward iterations.

The root finding process becomes even more complex at $\Omega = 0.15$ and $K = 2.5$ (Fig. 10(e)). Let us note that the middle root at $n = -1$ generates three roots at $n = -2$. Such a situation occurs only once; four different branches of backward roots tend to converge as backward iterations are continued. Finally, the situation becomes very complicated at $\Omega = 0.15$ and $K = 3$ (Fig. 10(g)). Triples of backward roots are generated in an almost unpredictable manner as backward iterations are continued.

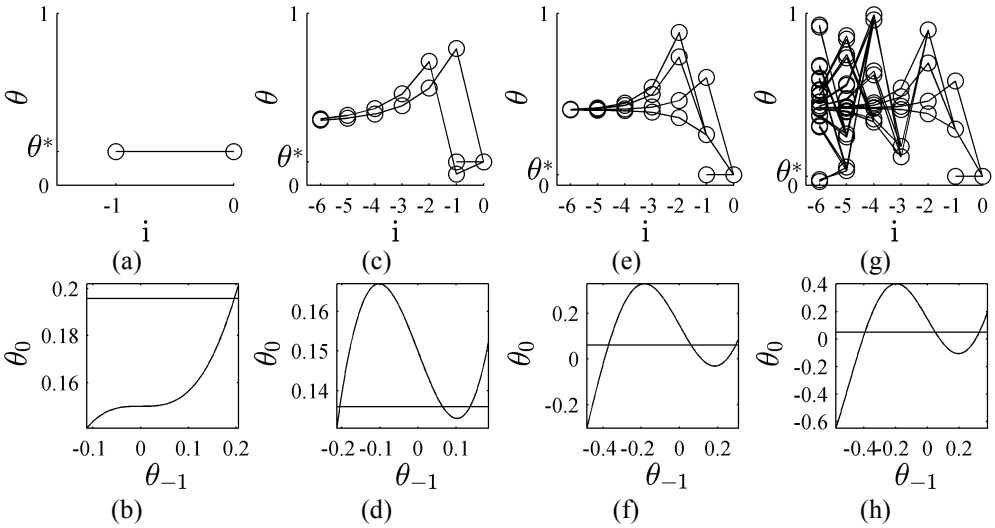

Fig. 10. The construction of the manifold of non-asymptotic convergence to the stable period-1 regime. There are no other initial conditions except for the fixed point itself leading to the period-1 regime in a finite number of forward steps at $\Omega = 0.15$ and $K = 1$ (part (a)). Parts (c), (e) and (g) show the manifold at $\Omega = 0.15$, $K = 1.25$, $K = 2.5$ and $K = 3$ respectively. Parts (b), (d), (f) and (h) illustrate the root finding process: horizontal lines represent $\theta_0 = \theta^*$; curved lines stand for $f(\theta_{-1})$

Let us consider once more the circle map when Ω is set at 0.15 and K varies in the interval $[0;\pi]$ (Fig. 11(a)). A considerable number of iterates ($k = 4000$) is omitted until initial transients terminate for every discrete value of K. The rational number $\Omega = 0.15$ yields a periodic regime at $K = 0$. Yet the system experiences complex quasi-periodic transitions at increasing values of K until it falls into a stable period-1 mode (at K around 1). The further increase of K results into a cascade of period doubling bifurcations leading into the onset of chaos (Fig. 11(a)).

The manifold of the non-asymptotic convergence is visualized in Fig. 11(b). The thick solid red line denotes the stable period-1 regime. The thick dashed red line represents the unstable period-1 regime which occurs after the first period-doubling bifurcation (Fig. 11(a)). All solid black lines represent the manifold of the non-asymptotic convergence to the period-1 regime (either stable or unstable). The thickest solid black lines (the width is set at 6 pixels) illustrate the initial conditions

resulting in the period-1 regime in one forward step. 5 pixel-wide solid black lines illustrate the initial conditions resulting in the period-1 regime in two forward steps; 4 pixel-wide lines lead to three forward steps and so on. As mentioned previously, the interval of the initial conditions $\theta_0 \in [0;1]$ (at fixed Ω and K) can be classified into two sets: the infinite uncountable set of initial conditions converging asymptotically to θ^* as n tends to infinity and the infinite countable set of initial conditions resulting into θ^* in a finite number of forward steps (if only the stable period-1 regime exists). Fig. 11(b) is a clear illustration of such a classification.

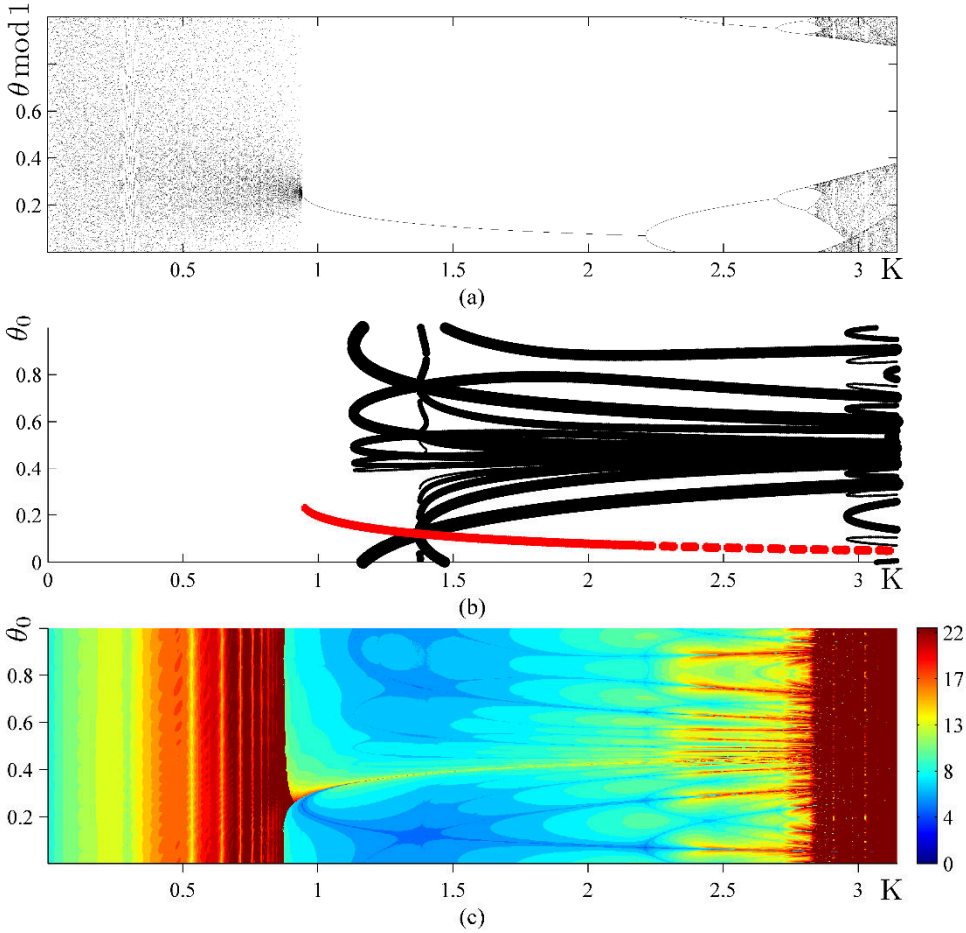

Fig. 11. The bifurcation diagram of the circle map is shown in part (a) at $\Omega = 0.15$. The manifold of non-asymptotic convergence to the period-1 regime is illustrated in part (b). The thickness of black solid lines in (b) illustrates the number of forward iterations required to reach the period-1 regime; the red solid line stands for the stable period-1 regime; the red dashed line stands for the unstable period-1 regime which occurs after the first period-doubling bifurcation. The map of pseudoranks is shown in (c). All computations are performed at $\Omega = 0.15$

It has been shown in (Ragulskis and Navickas, 2011) that the *H*-rank can be used as an effective computational tool for the construction of the intertwined pattern of the stable and the unstable manifold as well as the manifold of the non-asymptotic convergence. Computational experiments for the circle map are performed, and *H*-ranks in the region $0 \le \theta_0 \le 1$ and $0 \le K \le \pi$ are computed at fixed $\Omega = 0.15$. For every pair of θ_0 and K, the sequence $\left(\theta_j; j = 0,1,\ldots\right)$ is constructed and the *H*-rank of that sequence is derived. The results are shown in Fig. 11(c). The manifold of the non-asymptotic convergence to the period-1 regime can be clearly seen in Fig. 11(c) (the transient process is short due to the non-asymptotic convergence to the stable period-1 regime and thus the *H*-rank is low there).

The manifold of non-asymptotic convergence for the circle map (Fig. 11(c)) is constructed by using the computational technique based on *H*-ranks. One could raise a question whether the manifold of non-asymptotic convergence could be constructed by performing a straightforward calculation of the number of steps of convergence to the stationary state instead.

In general, the applicability of the *H*-rank technique has a number of important advantages if compared to the calculation of the number of steps. First of all, one does not have to consider the type of the stable attractor when applying the *H*-rank technique. We should note that Fig. 11(b) is constructed by counting backward steps from the period-1 regime as the construction of the manifold of non-asymptotic convergence to the period-2 stable regime would be much more complex. Yet the *H*-rank technique measures the complexity of transient processes; the manifold of non-asymptotic convergence is constructed simultaneously for all the existing attractors.

Secondly, the *H*-rank technique automatically reveals the manifold of non-asymptotic convergence to unstable periodic regimes (if only they do exist). For example, a transient process can converge non-asymptotically to the unstable period-1 regime at $K = 2.5$ (Fig. 11(c)). Backward iterations from the unstable period-1 regime allow the construction of the manifold of non-asymptotic convergence to the unstable fixed point (Fig. 11(b)). However, the identification of such non-asymptotic convergence would be complicated if the counting of forward steps would be used simply because a stable period-2 regime and the unstable period-1 fixed point coexist at K = 2.5.

Finally, the *H*-rank technique allows identifying zones of regularity surrounded by complex chaotic processes in the parameter plane (at $K = 0.88$ and $K = 2.84$ in Fig. 11(c)). Such identification would be nearly impossible when using straightforward calculation of the number of steps of convergence to a stationary state because the type of the attractor is not known at the beginning of the computational experiment.

3.3. The Quality of *H*-ranks Near the Manifolds of Convergence

A comparison between Fig. 8 and Fig. 9 shows that the distribution of accuracy of computations may not be uniform over the parameter plane. One of the essential elements of a particular parameter plane is the stable and unstable manifolds. Vicinities of these manifolds contain orbits of different dynamical

qualities. These differences can also be explained as differences in terms of complexity which in turn has an effect on the accuracy of the computations.

Such a heuristic argument is explored further by constructing the manifolds of convergence for the circle map and comparing them to the plots of accuracy loss detection of pseudorank calculations. Accuracy loss is considered here as the arithmetic operation "+" (or "-") as long as it implies the relation $a+b=a$; $a \neq 0$, $b \neq 0$. As discussed before, this happens when a and b differ more than the length of a mantissa. Finding the operations where operands differ more than 2 or 3 lengths of a mantissa also proved to be an informative measure regarding the accuracy loss.

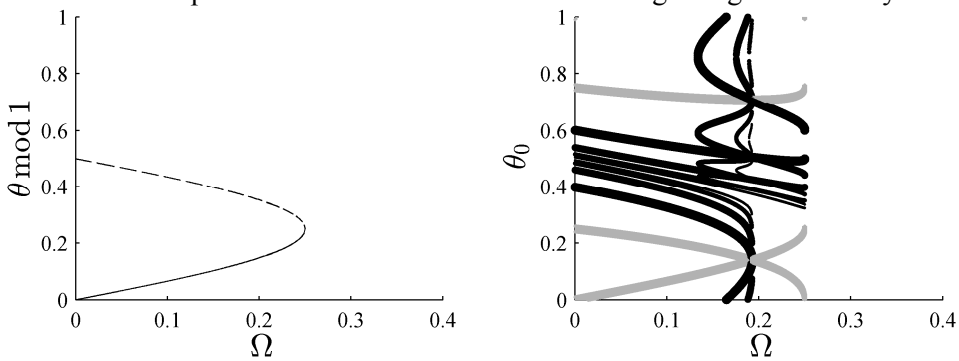

(a) (b)

Fig. 12. (a) The stable (solid line) and the unstable (dashed line) manifolds for the circle map at $K=\pi/2$. (b) The manifold of non-asymptotic convergence to the period-1 regime at $K=\pi/2$. The thickness of black solid lines in (b) illustrates the number of forward iterations required to reach the period-1 regime; the gray solid line stands for period-1 regimes

In order to construct stable and unstable manifolds, one needs to find the fixed points of the map. By solving $f(\theta)=\theta$, the fixed points $\theta=(-1)^k \frac{1}{2\pi}\left(arcsin\frac{2\pi\Omega}{K}+\pi k\right)$, $k \in \mathbb{Z}$ are obtained. Previous computations were performed on the domain $[0;1]\times[0;1]$ (or a subset of it) on the plane $\Omega - K$. Thus $k=0$ is fixed; hence we get the following equations for stable and unstable manifolds:

$$\theta=\begin{cases} \frac{1}{2\pi}arcsin\frac{2\pi\Omega}{K}, \\ \frac{1}{2\pi}\left(\pi - arcsin\frac{2\pi\Omega}{K}\right). \end{cases} \tag{23}$$

Fig. 12 represents a comparison of constructed manifolds to the manifold of non-asymptotic convergence. The plot of accuracy loss detection in Fig. 13(b) shows the minimal order of the determinant calculated with at least $n!/2$ accuracy losses in arithmetic operations. If the manifold of non-asymptotic convergence is

compared to the plot of accuracy losses (Fig. 13(b)), some interesting similarities may be seen.

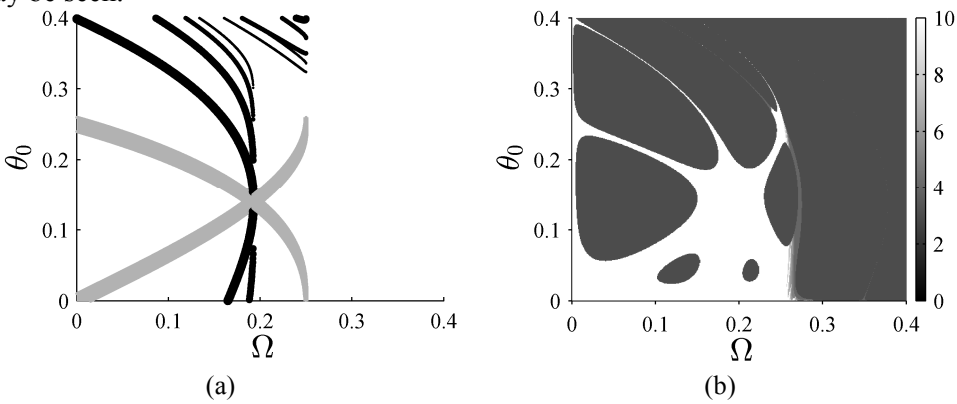

Fig. 13. The comparison of the manifold of non-asymptotic convergence (to the period-1 regime) with the plot of accuracy loss detection ($\varepsilon = 10^{-16}$, $K = \pi/2$, $k = n!/2$)

A part of the manifold corresponds to the initial conditions leading to fewer accuracy losses mentioned above. This fact suggests that one must pay more attention to the various manifolds whenever the quality and detail of the parameter planes is considered. The other areas of the parameter plane correspond to the majority of accuracy losses. A logical explanation for this result might be the heuristic argument mentioned before. An orbit which is relatively far from the manifold of convergence tends to act more chaotically which in turn leads to higher order determinants being considered.

3.4. Non-asymptotic Convergence and the Logistic Map

3.4.1. Classification of Manifolds for the Logistic Map

A well-known one-dimensional Logistic map is defined by:

$$x_{k+1} = rx_k\left(1 - x_k\right);\ k = 0,1,2,\ldots; \tag{24}$$

where $0 \le r \le 4$ and $0 \le x_0 \le 1$; otherwise x_k would be unbounded.

In order to construct the manifold of the non-asymptotic convergence for the Logistic map one needs to perform the following procedure. Taking into consideration the value of r , a corresponding stable fixed point $x^* = 1 - r^{-1}$ is found at first. Then two points $x_{-1}^{(1,2)}$ are computed according to Eq. (25) by considering $x^* = r \cdot x_{-1}^{(1,2)}\left(1 - x_{-1}^{(1,2)}\right)$. When redefining $x_{n+1} := x_{-1}^{(1,2)}$, a set of successive points is computed. The process is continued recursively. Thus x^*_i , $i = -1,-2,\ldots$ are initial conditions leading to the stable fixed point x^* in exactly i iterations.

$$x_{-1}^{(1,2)} = \frac{r \pm \sqrt{r^2 - 4rx^*}}{2r}. \tag{25}$$

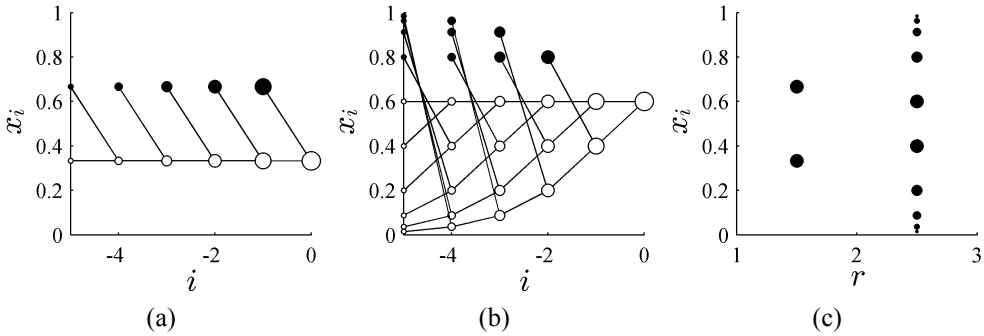

Fig. 14. Backward iterative steps for the Logistic map. Part (a) shows iterations originating at the fixed point x_0 when $r = 1.5$; part (b) represents $r = 2.5$. The same set of points is shown in a single line at a particular r value in part (c); the weight of a point decreases with each backward iteration

Fig. 14 shows the iterative process discussed above. Fig. 14 (c) summarizes Fig. 14(a) and (b) by plotting every point in a single line in respect of r.

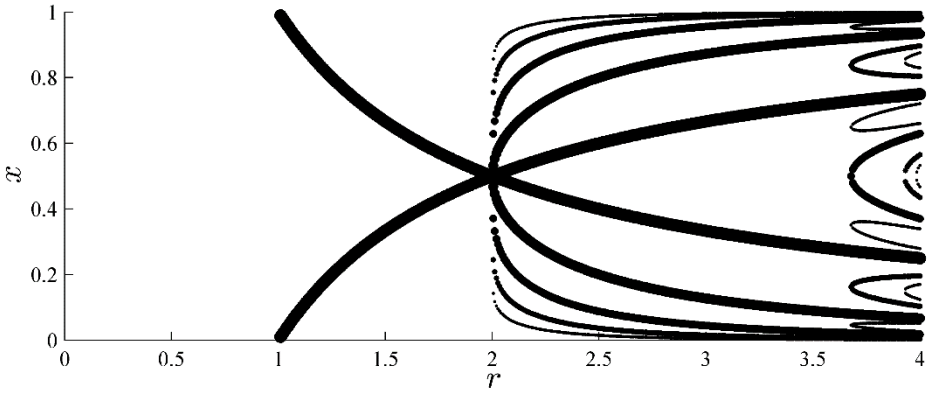

Fig. 15. The manifold of non-asymptotic convergence for the Logistic map. The thickness of lines is inversely proportional to the number of steps required to reach a fixed point

Considering the continuous variation of parameter r, the structure depicted in Fig. 15 represents the manifold of the non-asymptotic convergence for the Logistic map. The manifold is obtained by considering a continuous set of values for parameter r in an analogy to Fig. 14(b).

Stable and unstable manifolds cannot be found directly for nonlinear maps. An approximation could be found when using a computer.

3.4.2. Non-asymptotic Convergence in the Logistic Map

Let us consider a stable period-2 orbit at $r = 3.2$ for the Logistic map. We should note that the Logistic map is a non-invertible map.

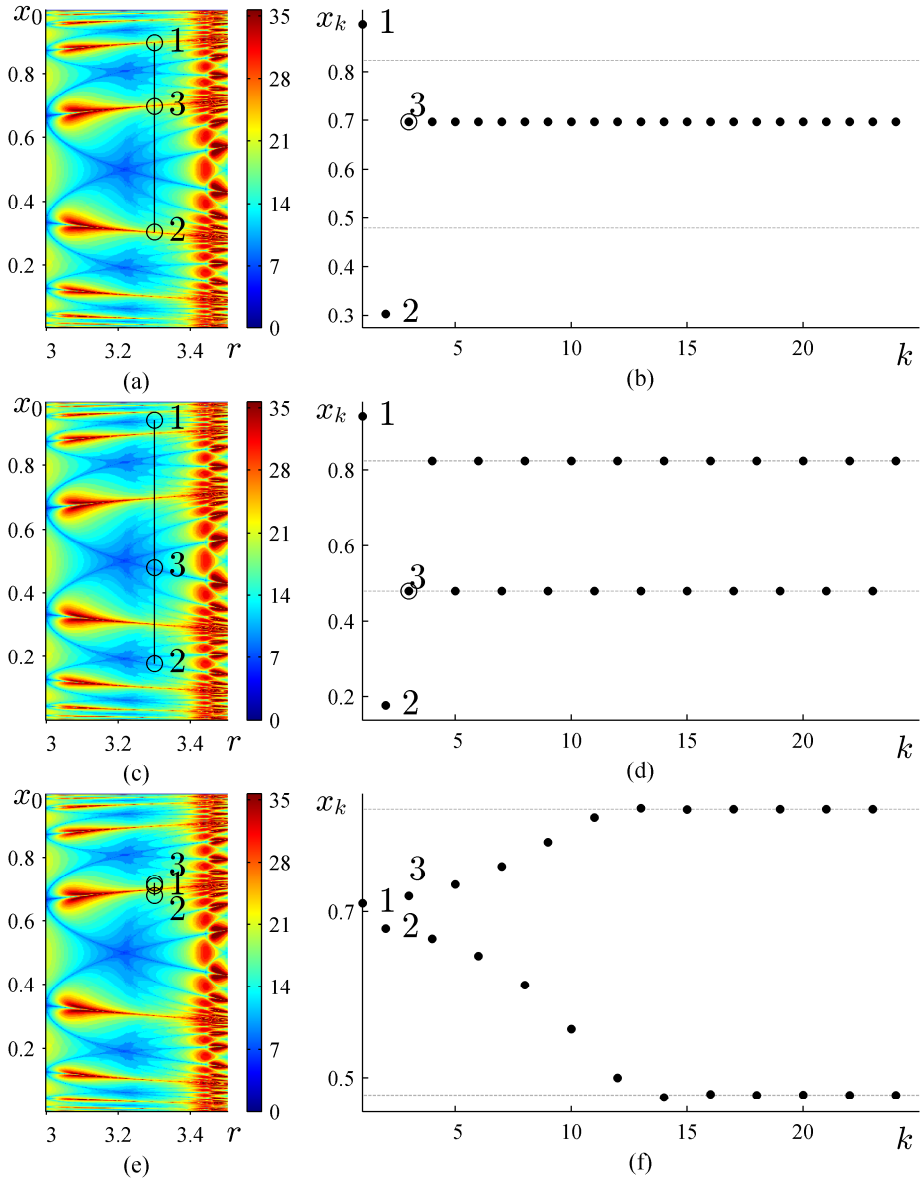

Fig. 16. Three different types of transient processes for the non-invertible Logistic map $x_{n+1} = rx_n\left(1-x_n\right)$. Parts (a) and (b) illustrate non-asymptotic convergence to the unstable period-1 repeller (the initial condition is located at the center of the second upper tulip in the pattern of *H*-ranks). Parts (c) and (d) illustrate non-asymptotic convergence to the stable period-2 attractor in two forward steps; parts (e) and (f) illustrate asymptotic convergence to the stable period-2 attractor. Parameter r is fixed at 3.3 in all computational experiments

All initial conditions can be classified into 3 distinct sets: the infinite uncountable set of initial conditions leading to the asymptotic convergence to the

period-2 attractor; the infinite countable set of initial conditions leading to the non-asymptotic convergence to the period-2 attractor and the infinite countable set of initial conditions leading to the non-asymptotic convergence to the unstable period-1 repeller. All three different types of convergence are illustrated in Fig. 16.

3.5. Pseudo Manifolds in the Space of System Parameters

3.5.1. A pseudo-stable Structure in a Completely Invertible Bouncer System

It was shown that a pseudo-stable structure of non-asymptotic convergence may exist in a completely invertible bouncing ball model. Visualization of the pattern of *H*-ranks helps to identify this structure. It appears that this structure is similar to the stable manifold of non-invertible nonlinear maps governing the non-asymptotic convergence to unstable periodic orbits. Yet this convergence to the unstable repeller of the bouncing ball problem is only temporary since non-asymptotic convergence cannot exist in completely invertible maps. This nonlinear effect is exploited for temporary stabilization of unstable periodic orbits in completely reversible nonlinear maps.

As mentioned before, Eq. (3) can be used as an approximation of the bouncing ball model – one may check (Joseph et al., 2012) for details. Nevertheless, here the bouncing ball model from (Luo and Guo, 2013) is taken, and Eq. (3) is derived. On the other hand, the investigated model (Eq. (3)) is a completely invertible discrete dynamical system. The initial conditions do specify the unique evolution of the system in the positive and in the negative direction (this is not true , for example, for the Logistic map considered in (Luo and Guo, 2013)). One of the main objectives of our approach is to propose an alternative approach based on the patterns of *H*-ranks. As mentioned previously, patterns of *H*-ranks had been used for noninvertible systems – now the efficiency of this approach for completely invertible systems is bound to be demonstrated.

Let us suppose that a ball of mass m is falling onto an oscillating table. The oscillations of the table follow the equation $m(t) = A(1+\sin(\omega t))$, $A \geq 0$; t here denotes time. Here, 1 is added in order to keep the amplitude always positive. Let us denote the moment of time the ball hits the table for the k-th time as t_k. Let $u(t_k)$ be the velocity of the ball right before the impact and $v(t_k)$ represent the velocity of the ball right after the impact.

If impacts are inelastic then $v(t_k) = -\alpha u(t_k)$; α is the coefficient of restitution. Let the velocities in respect of the table be noted with the bar as, for example, $\bar{v}(t_k)$. It follows that:

$$\bar{v}(t_k) = -\alpha \bar{u}(t_k), \tag{26}$$

$$\begin{cases} v(t_k) = \bar{v}(t_k) + m'(t_k); \\ u(t_k) = \bar{u}(t_k) + m'(t_k); \end{cases} \Rightarrow \begin{cases} \bar{v}(t_k) = v(t_k) - m'(t_k); \\ \bar{u}(t_k) = u(t_k) - m'(t_k). \end{cases} \tag{27}$$

Combining equations (26) and (27) results in:

$$v(t_k) - m'(t_k) = \bar{v}(t_k) = -\alpha \bar{u}(t_k) = -\alpha\left(u(t_k) - m'(t_k)\right). \tag{28}$$

$$v(t_k) - m'(t_k) = -\alpha\left(u(t_k) - m'(t_k)\right). \tag{29}$$

Thus the impact relation is derived:

$$v(t_k) = (1+\alpha)m'(t_k) - \alpha u(t_k), \tag{30}$$

as $m'(t) = A\omega\cos(\omega t + \theta_0)$, and the explicit impact map is:

$$v(t_{k+1}) = (1+\alpha)\omega A\cos(\omega t_{k+1} + \theta_0) - \alpha\left(v(t_k) - g\cdot(t_{k+1} - t_k)\right). \tag{31}$$

In order to find the value of θ_{k+1}, one needs to apply numerical algorithms. It is important to note that the velocity of the table is assumed to be not affected by the impacts.

Let us suppose that the ball travels a much further distance between the impacts compared to the distance covered by the oscillations of the table. Then $v(t_k) \approx \dfrac{g\cdot(t_{k+1} - t_k)}{2}$ and

$$t_{k+1} - t_k = \frac{2v(t_k)}{g}. \tag{32}$$

The velocity of the approaching ball reverses after the impact and by following the same idea it could be approximated as

$$u(t_{k+1}) \approx -v(t_k). \tag{33}$$

(30), (32) and (33) combine to the nonlinear map:

$$\begin{cases} t_{k+1} = t_k + \dfrac{2v(t_k)}{g}, \\ v(t_{k+1}) = \alpha v(t_k) + (1+\alpha)m'\left(t_k + \dfrac{2v(t_k)}{g}\right). \end{cases} \tag{34}$$

These equations can be non-dimensionalized by defining non-dimensional time $\varphi_k = \omega t_k$, non-dimensional velocity $v_k = 2\omega v(t_k)/g$, force amplitude

$\gamma = 2\omega^2(1+\alpha)\beta/g$ and $m'(t_k) = -\beta\omega\cos(\omega t_k + \theta_0)$. $m(t)$ is thus defined as mentioned before but with A:= $-\beta$. Then $\frac{\varphi_k}{\omega} = t_k$, $v(t_k) = \frac{g v_k}{2\omega}$, $1+\alpha = \frac{\gamma g}{2\omega^2\beta}$ and $m'(t_k) = -\beta\omega\cos\left(\frac{\varphi_k}{\omega} + \frac{v_k}{\omega}\right)$.

$$\begin{cases} \frac{\varphi_{k+1}}{\omega} = \frac{\varphi_k}{\omega} + \frac{v_k}{\omega}, \\ \frac{g}{2\omega} v_{k+1} = \frac{g}{2\omega}\alpha v_k + \frac{g}{2\omega}\frac{1}{\omega\beta}(-\beta\omega)\gamma\cos\left(\frac{\varphi_k}{\omega} + \frac{v_k}{\omega}\right). \end{cases} \tag{35}$$

After redefining $\varphi_k := \varphi_k/\omega$ and $v_k := v_k/\omega$, Eq. (35) evolves into

$$\begin{cases} \varphi_{k+1} = \varphi_k + v_k, \\ v_{k+1} = \alpha v_k - \gamma\cos(\varphi_k + v_k). \end{cases} \tag{36}$$

which is the model (Eq. (3)) used in this work. The presented techniques can be applied for any mapping in invertible dynamical systems.

Unstable periodic orbits in nonlinear maps can be identified by clocking the convergence processes. A pattern of *H*-ranks (which does help to clock the convergence) is a particularly useful tool for the visualization of these unstable orbits and their manifolds in non-invertible nonlinear maps (Landauskas and Ragulskis, 2012). However, non-asymptotic convergence to an unstable orbit cannot exist in a completely invertible map (this statement can be easily proven by the contradiction). Nevertheless, a "shadow" of a previously stable orbit (after a period doubling bifurcation) will still temporarily attract transient processes from some initial conditions in a completely invertible bouncing ball model. The question how to identify these "shadows" for an unstable orbit for a completely invertible map remains open.

In order to assess the convergence rate to stable periodic orbits of the bouncer model, computational tools based on *H*-ranks (Landauskas and Ragulskis, 2012) are used. The resulting patterns of *H*-ranks reveal interesting structures in the phase space of initial conditions. The fact that the "shadows" of unstable orbits can be interpreted in these patterns of *H*-ranks is not unexpected. The topological structure of these "shadows" is much more interesting as it appears to be strikingly similar to the stable manifold of a non-invertible one-dimensional Logistic map and thus suggests the existence of the non-asymptotic temporary convergence to the unstable repeller. The main objective of this chapter is to demonstrate the existence of this non-asymptotic convergence and its ability to stabilize unstable periodic orbits of discrete completely invertible dynamical systems during finite transient processes.

Period-1 fixed points of the bouncer model can be easily determined by substituting $x_{n+1} = x_n$ and $y_{n+1} = y_n$ into Eq. (3). There exist two different fixed points: $x^{(1)} = \pi/2 + 2\pi k$; $y^{(1)} = 0$ and $x^{(2)} = -\pi/2 + 2\pi k$; $y^{(2)} = 0$; $k \in \mathbb{Z}$.

The stability of the fixed points can be determined by evaluating the eigenvalues of the Jacobian matrix J_B:

$$J_B = \begin{bmatrix} \dfrac{\partial F_B(x_n, y_n)}{\partial x_n} & \dfrac{\partial F_B(x_n, y_n)}{\partial y_n} \\ \dfrac{\partial G_B(x_n, y_n)}{\partial x_n} & \dfrac{\partial G_B(x_n, y_n)}{\partial y_n} \end{bmatrix}. \tag{37}$$

$$\lambda_{1,2}\left(x^{(k)}, y^{(k)}\right) = \\ = \frac{1+\alpha-\beta\sin x^{(k)} \pm \sqrt{(1-\alpha)^2 - 2(1+\alpha)\beta\sin x^{(k)} + \beta^2 \sin^2 x^{(k)}}}{2}; \; k = 1,2. \tag{38}$$

Eq. (38) shows the eigenvalues of matrix J_B.

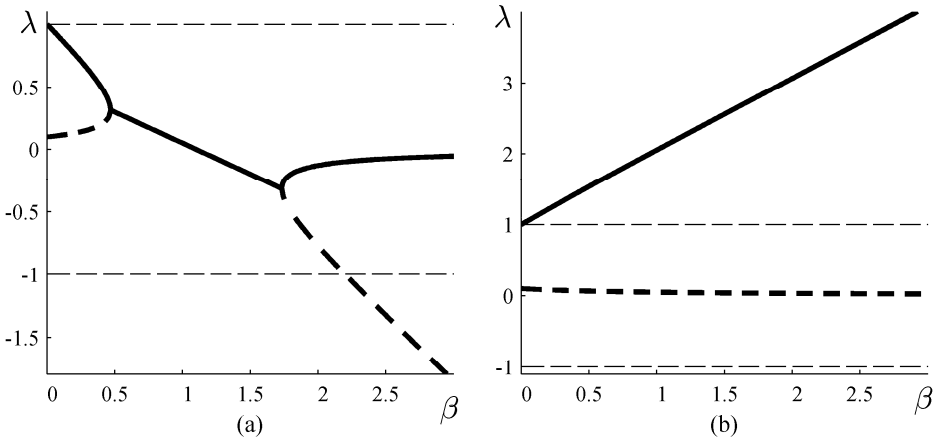

Fig. 17. The eigenvalues of the Jacobian matrix for $\left(x^{(1)}, y^{(1)}\right)$ (part (a)) and $\left(x^{(2)}, y^{(2)}\right)$ (part (b))

Now $\alpha = 0.1$ is fixed, and the variation of eigenvalues in respect to β is explored:

$$\lambda_{1,2}\left(x^{(1)}, y^{(1)}\right) = \frac{(1.1-\beta) \pm \sqrt{0.81 - 2.2\beta + \beta^2}}{2}, \\ \lambda_{1,2}\left(x^{(2)}, y^{(2)}\right) = \frac{(1.1+\beta) \pm \sqrt{0.81 + 2.2\beta + \beta^2}}{2}. \tag{39}$$

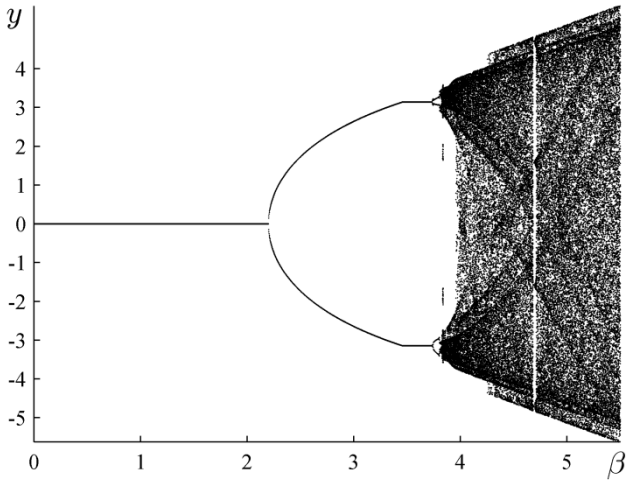

Fig. 18. The bifurcation diagram for the bouncer model; $\alpha = 0.1$

The values of $\lambda_{1,2}\left(x^{(k)}, y^{(k)}\right)$; $k = 1,2$ are plotted in Fig. 17. It can be seen that the fixed point $\left(x^{(1)}, y^{(1)}\right)$ is stable in the interval $0 < \beta < 2.200$ (both absolute values of its eigenvalues are lower than 1) and its stability is lost as β exceeds 2.200 (Fig. 17(a)). This fact can be observed in the bifurcation diagram (Fig. 18) where the first period doubling bifurcation occurs at $\beta = 2.200$.

3.5.2. Patterns of *H*-ranks for the Bouncer Model

Patterns of *H*-ranks for the bouncer model produced at different values of the parameter β are illustrated in Fig. 19. Every point in the phase space $(x_0; y_0)$ corresponds to a separate transient process starting from the initial conditions $(x_0; y_0)$. The color of a point is assigned in accordance to the *H*-rank of a transient process starting from this point. Yet *H*-ranks can be computed for scalar time series only (Ragulskis and Navickas, 2011). Therefore, $Hr\left(\sqrt{x_0^2 + y_0^2}, \sqrt{x_1^2 + y_1^2}, \sqrt{x_2^2 + y_2^2}, \ldots\right)$ is computed for a particular trajectory in the two-dimensional phase plane. Such an approach ensures the consistency of results and eliminates the possibility for the recovery of low *H*-ranks for such transient processes where one coordinate is frozen while the other performs wild oscillations.

The computation of the *H*-rank of a transient process for a predefined set of system parameters and initial conditions can be described by the following algorithm. Step 0: We set the maximum dimension $\overline{m}$ of the square Hankel matrix; we set $\varepsilon > 0$. Step 1: We compute the Hankel transform of the transient process up to $k = \overline{m}$ resulting in a sequence of determinants $\{d_k\}_{k=2}^{\overline{m}}$. Step 2: we find such

$2 \le s \le \overline{m}$ that $\{|d_k|\}_{k \ge s+1}^{\overline{m}} < \varepsilon$; we assign the *H*-rank of the sequence to s. If $|d_{\overline{m}}| \ge \varepsilon$ then we assume that the *H*-rank is greater than or equal to $\overline{m}$.

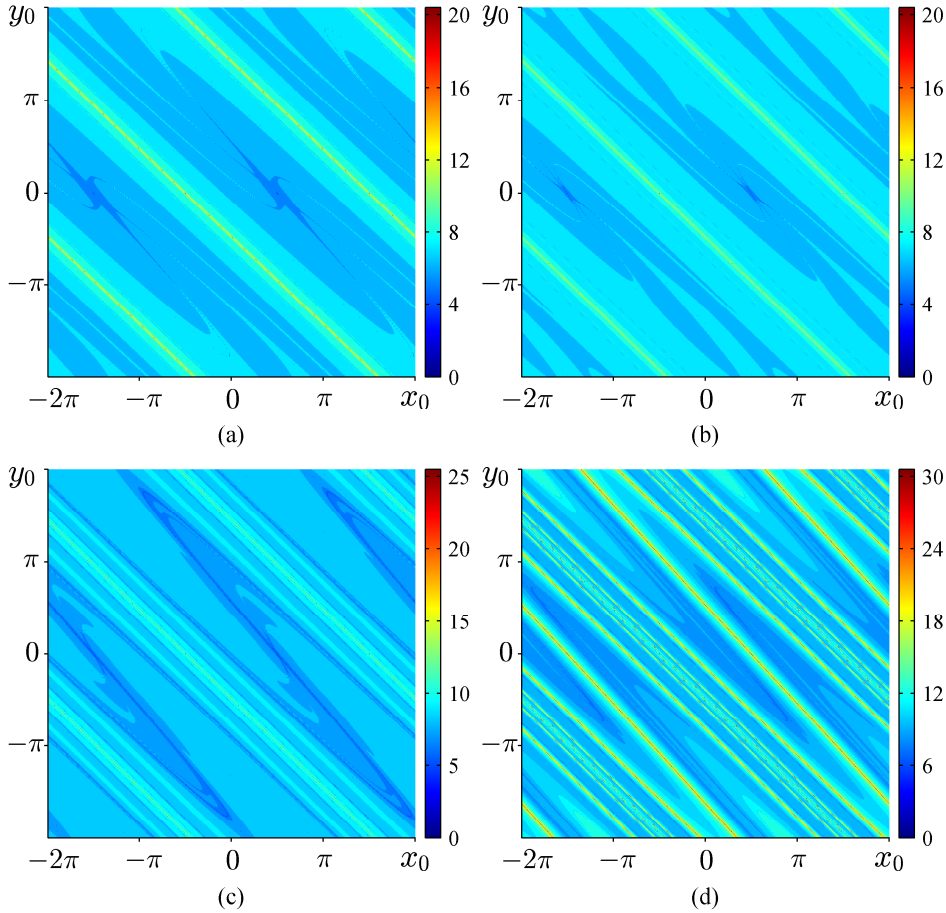

Fig. 19. Patterns of *H*-ranks computed for the bouncing ball model at a variety of values of β: (a): $\beta = 1$; (b): $\beta = 1.5$; (c): $\beta = 2$; (d): $\beta = 2.5$. Parameter α is fixed at 0.1; all the computations are performed in the region ($-2\pi \le x_0 \le 2\pi$ and $-2\pi \le y_0 \le 2\pi$)

Several characteristic features can be singled out in all patterns of *H*-ranks illustrated in Fig. 19. All the patterns of *H*-ranks are periodic in respect to x_0 due to the periodical structure of the model in respect of x. Stable period-1 attractors are clearly visible at $x_0 = \pi/2 + 2\pi k$; $y_0 = 0$; $k \in \mathbb{N}$ in Fig. 19(a), (b) and (c) (period-1 orbit is unstable in Fig. 19(d)). Also, it can be noted that the boundary lines separating periodic bands of patterns run through unstable period-1 fixed points $x_0 = -\pi/2 + 2\pi k$; $y_0 = 0$; $k \in \mathbb{N}$ in all the figures including Fig. 19(d).

Visualizing the pattern of *H*-ranks in one single periodic band would be advantageous. Straightforward shear mapping could be used for such visualization(s). Unfortunately, the slope of lines separating adjacent bands is

different for different β (Fig. 19). Numerical techniques for the approximation of the slope of separatrices (at the fixed level of $\alpha = 0.1$) were used:

$$y = -S(\beta)\cdot\left(x + \frac{\pi}{2} + 2\pi k\right); k \in \mathbb{N}. \tag{40}$$

Numerical values of parameter $S(\beta)$ are reconstructed from the results of numerical experiments: $S(1) = -0.9529$; $S(1.5) = -0.9615$; $S(2) = -0.9674$; $S(2.5) = -0.9735$; thus

$$S(\beta) = -0.01354\cdot\beta - 0.94013. \tag{41}$$

The least square linear regression yields the approximation depicted in Fig. 20 and is expressed as Eq. (41).

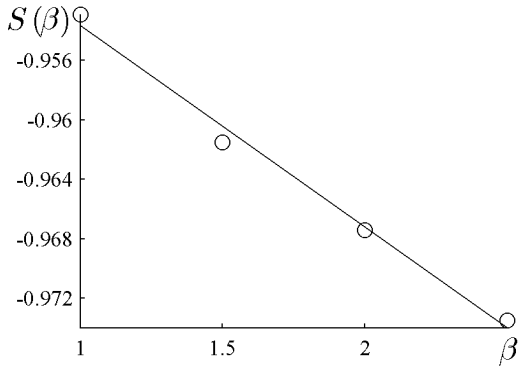

Fig. 20. Numerical reconstruction of the slope of separatrices $S(\beta)$. The circles denote numerically reconstructed values of the slope at $\beta = 1$; 1.5; 2 and 2.5; the solid line represents the least squares linear approximation of $S(\beta)$

Now, the plain shear mapping reads:

$$\begin{cases} x := x + \dfrac{y}{S(\beta)}; \\ y := y. \end{cases} \tag{42}$$

This mapping is used to visualize only one band between two adjacent separatrices; both separatrices are represented as vertical border lines on the left and the right side of the mapped image of *H*-ranks (Fig. 21). We should note that all the mapped coordinates at $y_0 = 0$ correspond to the original coordinate system as stable fixed points are located at $x_0 = \pi/2$; $y_0 = 0$ in Fig. 21(a), (b) and (c). Two period-2 fixed points are clearly visible in Fig. 21(d) (they are located in the centers of regions represented by the lowest *H*-rank). Let us note that period-2 fixed points are

separated by a new separatrix; this separatrix does cross the previously stable period-1 point at $x_0 = \pi/2$; $y_0 = 0$ (Fig. 21(d)).

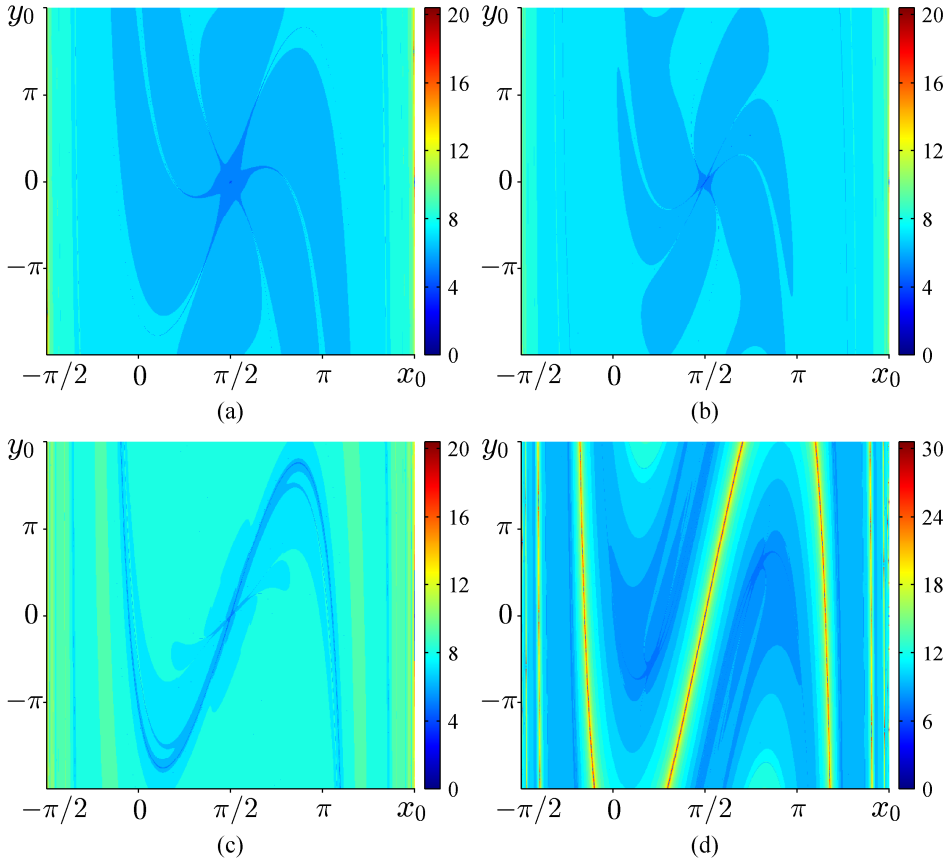

Fig. 21. Patterns of *H*-ranks in a periodic sheared band computed at a variety of values of β : (a): $\beta = 1$; (b): $\beta = 1.5$; (c): $\beta = 2$; (d): $\beta = 2.5$. Parameter α is fixed at 0.1

Snapshots of patterns of *H*-ranks in Fig. 19 and Fig. 21 are illustrated with four discrete values of parameter β . Continuous variation of parameter β would help to reveal the evolution of these patterns of *H*-ranks. In order to simplify the graphical data representation, every pattern in Fig. 21 is cut in the vertical and the horizontal direction through the point $(x_0 = \pi/2; y_0 = 0)$. The resulting graphs (as β varies continuously from 0 to 4) are shown in Fig. 22(b) (the vertical cut) and Fig. 22(a) (the horizontal cut).

The pattern of *H*-ranks in Fig. 22(b) reveals the period doubling bifurcation occurring at β = 2.200. The fixed point $(x_0 = \pi/2; y_0 = 0)$ becomes unstable after the first period doubling bifurcation; a characteristic supercritical pitchfork shape can be observed in Fig. 22(b) after the bifurcation point. Let us note that the outer pitchfork fingers do not represent the stable period-2 solution in Fig. 22(b) – the vertical cutting line does not intersect the stable period-2 attractor (Fig. 21(d)).

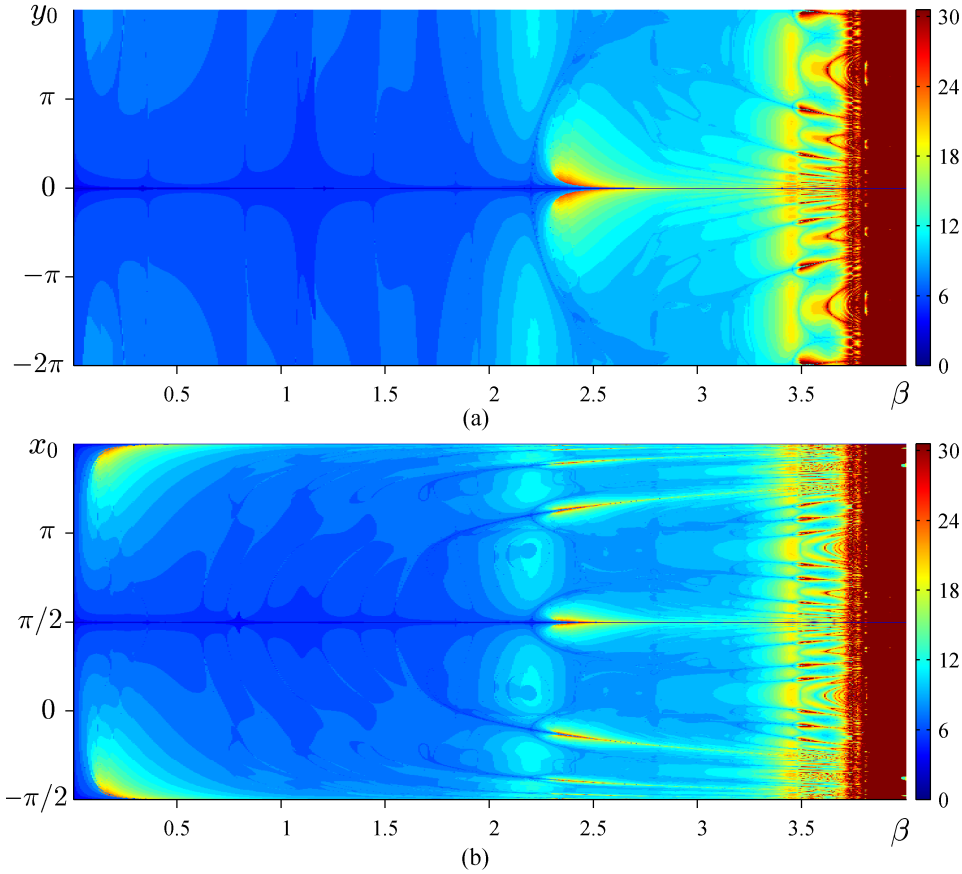

Fig. 22. The evolution of the pattern of *H*-ranks for the continuous variation of β in horizontal (a) and vertical (b) sections of sheared bands of *H*-ranks; parameter α is fixed at 0.1

The unstable finger of the pitchfork is surrounded by a region of high *H*-ranks after the period doubling bifurcation (Fig. 22(b)). This represents the transient behavior of solutions with initial conditions in the vicinity of the unstable period-1 fixed point. The system would be repelled to the stable period-2 attractor at $\beta = 2.5$. Yet this repelling process is slow if initial conditions are very close to the unstable period-1 fixed point (as the "shadow" of the previously stable attractor is still there (Hilborn, 2000)). The pattern of *H*-ranks surrounding the unstable period-1 repeller forms the shape of a tulip. Such an ornament represents the fact that the algebraic complexity of the transient process from the initial conditions near the repeller is high – the system starts slowly moving away from the unstable period-1 attractor and subsequently converges (after a rather long transient time) to the stable period-2 attractor.

3.6. Non-asymptotic Temporary Convergence

Let us consider the evolution of the pattern in *H*-ranks in vertical sections (Fig. 22(a)). The supercritical pitchfork of the period doubling bifurcation is also visible at β = 2.200. Yet we can observe a rather interesting structure of patterns in the region after the first period doubling bifurcation. Such structures in the pattern of *H*-ranks require further attention.

3.6.1. The Stable Manifold of the Bouncer Model

The *Dynamics* (Nusse and Yorke, 1998) software is employed here for the construction of the stable and unstable manifolds of the bouncer model. The stable and the unstable manifolds of the bouncer model are illustrated in Fig. 23 at $\alpha = 0.1$ and $\beta = 2.5$.

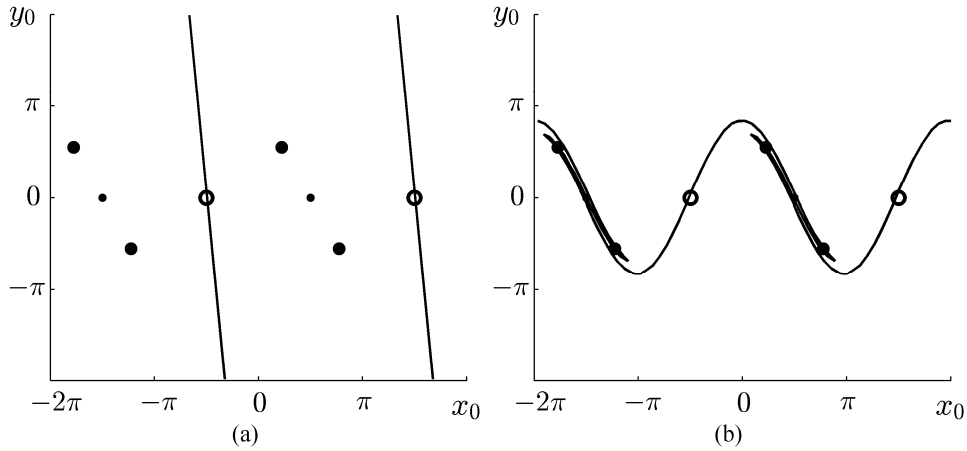

Fig. 23. The stable (a) and the unstable (b) manifolds of the bouncer model at $\alpha = 0.1$ and $\beta = 2.5$. The saddle points are shown as empty circles; the stable period-2 points are shown as black disks; "shadows" of previously stable period-1 points are shown as black dots and are located between each pair of black disks. The unstable manifold goes through all the equilibrium points (both stable and unstable)

3.6.2. The Pseudo-stable Structure of the Bouncer Model

Let us consider the pattern of *H*-ranks constructed for the continuous variation of β in horizontal sections (Fig. 22(b)). A vertical band of *H*-ranks around $\beta = 2.5$ is illustrated in Fig. 24(a). Let us denote the region of higher *H*-ranks wrapped around the central line $x_0 = \pi/2$ as the central tulip. Regions of higher *H*-ranks above and below the central line are denoted as the first upper and the first lower tulip accordingly (marker 2 is located near the first upper tulip in Fig. 24(a)). Analogously, tulips located further away from the central line are given higher numbers (marker 1 is located at the center of the second upper tulip in Fig. 24(a)).

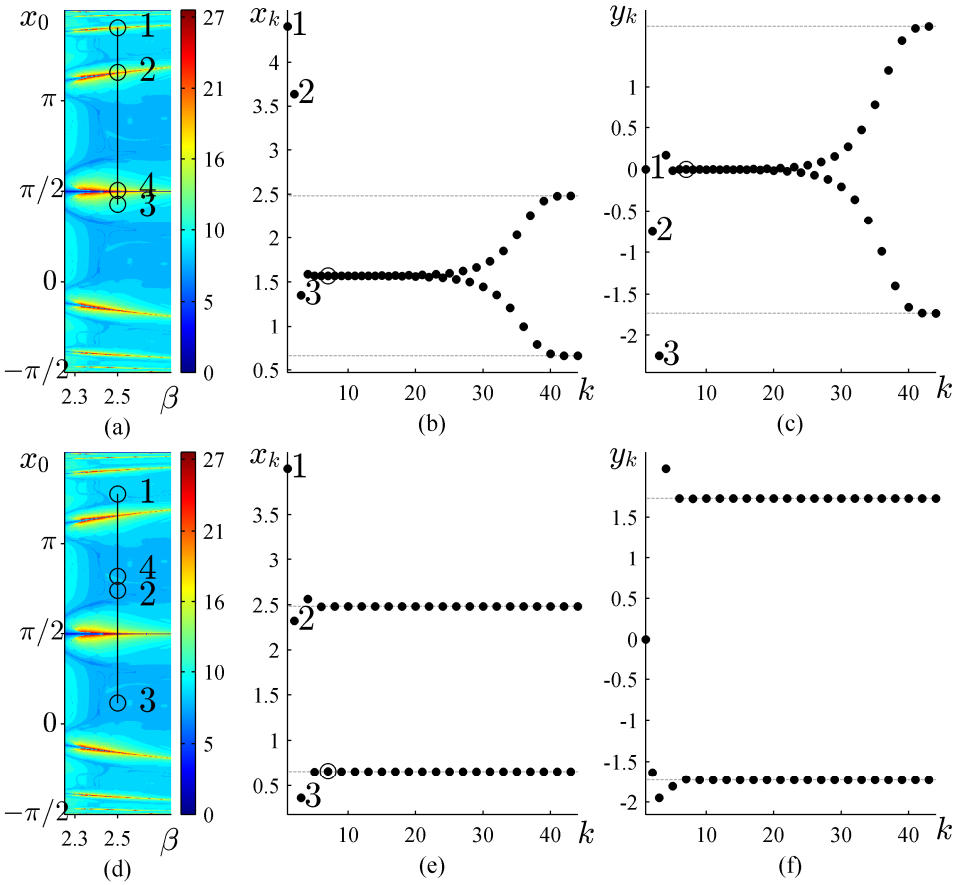

Fig. 24. The evolution of a transient process starting from the initial conditions coinciding with the center of the second upper tulip in the pattern of *H*-ranks. Part (a) shows a vertical band of the pattern of *H*-ranks in Fig. 3.4(b) around $\beta = 2.5$; part (b) illustrates the evolution of x_k; part (c) represents the evolution of y_k (k is the step number). Initial conditions are marked by symbol 1 in parts (a), (b) and (c). 4 consecutive steps are illustrated in part (a); 44 forward steps are illustrated in parts (b) and (c). Initial conditions located not in the center of a tulip result in fast convergence to the stable period-2 attractor (parts (d) and (f)). Parameter α is fixed at 0.1; β here is 0.25

It can be observed that the initial conditions corresponding to the centers of tulips result in transient processes approaching the unstable period-1 regime and consequently converging to the stable period-2 regime (Fig. 24). Initial conditions for the computation experiment illustrated in Fig. 24 (a) are as follows: $x_1 = 4.4082$; $y_1 = 0$. We should note that y_1 must be equal to zero because the horizontal section through the pattern of *H*-ranks in Fig. 22(b) is performed through the point $(x_0 = \pi/2; y_0 = 0)$. Four consecutive steps of the transient process are illustrated in Fig. 24(a) but only x-coordinates are shown here. For example, the coordinates of the second point are $x_2 = 3.6392$; $y_2 = -0.7489$. Therefore, the coincidence of the

second point with the center of the first upper tulip in Fig. 24(a) is completely accidental. The transient process starting from the center of the first upper tulip would be different from the process illustrated in Fig. 24 (though it would also approach the unstable period-1 regime and then converge to the stable period-2 regime).

The evolution of x_k and y_k is illustrated in Fig. 24(b) and (c). The transient process approaches the unstable period-1 fixed point $(x_0 = \pi/2; y_0 = 0)$ but never reaches it. Empty circles at $\mathrm{k} = 6$ in Fig. 24(b) and (c) denote the sixth iteration when the system is located at the closest to this fixed point:

$$\sqrt{(x_6 - \pi/2)^2 + y_6^2} = 6.8454 \cdot 10^{-8}. \tag{43}$$

As mentioned previously, such temporary convergence to a "shadow" of a previously stable fixed point is not a new phenomenon. However, the basin of attraction of this "shadow" is rather unexpected. A schematic diagram drawn on top of Fig. 22(a) illustrates the complexity of this region (Fig. 25).

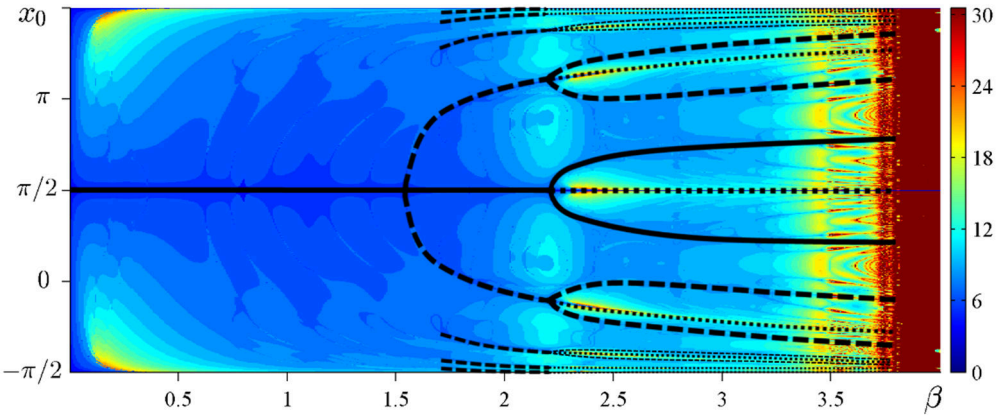

Fig. 25. Schematic diagram illustrating the skeleton-type structure of the pattern of *H*-ranks. Thick solid lines correspond to stable period-1 and period-2 regimes; the central thick dotted line corresponds to the unstable period-1 regime. All other thick dotted lines belong to the pseudo-stable structure of the unstable period-1 regime

The thick solid line in the region $0 < \beta < 2.200$ represents the stable period-1 attractor. The period doubling bifurcation occurs at $\beta = 2.200$; a stable period-2 regime exists at $2.200 < \beta < 3.736$ (the second period doubling bifurcation is not visualized). The "shadow" of the previously stable period-1 regime is shown as a thick dotted line at $x_0 = \pi/2$. Thick dashed lines before the first period doubling bifurcation correspond to such initial conditions which yield fast convergence to the stable period-1 regime. Analogously, thick dashed lines after the first period doubling bifurcation correspond to such initial conditions which yield fast convergence to the stable perdiod-2 orbit. Finally, thick dotted lines running through the centers of the top and the bottom tulips correspond to such initial conditions which yield fast (though temporary) convergence to the unstable period-1 regime.

It is well known that the bouncer model is a completely invertible discrete nonlinear map; a backward step can be expressed from Eq. (3):

$$\begin{cases} y_{n-1} = \dfrac{1}{\alpha}\left(y_n - \beta \cos x_n\right), \\ x_{n-1} = x_n - y_{n-1}. \end{cases} \tag{44}$$

In other words, a unique backward trajectory can be constructed for every initial condition of the bouncer model. That is contrary to discrete non-invertible maps where the process of the convergence to a stable attractor of a nonlinear discrete map can be classified into the asymptotic convergence and the non-asymptotic convergence. An infinite number of forward steps is required for the system to reach the stable attractor if it converges asymptotically. On the opposite, a finite number of forward steps is required to reach the stable attractor if the system converges non-asymptotically. Such different types of convergence to stable attractors of the non-invertible Logistic map are well known; some computational aspects for the identification of the type of the convergence are discussed in (Ragulskis and Navickas, 2011).

Yet the non-asymptotic convergence cannot exist in the bouncer model. This statement can be proven by contradiction. Let us denote the coordinates of the period- p orbit as $\left\{\left(\hat{x}_1;\hat{y}_1\right),\left(\hat{x}_2;\hat{y}_2\right),\ldots,\left(\hat{x}_p;\hat{y}_p\right)\right\}$. Let us assume that the set of initial conditions which yield the convergence to this periodic orbit in a finite number of forward iterations is not an empty set. Then there exists at least one point $\left(\hat{x}_0;\hat{y}_0\right)$ which does not belong to the periodic orbit and is mapped into a point $\left(\hat{x}_k;\hat{y}_k\right)$; $1 \le k \le p$ in one forward iteration (otherwise, non-asymptotic convergence would be not possible). But then the point $\left(\hat{x}_k;\hat{y}_k\right)$ is a branching point – it can be mapped either into the previous point of the orbit $\left(\hat{x}_{k-1};\hat{y}_{k-1}\right)$, or into $\left(\hat{x}_0;\hat{y}_0\right)$ in one backward iteration. It contradicts the fact that the bouncer model is a completely invertible discrete map.

However, the topological structures of patterns of *H*-ranks in Fig. 25 and 16 are strikingly similar. As discussed previously, non-asymptotic convergence to stable or unstable attractors is impossible for completely invertible maps. Therefore, initial conditions coinciding with the centers of tulips in the pattern of *H*-ranks for the bouncer model do not result in non-asymptotic convergence to the unstable period-1 attractor in Fig. 25 (contrary to the non-invertible Logistic map in Fig. 16). The system is just temporarily attracted to the vicinity of the unstable attractor (Fig. 25). Therefore the topological structure highlighted in Fig. 25 cannot be identified by *Dynamics*. Still, this structure *does* attract (although temporarily) the system to the unstable attractor. Moreover, this attraction reminds of non-asymptotic convergence as the system approaches the unstable attractor in a finite number of forward iterations. Thus the presently discussed topological structure is denoted as the pseudo-stable structure of the unstable orbit.

3.7. Controlling of Discrete Dynamical Systems

The main purpose of this section is to show the use of *H*-rank as a control tool for a discrete dynamical system. Firstly, the previously obtained pseudo-stable structure of the bouncer model will be employed for the stabilization of the unstable period-1 attractor. Next, the discrete iterative circle map will be used in order to illustrate the process of convergence to stationary states. It is shown here that the study of the convergence rate to a periodic orbit of a single circle map can produce patterns containing important information on the stability of periodic orbits of the circle map. This information could be useful whenever the manipulation or control of quasiperiodic nonlinear systems should be considered.

3.7.1. Temporary Stabilization of the Unstable Period-1 Attractor

The ability of the bouncer model to attract transient processes into the vicinity of the unstable attractor can be successfully exploited for the temporary stabilization of unstable orbits. A continuous feedback control loop is not necessary in such a case as one can exploit the small external pulse which could relocate the system onto a branch of the pseudo-stable structure.

Such a control strategy is illustrated in Fig. 26 and 27. A single impulse relocates the system onto a nearest point lying on the pseudo-stable structure. The system then converges non-asymptotically to the vicinity of the period-1 repeller and stays there for a considerable number of forward iterations.

The presented technique for the temporary stabilization of unstable orbits comprises the following steps:

1. We have to compute the pattern of *H*-ranks for the completely invertible discrete map.
2. We need to identify the structure of non-asymptotic pseudo-convergence to the unstable orbit in the pattern of *H*-ranks. Let us note that non-asymptotic convergence is not possible in a completely invertible discrete map; negative mapping cannot reveal this structure.
3. We use a control impulse so that to reset the system from its current point to the closest branch of this structure of non-asymptotic pseudo-convergence.
4. We then allow the system to converge (non-asymptotically) to the infinitesimal surrounding of the unstable orbit. Such a process of convergence is referred to as temporary convergence because the system cannot converge exactly to this unstable orbit – otherwise this system would not be invertible.
5. The unstable orbit is a repeller – finally the system will diverge from the infinitesimal surrounding of the unstable orbit. Yet the system will stay in the surrounding of this unstable orbit for a period of time before it converges (asymptotically) to a different stable attractor.

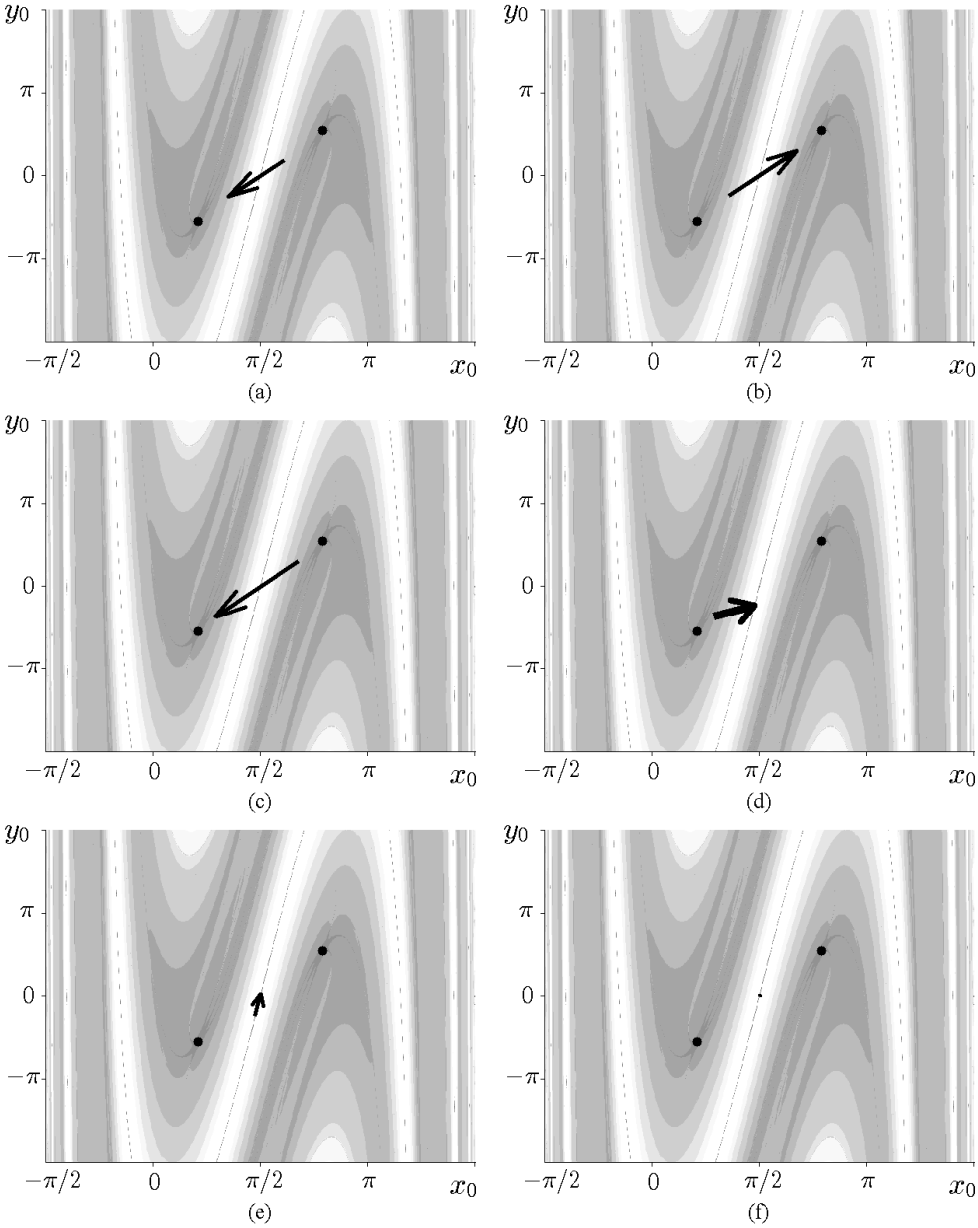

Fig. 26. The control strategy illustrated at $\alpha = 0.1$ and $\beta = 2.5$ (the grayscale pattern of H-ranks is only shown in the background for clarity). Thin black arrows illustrate the evolution of the system without any control applied – the system approaches the stable period-2 regime (illustrated by two thick black dots) in parts (a), (b) and (c). The thick arrow in part (d) illustrates the control impulse which relocates the system onto a point on the pseudo-stable structure. The system converges to the period-1 regime in a finite number of steps as shown in parts (e) and (f) (no control is further required)

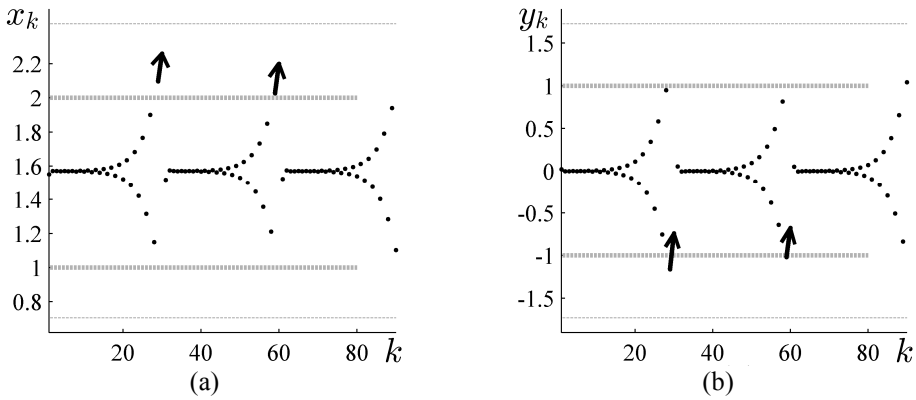

Fig. 27. Control strategy illustration for the bouncer model – the evolution of x_k and y_k is shown in parts (a) and (b). Thin dashed lines stand for the stable period-2 attractor; thick dashed lines show the acceptable range for the deflection from the unstable period-1 repeller. Thick arrows denote the relocation of the system by a control pulse

The whole process is called non-asymptotic temporary convergence to unstable orbits in the completely invertible discrete dynamical system.

3.7.2. The Sensitivity of the Temporary Stabilization Technique to External Noise

The experimental bouncing ball problem is an analog system – and computational simulation of this system does introduce numerical noise. The system is not only simulated. *H*-ranks of transient solutions are computed; however, this process introduces additional computational errors. That raises the question about the robustness of the proposed temporary stabilization technique to external noise. Such analysis is also important from the point of view of practical applicability of this technique to an experimental analog system which would be exposed to inevitable external noise.

Thus the perturbed system is defined by Eq. (45).

$$\begin{cases} x_{n+1} = x_n + y_n + b\xi_n; \\ y_{n+1} = \alpha y_n + \beta \cos(x_n + y_n); \end{cases} \tag{45}$$

where ξ_n is the Gaussian white noise with zero mean and a standard deviation equal to one; b is the noise intensity. The time interval between the collisions is perturbed; the velocity is perturbed automatically for every subsequent collision.

Three computational experiments are performed at $b = 0.0001$; $b = 0.001$ and $b = 0.01$ (Fig. 28); 50 experiments are repeated from the same initial conditions as used in Fig. 4.2 parts (b) and (c). Black dots in Fig. 28 correspond to unperturbed transient solutions (identical to ones illustrated in Fig. 27 parts (b) and (c)); gray dots correspond to 50 perturbed transients.

It is clear that small external noise does not damage the temporary stabilization of the unstable orbit – though the resulting time interval when the transient solution stays in the surrounding of the unstable period-1 repeller is on average shorter if

compared to the unperturbed case. By the way, there exist some particular transient solutions (Fig. 28) which stay longer in the surrounding of the repeller compared to the unperturbed system. That is an interesting phenomenon which could be explained by the fact that noise may change the stability of nonlinear systems (Hutt, 2008). In other words, proper manipulation with particular realizations of the Gaussian noise may enable the design of efficient control strategies of unstable orbits.

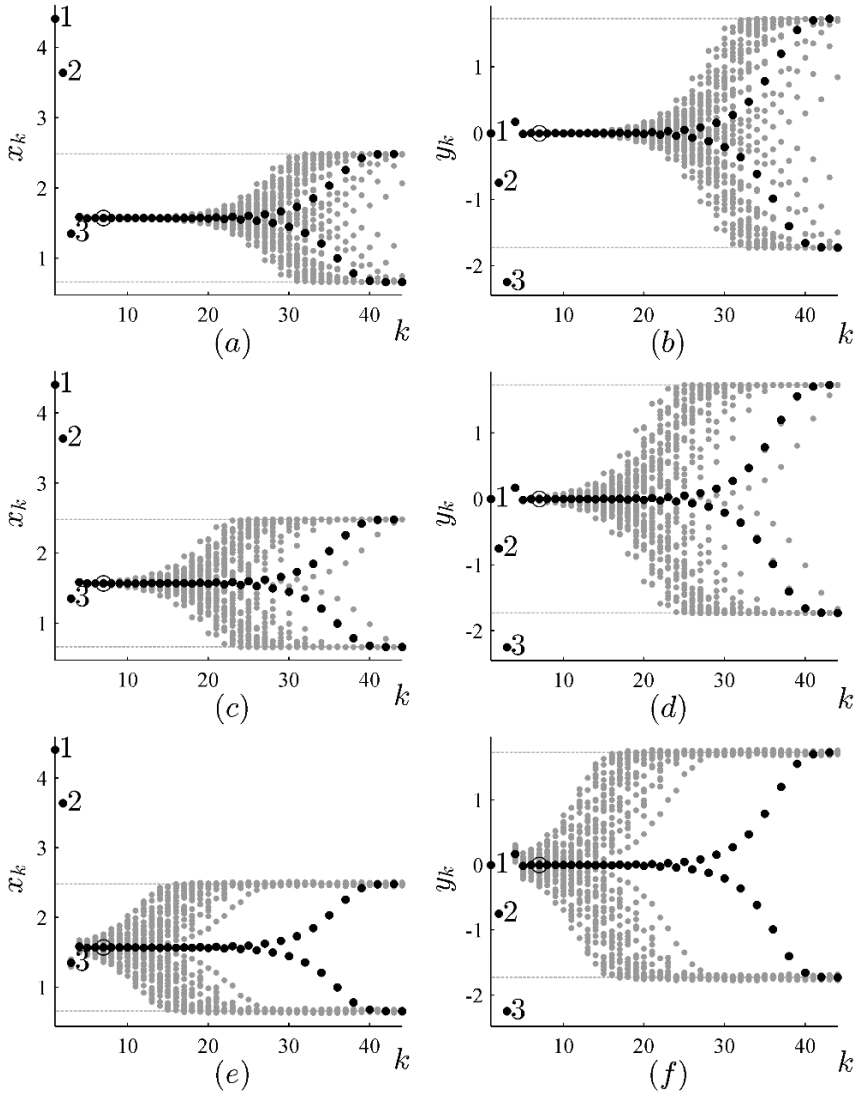

Fig. 28. The evolution of transient processes perturbed by the Gaussian noise at: $b = 0.0001$ (parts (a) and (b)); $b = 0.001$ (parts (c) and (d)); $b = 0.01$ (parts (e) and (f)). 50 perturbed transients are plotted as arrays of gray dots; the unperturbed transient is plotted as a sequence of black dots

3.7.3. Controlling of Period-2 Unstable Orbits in a Bouncer System

In this chapter, the unstable period-2 orbit of a bouncer system is explored. The use of techniques based on the patterns of *H*-ranks is employed in order to keep these orbits temporarily stable, i.e. to keep the iterative process bounded in a certain location. The results exhibit some important facts to be considered whenever controlling dynamical systems.

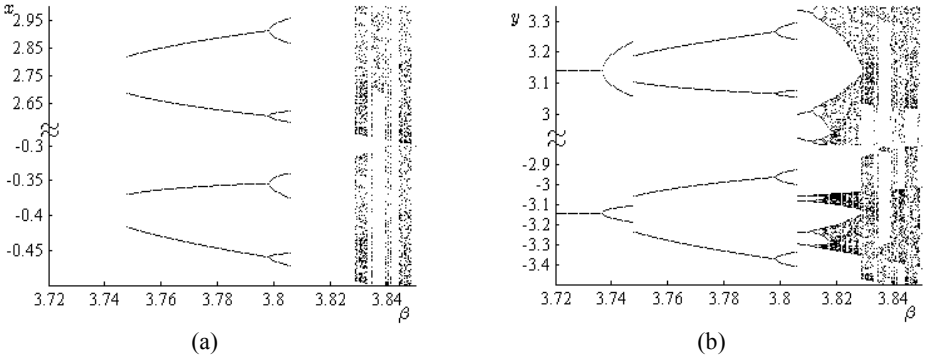

Fig. 29. Bifurcation diagrams of the bouncer system. (a) – diagram for variable *x*; (b) – diagram for variable *y*

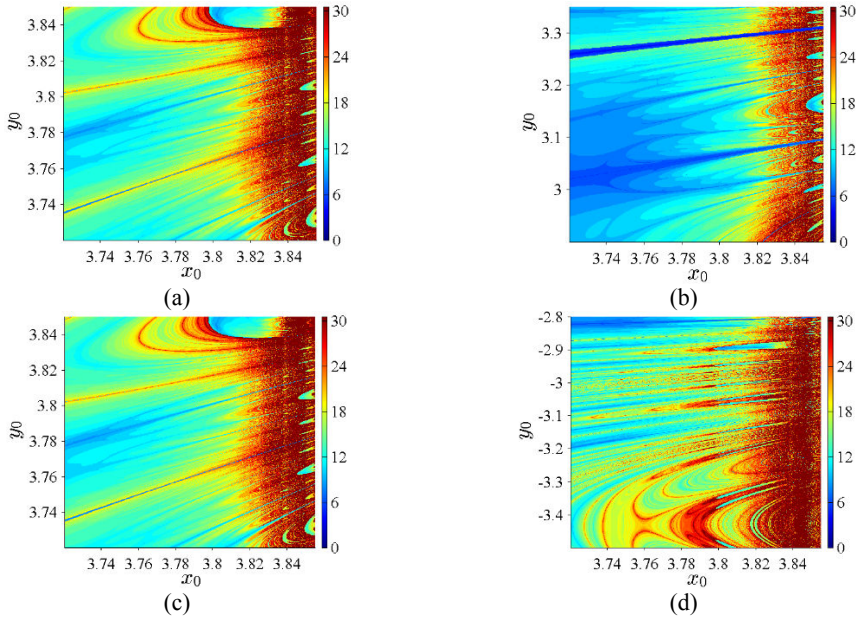

Fig. 30. Patterns of *H*-ranks. Part (a) corresponds to the upper part of the bifurcation diagram in Fig. 29(a); (b) corresponds to the upper part of Fig. 29(b); (c) corresponds to the lower part of Fig. 29(a); (d) corresponds to the lower part of Fig. 29(b)

However, whenever working with a dynamical system of more complex behavior, the proper interpretation of the pattern of *H*-ranks must be evaluated

beforehand. Thus this section takes it one step further by exploring a higher period orbit of the bouncer system.

It must be noted that the attractor of a bouncer system is not always unique. The bifurcation diagram in Fig. 29 is obtained by starting calculations from the same initial condition. At different β values, orbits may converge to different attractors; thus the bifurcation diagram results in getting sliced.

The focus here is on a non-feedback control method, the phase control method which has been hardly explored and applied to discrete dynamical systems. In the framework of this method, the phase of the applied perturbation is used in order to change the dynamical system behavior. Moreover, experimental implementation of this non-feedback method is relatively easy.

Let us consider a period-4 stable orbit for the bouncer system at $\beta = 3.79$. There exists a corresponding period-2 unstable orbit as the shadow of the previous stable period-2 orbit. The pattern of *H*-ranks in the vicinity of $\beta = 3.79$ is quite irregular (Fig. 30) and does not have any "tulip-shaped" areas the way the vicinity area of $\beta = 2.5$ does (Landauskas and Ragulskis, 2014). Thus here the unstable period-2 orbit is temporarily stabilized at $\beta = 3.79$ by employing *H*-rank based techniques used in (Landauskas and Ragulskis, 2014).

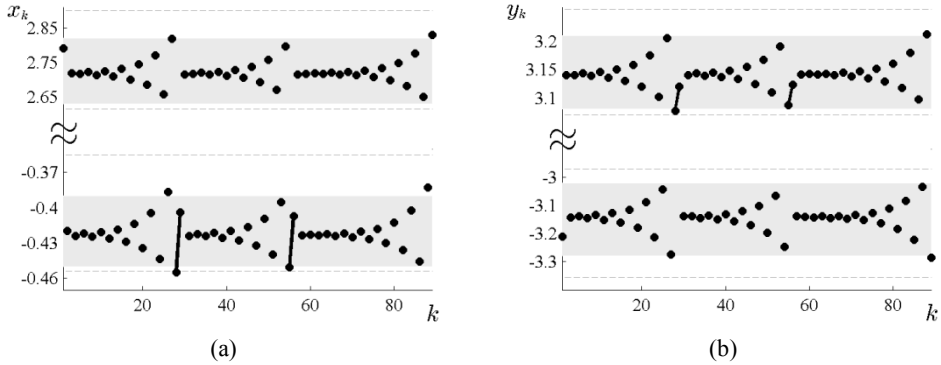

Fig. 31. The control of the unstable period-2 orbit for the bouncer model

The iterative process starts from $x_0 = 2.79$ and $y_0 = -3.21$. Fig. 31 depicts the evolution of the system. After 27 iterations, x_{27} resides outside the predefined strip of desirable values shown in gray color.

In Fig. 32 (a), the pattern of *H*-ranks in the vicinity of (x_{27}, y_{27}) is shown. The valley of low ranks results in the evolution of iterative process to be relatively near the period-2 unstable point in one iteration. In order to exert minimal control over the system, the nearest point in the valley is chosen. It is clearly seen in Fig. 31 that the orbit temporarily stays in the nearest vicinity of the period-2 unstable point. After another 26 iterations, control is applied again.

A very important observation should be made here. As mentioned before, the attractor of the bouncer model is not unique at $\beta = 3.79$. Fig. 32 (b) depicts the basin of attraction for the discussed system, and it could be seen that every initial

condition from part (a) evolves to the same attractor. Still, one can fall into the situation when a control impulse would tend to another attractor. The current example highlights the necessity to take into account the uniquiness of attractors as well while applying *H*-rank based control strategies.

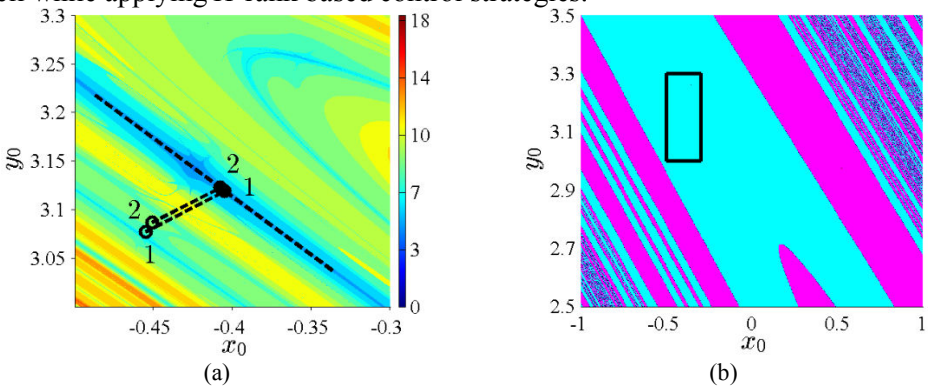

Fig. 32. The control of the unstable period-2 orbit; (a) – numerals represent the number of the control step, the empty circle is the point before the control impulse while the full circle represents the point after the control impulse; (b) – basins of attraction for the bouncer model; the rectangle shows the area relative to part (a)

We should note that while the biggest valley of low *H*-ranks in Fig. 32 (a) tends the orbit to the period-2 unstable point in one iteration, the other valeys do not behave like that. The orbit is placed closer to the stable period-4 regime then. This behavior is completely different from the one considered in the previous chapter while controlling the unstable period-1 attractor and was quite unexpected.

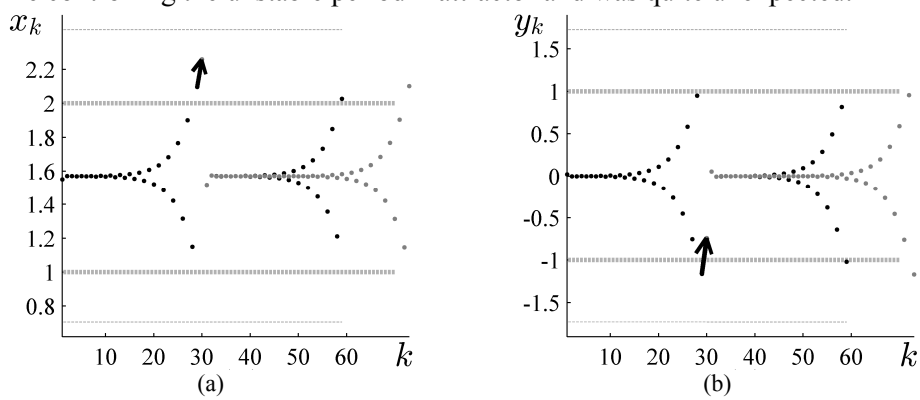

Fig. 33. The control strategy illustrated for the bouncer model – the evolution of x_k and y_k is shown in parts (a) and (b). Thin dashed lines stand for the stable period-2 attractor; thick dashed lines show the acceptable range for the deflection from the unstable period-1 repeller. Thick arrows denote the relocation of the system by a control pulse. Lighter dots mark the orbit obtained when utilizing the Gaussian noise at $b = 0.001$

The next section shows that the control quality is successfully improved by incorporating the Gaussian noise.

3.7.4. Improvement of the Control Strategy by Utilizing the Gaussian Noise

It was observed above that it is possible to efficiently control unstable orbits by properly utilizing the appropriate interpretation of the pattern of *H*-ranks and particular realizations of the Gaussian noise (Landauskas and Ragulskis, 2014). Additive noise itself can be considered as a control tool (Hutt, 2008). The presence of the noise enables us to adjust the control impulse thus boosting its efficiency. This also applies whenever the pattern of *H*-ranks is employed.

Fig. 33 illustrates the improvement of the control strategy presented in the previous section. As above, one needs to determine the right control impulse for the system by examining the corresponding pattern of *H*-ranks. Then, perturbation of the pair of new initial conditions (x^*, y^*) for the control pulse with noise (Eq. (45)) will lead to several possible scenarios of system dynamics. The orbit will be contained in the surroundings of the unstable period-1 repeller longer if one chooses the scenario with the lowest *H*-rank. This type of technique ensures the minimization of the algebraic complexity of the orbit.

It is important to employ the noise of low intensity as otherwise a different attractor may be reached. In a sense, the described technique is similar to evaluating a strip of patterns of *H*-ranks. The shape of the Gaussian distribution leads to most scenarios being condensed around (x^*, y^*).

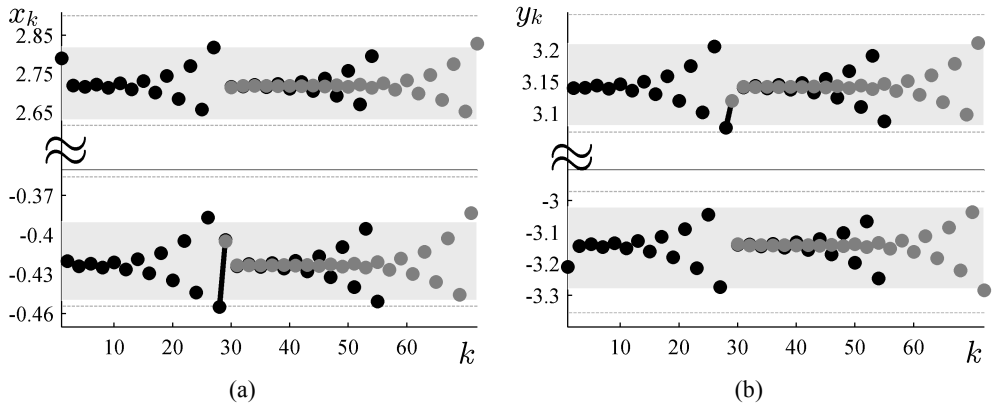

Fig. 34. Control of the unstable period-2 orbit for the bouncer model. Lighter dots are for the orbit obtained when utilizing the Gaussian noise with $b = 0.01$

The unstable period-2 orbit is also demonstrated to be more effectively controlled by perturbing initial conditions (x^*, y^*) for the control pulse with the Gaussian noise. Numerical experiments showed that, although being of a higher order, the fixed point is stabilized more efficiently by utilizing less deviated Gaussian noise.

3.7.5. *H*-pseudoranks as a Tool for Controlling the Circle Map

Here, the *H*-rank will be used as a computational tool for the reconstruction of Arnold tongues. *H*-ranks are computed in the region $0 \le \Omega \le 1$ and $0 \le K \le \pi$. For every pair of Ω and K, the iterative process is started, $k = 4000$ forward iterations

are omitted (all transients cease down during that period of time), the sequence $\left(\theta_{j+k}; j = 0,1,\ldots\right)$ is constructed, and the *H*-rank of that sequence is computed. As shown in (Ragulskis and Navickas, 2011), the *H*-rank of a chaotic sequence does not exist (it tends to infinity then). Therefore, the upper limit for the *H*-rank $\overline{m} = 15$ is set. If the sequence of determinants does not vanish until $m = 15$, the process is terminated assuming that $Hr\left(p_{j+k}; j = 0,1,\ldots\right) = \overline{m}$. The obtained results are shown in Fig. 35(a). The zones where the phase locking occurs are clearly separated by red insets; the produced picture reveals the well-known shape of Arnold tongues in the circle map (Schilder and Peckham, 2007).

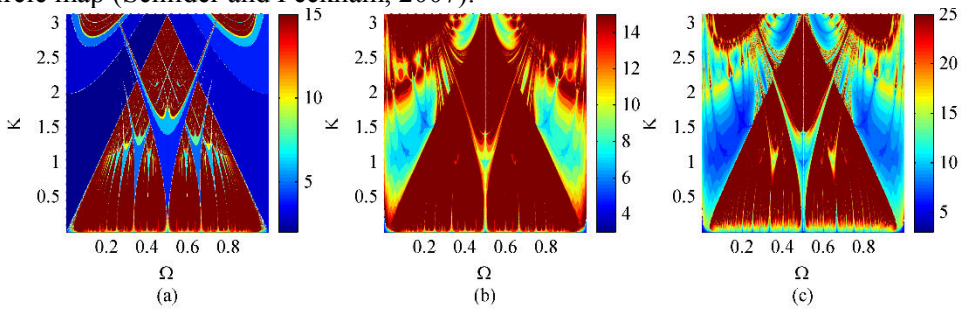

Fig. 35. Pseudoranks of the circle map. Part (a) was constructed by omitting transient processes whereas the initial phase was set at $\theta_0 = 0.5$; parts (b) and (c) were constructed without omitting transient processes

The computational experiment is repeated but this time without omitting transient processes ($k = 0$). The initial condition θ_0 is set at 0.5; the results show that the *H*-rank of the process involving transient processes is higher if compared to the *H*-rank of the same process but with transient processes getting omitted (Fig. 35(b)). The higher value of the upper bound ($\overline{m} = 25$) helps to visualize complex transient processes in the regions where phase locking occurs (Fig. 35(c)). The interesting pattern in the blue-colored zones (corresponding to phase-locked regions in the $\Omega - K$ plane) is rather unexpected and requires additional attention.

It is natural to expect that the initial condition $\theta_0 = \theta^* = 0.135$ should yield a minimal rank at $\Omega = 0.15$ and $K = 0.4\pi$. The computational experiment is repeated by constructing a map of pseudoranks when the initial phase is set at $\theta_0 = 0.135$ which also proved to be a clear illustration of the complex dynamic behavior of the circle map. The convergence process to the phase-locked behavior (Arnold tongues) is far from trivial, and one *does* need to pay careful attention to a number of circumstances whenever the generation or control of phase-locked regimes in discrete iterative maps is considered.

Even though theoretically one needs to find such a matrix dimension that the determinant of the Hankel matrix is equal to zero, in practice it suffices to compute determinants up to specific precision, like the *machine epsilon*. Thus the

computation of determinants is continued until $\left|H^{(m)}\right| < \varepsilon$. In this respect, the computations reveal not the rank but the pseudorank of a sequence instead. An analogy could be drawn with the pseudospectrum of a linear operator (Trefethen, 1997).

The selection of a particular value of ε requires additional attention. The structure of Arnold tongues in the circle map is well-known. Thus Fig. 35(a) is selected, parameter K ($K = 0.4\pi$) is fixed and a cut through the map of pseudoranks by varying parameter Ω is made. Moreover, the computation of pseudoranks for a variety of initial conditions ($0 \le \theta_0 \le 1$) for different ε is performed. The value $\varepsilon = 10^{-30}$ is fixed and used for the computation of pseudoranks (all previous figures of pseudoranks were constructed by using this particular value of ε).

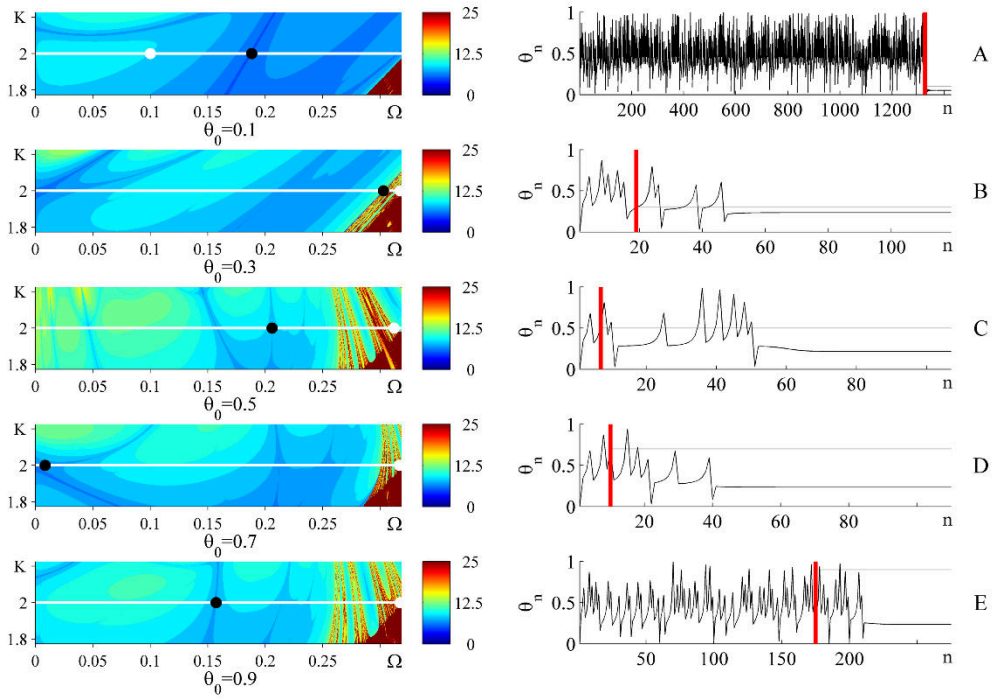

Fig. 36. The adjusting of Ω^*. The black dots show the lowest ranks at $K = 2$, the white dots show the highest ranks at the same K

Let us consider that the system is in the regime where $\Omega = 0.35$, $K = 2$ and $\theta_0 = 0.135$. Then we say that the map converges to a particular fixed point. While being able to control parameter Ω one might want the system to fall into the stable period-1 regime and the transient process to be as long as possible.

Now from the condition $f(\theta_{n+1}) = f(\theta_n)$ it follows that $\Omega = \dfrac{K}{2\pi} sin(2\pi\theta_n)$. This holds true if $\Omega^* \le K/2\pi$. Otherwise the map does not converge to a stable

point. In this particular case the stable period-1 regime exists if $\Omega^* \leq 1/\pi$. By replacing the particular Ω with $\Omega^* = \frac{K}{2\pi} sin(2\pi\theta_n)$ the system suddenly falls in the stable mode. But in this case the duration of the transient process is equal to zero. Thus another $\Omega^* \leq 0.1$ must be considered, and this is the value which represents the highest rank of the sequence in the phase plane $\Omega - K$.

The conducted numerical experiments enable us to take control of the particular system defined by a circle map. Fig. 36 illustrates the algorithm of establishing the control function $g(\theta_0)$. The value of this function is the value of Ω^* one needs to set Ω at step n (or moment n) in order to drive the system to the period-1 stable regime. The argument of the function is equal to θ_n. Thus θ_m , $m > n + n_0$ becomes equal after a transient process – as that was the objective. Here n_0 is the number of steps this transient process takes. Due to the above mentioned technique, the duration of the transient process is maximized.

Let us consider a situation when the circle map is operating in a chaotic regime and one needs to bring it to the phase-locked regime (we assume that there is a possibility to control one or both parameters of the circle map). One may jump from the chaotic region into the phase-locked region on the parameter plane of the circle map in one forward iteration. Yet the convergence to the actual phase-locked regime depends on the instantaneous phase of the system right after the jump. One can determine the phase of the circle map immediately before the jump and adjust the parameters of the map in such a way that the system is placed onto the manifold of non-asymptotic convergence immediately after the adjustment of the parameters has been performed. Such a control method would ensure that the system will start operating in the phase-locked mode immediately after the correction of the system's parameters. Otherwise (if the distribution of manifolds on Arnold tongues is unknown), a long transient process could be required until the system starts operating in the phase-locked mode.

It must be noted that changing Ω in a particular circle map affects its behavior. That is, the fixed point changes. Or, in other words: the system is modified to slowly converge to another stable state. It is reasonable to perform the above mentioned correction of Ω after detecting that the system has become stationary. Otherwise, the correction might result in a shorter transient process than that of the original system. Furthermore, such a control technique enables us to keep the system running. If one finds the $\Omega^* \geq K/(2\pi)$ with the highest rank, the system might be revived once and for all because there might be no fixed point.

3.8. Controlling of Continuous Dynamical Systems

3.8.1. Clocking Convergence to a Limit Cycle

A periodically driven pendulum will be used to explore the applicability of the *H*-rank for the investigation of non-asymptotic convergence to the dynamical

attractor. The model was previously defined with Eq. (2). Values $f = 2.048$ and $\omega = 2/3$ will be fixed in all further computations.

We note that the bifurcation diagram in Fig. 2 is constructed from steady-state solutions (a considerable number of initial iterates are omitted in order to exclude the transient behavior of the system). To the contrary, the investigation of the convergence processes requires data on the transient behavior of the system. Therefore the computation of *H*-ranks for solutions of the periodically driven pendulum must be performed without omitting transient processes.

Let us consider a discrete partial solution computed by using a constant-step time-forward marching integrator:

$$x(t_0 + kh) = x_k;\ \frac{dx}{dt}(t_0 + kh) = \dot{x}_k;\ \frac{d^2x}{dt^2}(t_0 + kh) = \ddot{x}_k; \tag{46}$$

where $k = 0,1,2,\ldots$ and h is the integration step in time. Straightforward computation of the *H*-rank for the partial solution could be performed in several alternative ways: $Hr(x_0, x_1, x_2, \ldots)$; $Hr(\dot{x}_0, \dot{x}_1, \dot{x}_2, \ldots)$; $Hr(\ddot{x}_0, \ddot{x}_1, \ddot{x}_2, \ldots)$ or

$$Hr\left(\sqrt{x_0^2 + \dot{x}_0^2 + \ddot{x}_0^2}, \sqrt{x_1^2 + \dot{x}_1^2 + \ddot{x}_1^2}, \sqrt{x_2^2 + \dot{x}_2^2 + \ddot{x}_2^2}, \ldots\right). \tag{47}$$

Unfortunately, neither of these strategies yields interpretable results – the step of integration is too small to build a representative sequence from a short time series.

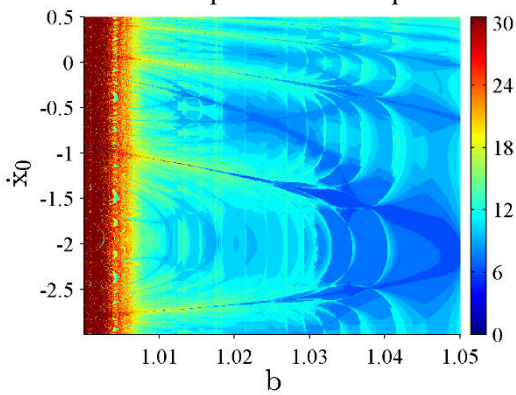

Fig. 37. The pattern of *H*-ranks for the system $\ddot{x} + b\dot{x} + \sin x = 2.048\cos(2t/3)$; $x(0) = 0$ is fixed for all initial conditions. *H*-ranks are computed for sequences of Poincaré section points

The alternative strategy for building a representative pattern of *H*-ranks could be based on Poincaré sections when the *H*-rank is computed from the sequence of consecutive coordinates of points in the section plane (Fig. 37). Such computation of *H*-ranks for partial solutions reveals the intrinsic structure of intertwined manifolds but the image is distorted due to inaccuracies in the determination of the point of intersection between the trajectory and the section plane (Fig. 37).

Strobing at the drive frequency helps to overcome the above mentioned drawbacks whereas the reproduced pattern of *H*-ranks reveals a clear structure of intertwined manifolds (Fig. 38). It must be noted that the whole number of time steps must fit into the stroboscopic period – otherwise the resulting pattern would be unclear due to reasons similar to the ones described above. Moreover, the numerical integrator must employ a constant step time forward marching technique since variable time step methods cannot be used for the construction of patterns of *H*-ranks. Newmark constant step constant average acceleration method (Newmark, 1959) is thus employed; the time step is set at $h = 2\pi/(500\omega)$. Thus every 500th step is used to construct the sequence and to calculate the *H*-rank as described with Eq. (2).

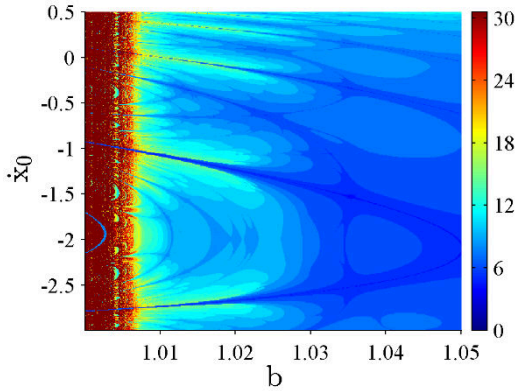

Fig. 38. The pattern of *H*-ranks for system $\ddot{x} + b\dot{x} + \sin x = 2.048\cos(2t/3)$; $x(0) = 0$ is fixed for all the initial conditions. *H*-ranks are computed for the sequences of the stroboscopic representation of the transient processes

The fact that the rate of convergence to the limit cycle type attractor (at fixed parameters of the system) depends on the initial conditions is not unexpected. The fact that the convergence to the stable limit cycle can be faster from a point located further away than from another point located closer to the limit cycle does not astonish us, either. Yet the pattern of *H*-ranks reveals a clear structure of intertwined manifolds (let us compare Fig. 38 to Fig. 10(c) and to the pattern of *H*-ranks constructed for the Logistic map in (Ragulskis and Navickas, 2011)). The deepest trench (i.e. the lowest *H*-rank in Fig. 38) corresponds to the initial condition near the trajectory of the limit cycle. However, a number of "shadow" trenches are visible at other values of $\dot{x}_0$ in Fig. 38. We should note that the pattern of *H*-ranks is computed for the strobed data. Nevertheless, Fig. 38 still suggests that there exists a manifold of nonasymptotic convergence to the stable limit cycle in the stroboscopic representation of the transient data.

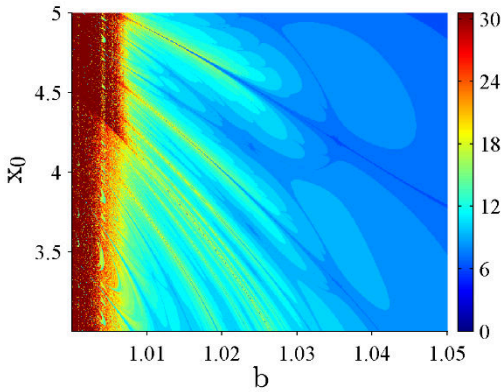

Fig. 39. The pattern of *H*-ranks for the system $\ddot{x}+b\dot{x}+\sin x=2.048\cos(2t/3)$; $\dot{x}(0)=0$ is fixed for all the initial conditions. *H*-ranks are computed for the sequences of the stroboscopic representation of the transient processes

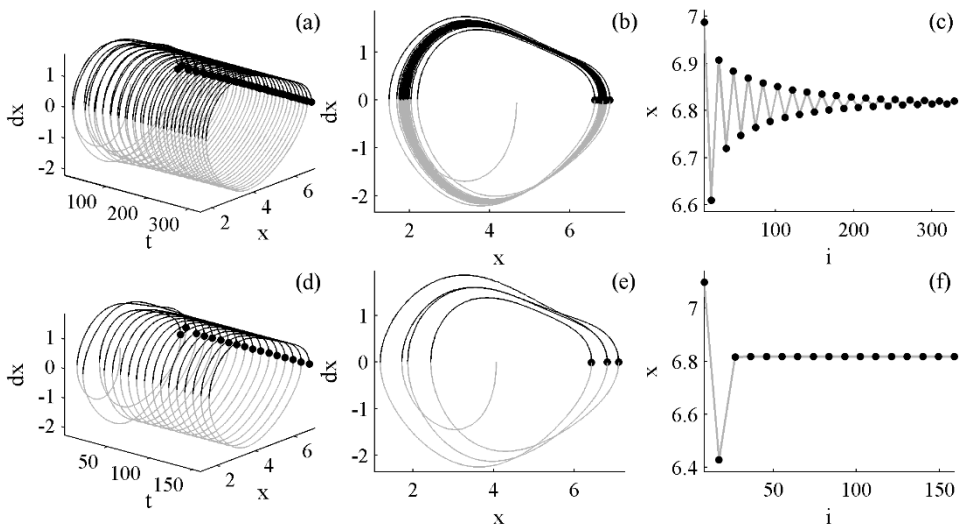

Fig. 40. Asymptotic versus non-asymptotic convergence to the stable limit cycle in the stroboscopic representation of the transient data of the system $\ddot{x}+b\dot{x}+\sin x=2.048\cos(2t/3)$. Part (a) shows the evolution of the partial solution in 3D; (b) illustrates the projection of the transient process on the phase plane $x-\dot{x}$; (c) shows the consecutive sequence of strobing points starting from $t_0=0$; $x_0=4.66$ and $\dot{x}_0=0$. Parts (d), (e) and (f) illustrate the transient process starting from $t_0=0$; $x_0=4.059$; $\dot{x}_0=0$

The interpretation of the pattern of *H*-ranks in Fig. 38 and Fig. 39 can be illustrated by the following computational example. Let us consider a period-1 limit cycle at b = 1.04. The initial conditions $t_0=0$; $x_0=371\pi/250\approx 4.660$ and $\dot{x}_0=0$ correspond to a point in the light blue region in the pattern of *H*-ranks in Fig. 39. Transient processes are illustrated in Fig. 40 (black dots denote strobing moments);

part (a) shows the evolution of the process in the 3D coordinate system; part (b) illustrates the projection of the transient process on the plane $x-\dot{x}$; part (c) shows a consecutive sequence of strobing points (adjacent strobing points are interconnected for clarity only). It is clear that the transient trajectory converges asymptotically to the stable period-1 limit cycle.

The situation becomes different at $t_0 = 0$; $x_0 = 323\pi/250 \approx 4.059$ and $\dot{x}_0 = 0$ (Fig. 40). These initial conditions correspond to the point in the deepest trench of the pattern of *H*-ranks in Fig. 39. The transient process comprises three distinct loops; the system is locked into the period-1 attractor afterwards. Such transient dynamics can be explained by the nonasymptotic convergence to the period-1 limit cycle in the stroboscopic representation of the transient data.

3.8.2. Control of Transient Processes

The existence of such special transient processes which yield fast nonasymptotic transitions to limit cycles enables the construction of effective control methods when the transition time must be minimized. It was shown in (Ragulskis and Navickas, 2011) that the entire set of initial conditions can be classified into the infinite uncountable set of initial conditions yielding asymptotic convergence to the stable fixed point and the infinite countable set of initial conditions yielding nonasymptotic convergence to the same fixed point. Thus a random selection of initial conditions most probably leads the transient process to asymptotic convergence to the stable fixed point. Prior knowledge about the shape and the structure of the manifold of nonasymptotic convergence (as illustrated for the circle map, for example) is required in order to select the corresponding initial conditions.

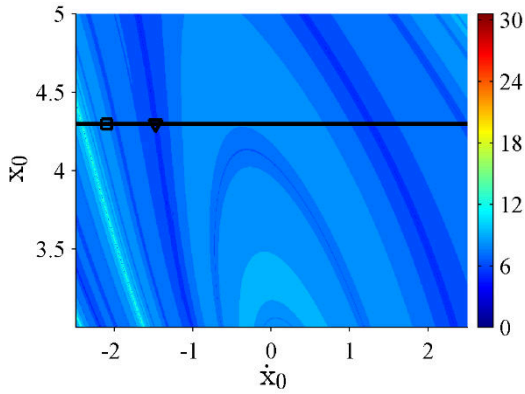

Fig. 41. The pattern of *H*-ranks for the system $\ddot{x} + b\dot{x} + \sin x = 2.048\cos(2t/3)$ on the phase plane $x_0 - \dot{x}_0$. The square marker denotes the position of the system before the impulse; the triangle marker shows the position of the system after the impulse

At this point it must be observed that the convergence to a stable limit cycle (in the strobed data) is considered now instead of the convergence to a fixed point. Let us consider a situation in which the evolution of the system starts from the initial conditions resulting in asymptotic convergence to a period-1 limit cycle ($b = 1.04$;

all other parameters of the system are fixed throughout the computational experiment). Fig. 38 and Fig. 39 represent patterns of *H*-ranks when one initial condition (x_0 or $\dot{x}_0$) is set at zero at $t_0 = 0$. These patterns would be different for other values of t_0 but they are exactly the same for $t_0 = 2\pi k/\omega$; $k \in \mathbb{Z}$ due to the periodicity of the forcing term. Thus patterns of *H*-ranks constructed for $t_0 = 0$ could be used for the control of transient processes at any time moment $t = 2\pi k/\omega$; $k \in \mathbb{Z}$. Unfortunately, it is unrealistic to expect that one of the system variables ($x(t)$ or $\dot{x}(t)$) will become equal to zero at one of the strobing moments. A plot of *H*-ranks in respect of initial conditions x_0 or $\dot{x}_0$ (Fig. 41) helps to resolve the above mentioned limitation.

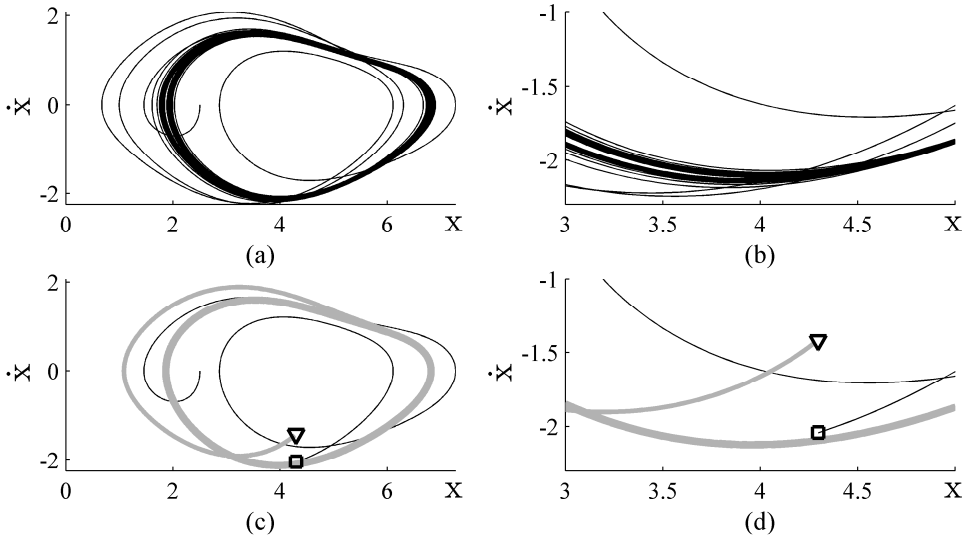

Fig. 42. The control of the transient process based on a single external impulse. The evolution of $\ddot{x} + b\dot{x} + \sin x = 2.048\cos(2t/3)$ starting from $x_0 = 2.5$ and $\dot{x}_0 = 0$ is shown in part (a). Part (b) shows the zoomed region of (a). The square marker denotes the position of the system before the impulse; the triangle marker shows the position of the system after the impulse in part (c) (part (d) shows the zoomed region of (c)); the trajectory after the impulse is shown in gray

Let us assume that the transient process starts from initial conditions $x_0 = 2.5$; $\dot{x}_0 = 0$ (Fig. 42(a)); the system converges asymptotically to the period-1 limit cycle; a zoomed region in Fig. 42(b) illustrates the process of asymptotic convergence to the stable attractor. Fig. 42(c) demonstrates the control technique based on a single control impulse (all system parameters including the initial conditions are kept unchanged). The initial transient process (the black solid line in Fig. 42(c)) is continued for two stroboscopic cycles. The system is then perturbed by an instantaneous impulse which changes the velocity whereas the displacement remains unchanged. The position of the system before the impulse is denoted by a square while the position after the impulse is shown with a triangle in Fig. 42(c) and in Fig.

41. The magnitude of x before the impulse is marked with a thick black horizontal line in Fig. 41; the triangle is placed in the nearest trench in the pattern of H-ranks in Fig. 41.

3.9. Conclusions

The convergence to Arnold tongues was studied in the present chapter. The existence of phase-locked regions in the circle map is a well-known and explored topic in the area of discrete nonlinear iterative maps. Yet it appears that the process of convergence to Arnold tongues is far from being trivial. Such complexity of transient processes constitutes an important feature for the applicability of control techniques pertinent to the circle map.

Pictures representing the manifold of non-asymptotic convergence carry not only important physical information but are also aesthetically beautiful.

Non-asymptotic convergence to unstable periodic orbits in non-invertible nonlinear maps is a well-known effect in nonlinear dynamics. However, non-asymptotic convergence is not possible in completely invertible nonlinear maps (otherwise these maps cannot be invertible by default). This chapter presents computational proof of the fact that a pseudo-stable structure of non-asymptotic convergence to an unstable orbit may exist in a completely invertible discrete dynamical system.

A new computational framework for the identification of this pseudo-stable structure attracting to the unstable period-1 repeller in the bouncer model was presented in this chapter. The same framework is easily extendable whenever other completely invertible maps and more complex unstable periodic orbits are concerned.

The attraction of this pseudo-stable structure resembles non-asymptotic convergence to unstable periodic orbits in non-invertible nonlinear maps. Still, this attraction is only temporary since non-asymptotic convergence cannot exist in completely invertible maps. It was demonstrated that this pseudo-stable structure can be effectively exploited for temporary stabilization of unstable periodic orbits.

Patterns of H-ranks represented different dynamics of the system in respect of different period orbits. Our analysis also suggested that we should be more cautious regarding the uniquiness of attractors while controlling a particular dynamical system with H-rank based techniques.

The robustness of the proposed technique for temporary stabilization of unstable periodic orbits in completely invertible maps to external noise was shown. It appears that particular realizations of the Gaussian noise may extend the time interval when transient solutions stay in the surrounding of the unstable periodic orbit. This phenomenon could be explained by the fact that noise may change the stability of nonlinear systems (Hutt, 2008). In other words, the design of efficient control strategies based on external noise is possible.

It was demonstrated that the manifold of non-asymptotic convergence to a stable limit cycle exists in the stroboscopic representation of the transient data of the periodically driven nonlinear pendulum. Even though the stable period-1 limit cycle

was used for that purpose, a similar phenomenon can be observed for stable limit cycles with higher periodicities.

Periodically driven nonlinear pendulum was used as a nonlinear model generating a stable periodic limit cycle. Similar effects could be observed in other nonlinear models of stable limit cycles.

4. *H*-RANKS FOR TIME SERIES ANALYSIS

4.1. Onset of Chaos in the Dynamical System

In this chapter, an algebraic approach based on the rank of a sequence is proposed for the exploration of the onset of chaos in discrete nonlinear dynamical systems. The rank of the partial solution is identified and a special technique based on Hankel matrices is used to decompose the solution into algebraic primitives comprising roots of the modified characteristic equation. The distribution of roots describes the dynamical complexity of a solution and is used to explore the properties of the nonlinear system and the onset of chaos.

The object of this chapter is the exploration of the onset of chaos also by using a computer-algebraic technique. However, the main difference of this approach is that Hankel matrix-based techniques are used instead. The concept of *H*-rank and its applicability for mapping manifolds and the exploration of the system's sensitivity to the initial conditions is introduced in (Ragulskis and Navickas, 2011).

This chapter presents an adaptation of the *H*-rank technique for the investigation of the complexity of transient processes occurring in a discrete nonlinear dynamical system as it approaches the chaotic state. Algebraic decomposition of a discrete sequence is introduced in Section 4.1.1; numerical experiments with the Logistic map are performed in Section 4.1.2; a numerical experiment with real-world time series is presented in Section 4.1.3.

4.1.1. Algebraic Decomposition of a Solution of a Discrete Map

Let us consider a periodic sequence $S=(1,0,4,1,0,4,\ldots)$. It is clear that $HrS=3$ because $d^{(3)}\neq 0$ but $d^{(4)}=\begin{vmatrix}1&0&4&1\\0&4&1&0\\4&1&0&4\\1&0&4&1\end{vmatrix}=0$ and $d^{(4+n)}=0$ for all $n\in\mathbb{N}$.

The characteristic algebraic equation

$$\begin{vmatrix}1&0&4&1\\0&4&1&0\\4&1&0&4\\1&\rho&\rho^2&\rho^3\end{vmatrix}=65\left(1-\rho^3\right)=0 \tag{48}$$

yields roots $\rho_1=1$; $\rho_2=-\frac{1}{2}+i\frac{\sqrt{3}}{2}$; $\rho_3=-\frac{1}{2}-i\frac{\sqrt{3}}{2}$. All the roots are different, thus the linear algebraic system for the identification of coefficients $\{\mu_{k0}\}_{k=1}^{3}$ takes the following form:

$$\begin{bmatrix} 1 & 1 & 1 \\ \rho_1 & \rho_2 & \rho_3 \\ \rho_1^2 & \rho_2^2 & \rho_3^2 \end{bmatrix} \begin{bmatrix} \mu_{10} \\ \mu_{20} \\ \mu_{30} \end{bmatrix} = \begin{bmatrix} 1 \\ 0 \\ 4 \end{bmatrix}. \tag{49}$$

Solutions read as: $\mu_{10} = \frac{5}{3}$; $\mu_{20} = -\frac{1}{3} + i\frac{2}{\sqrt{3}}$; $\mu_{30} = -\frac{1}{3} - i\frac{2}{\sqrt{3}}$. Finally, elements of the sequence can be expressed as:

$$x_n = \frac{5}{3} + \left(-\frac{1}{3} + i\frac{2}{\sqrt{3}}\right)\left(-\frac{1}{2} + i\frac{\sqrt{3}}{2}\right)^n + \left(-\frac{1}{3} - i\frac{2}{\sqrt{3}}\right)\left(-\frac{1}{2} - i\frac{\sqrt{3}}{2}\right)^n; \tag{50}$$

$$n = 0,1,2,\ldots$$

It can be noted that this is not an approximation of elements of the sequence; this expression is actually exact.

Lemma 1. Let us consider $Hr(x_0, x_1, \ldots) = m < +\infty$ and $x_0, x_1, \ldots \in \mathbb{R}$. Then roots ρ_k and coefficients μ_{kl} of the algebraic decomposition of the sequence $\{x_n\}_{n=0}^{+\infty}$ are real or complex conjugate (Ragulskis, Navickas, Palivonaite and Landauskas, 2012).

The proof is as follows:

The algebraic decomposition of sequence $\{x_n\}_{n=0}^{+\infty}$ is defined by Eq. (11) with $\mu_{k,n_k-1} \neq 0$ and $n_1 + n_2 + \cdots + n_k = m$; $n_1, \ldots, n_k, m \in \mathbb{N}$. The equality $\mathrm{Im}\left(\sum_{k=1}^{r}\sum_{l=0}^{n_k-1} \mu_{kl}\binom{n}{l}\rho_k^{n-l}\right) = 0$ holds because $x_0, x_1, \ldots \in \mathbb{R}$. On the other hand, $\mathrm{Im}\left(\overline{\sum_{k=1}^{r}\sum_{l=0}^{n_k-1} \mu_{kl}\binom{n}{l}\rho_k^{n-l}}\right) = 0$ holds too (the top line denotes the complex conjugate). But $\overline{\sum_{k=1}^{r}\sum_{l=0}^{n_k-1} \mu_{kl}\binom{n}{l}\rho_k^{n-l}} = \sum_{k=1}^{r}\sum_{l=0}^{n_k-1} \overline{\mu_{kl}}\binom{n}{l}\left(\overline{\rho_k}\right)^{n-l}$ because $\binom{n}{l} \in \mathbb{R}$. But then $\mathrm{Im}\left(\sum_{k=1}^{r}\sum_{l=0}^{n_k-1} \mu_{kl}\binom{n}{l}\rho_k^{n-l}\right) = \mathrm{Im}\left(\sum_{k=1}^{r}\sum_{l=0}^{n_k-1} \overline{\mu_{kl}}\binom{n}{l}\left(\overline{\rho_k}\right)^{n-l}\right) = 0$; $n \in \mathbb{Z}_0$. The last equality holds if one and only one of the following conditions holds true:

(i) $\mu_{kl}, \rho_k \in \mathbb{R}$;

(ii) $\mu_{kl}, \rho_k \in \mathbb{Z}$ and there exists such $\hat{k}$ that $\rho_{\hat{k}} = \overline{\rho_k}$ and $\mu_{\hat{k}l} = \overline{\mu_{kl}}$ for all $l = 0,1,\ldots,\left(n_{\hat{k}} - 1\right)$; $1 \le k, \hat{k} \le r$; $k \neq \hat{k}$.

End of Proof.

Lemma 2. Let us consider that $\{x_n\}_{n=0}^{+\infty}$ is a real periodic sequence. Then it is necessary and sufficient that all the following statements hold true (Ragulskis et al., 2012):

(i) A real periodic sequence has a rank; $Hr\{x_n\}_{n=0}^{+\infty} = m$.

(ii) All the roots of the algebraic decomposition of the sequence are different; $\rho_k \neq \rho_l$; $k \neq l$; $1 \leq k,l \leq m$.

(iii) Modulus of all the roots are equal to 1; $|\rho_k| = 1$; $k = 1,2,\ldots,m$.

(iv) All ratios $\dfrac{\arg(\rho_k)}{2\pi}$; $k = 1,2,\ldots,m$ are rational numbers.

The proof is as follows:

(i) Since the sequence $\{x_n\}_{n=0}^{+\infty}$ is periodic, there exists such $p \in \mathbb{N}$ that $x_{n+p} = x_n$ for all $n \in \mathbb{Z}_0$. Then Hankel matrices $H^{(p+k)}$; $k \in \mathbb{N}$ contain at least two identical rows and therefore $\det H^{(p+k)} = 0$ for all $k \in \mathbb{N}$. Thus $\exists m \leq p$, and this m equals $Hr\{x_n\}_{n=0}^{+\infty}$.

(ii) $\{x_n\}_{n=0}^{+\infty}$ is a periodic sequence and it can be extended into periodic sequence $\{x_n\}_{n=-\infty}^{+\infty}$. Moreover, there exists such $0 < M < +\infty$ that $|x_n| < M$ for all $n \in \mathbb{Z}$ because $\{x_n\}_{n=-\infty}^{+\infty}$ is a periodic sequence. Let us assume that $Hr\{x_n\}_{n=0}^{+\infty} = m \leq p$ and that there exist two equal roots: $\rho_{m-1} = \rho_m$ but all other roots are different. Then, according to Eq. (11):

$$x_n = \sum_{k=1}^{m-1} \mu_{k0}\rho_k^n + \mu_{(m-1),1} n \rho_{m-1}^{n-1};\ n \in \mathbb{Z};\ \mu_{(m-1),1} \neq 0. \tag{51}$$

But then there exists such $n_0 \geq 0$ that $|x_n| \geq M$ for all $|n| \geq n_0$, which contradicts the requirement that $\{x_n\}_{n=0}^{+\infty}$ is a periodic sequence. Analogous contradictions occur when the number of equal roots is higher.

(iii) The proof is analogous to the proof of (ii). Let us assume that $|\rho_k| > 1$; $1 \leq k \leq m$. Then there exists such $n_0 \geq 0$ that $|x_n| \geq M$ for all $n \geq n_0$. Now, let us assume that $0 < |\rho_k| < 1$; $1 \leq k \leq m$. Then there exists such $n_0 \geq 0$ that $|x_n| \geq M$ for all $n \leq -n_0$.

(iv) Lemma 1 and statements (i), (ii) and (iii) yield:

$$x_n = \sum_{k=1}^{m} \mu_{k0} \exp(in\phi_k);\ n \in \mathbb{Z}; \tag{52}$$

where $i^2 = -1$; $\phi_k = \arg(\rho_k)$; $-\pi \le \phi_k < \pi$. The sequence $\{x_n\}_{n=0}^{+\infty}$ is periodic if and only if $\frac{\phi_k}{2\pi}$ is a rational number for all $k = 1,2,\ldots m$. Then, Eq. (52) reads:

$$x_n = \sum_{k=1}^{m} \mu_{k0} \exp\left(i2\pi n \frac{a_k}{b_k} \right); \; n \in \mathbb{Z}; \tag{53}$$

where $a_k \in \mathbb{Z}$; $b_k \in \mathbb{N}$ for all $k = 1,2,\ldots m$. Let p be the least common multiple of $b_1, b_2, \ldots, b_m$; $p \in \mathbb{N}$. Thus p is the period of the sequence $x_{n+p} = x_n$; $n \in \mathbb{Z}$. Then, $\exp\left(i2\pi p \frac{a_k}{b_k} \right) = 1$ for all $k = 1,2,\ldots m$.

End of Proof.

4.1.2. Numerical Experiments with the Logistic Map

Logistic map is a paradigmatic model used to illustrate the evolution of a simple nonlinear system to chaos (Strogatz, 2014). As mentioned before, the discrete dynamical map $x_{n+1} = r \cdot x_n (1 - x_n)$ comprises one control parameter r; the interval $0 \le r \le 4$ will be investigated here below.

The algorithm used for the computation of the rank of sequence *S* constructed as an iterative solution of the Logistic map starting from the initial condition x_0 and at a fixed value of the parameter *a* is rather straightforward (Ragulskis and Navickas, 2011). A sequence of matrices $H^{(m)}$; $m = 2,3,\ldots$ is formed. Theoretically, this process should be continued until such *m* when $\det\left(H^{(m+k)}\right) = 0$ for all $k = 1,2,\ldots$. Unfortunately, as shown before, the rank of a chaotic time series does not exist. Therefore the sequence of Hankel matrices is limited by setting the upper bound for *m*. The process is terminated if the sequence of the determinants does not vanish until *m* has reached the predefined upper bound $\overline{m}$.

As well as in the previous chapters, the computation of determinants is executed until $\left|\det\left(H^{(m)}\right)\right| < \varepsilon$. Such computations reveal not the rank but rather the pseudorank of a sequence. It must be noted that the upper bound of the rank and the machine *epsilon* must be preselected individually for each specific discrete iterative map. One of the objectives of this chapter is to present an adaptive strategy for the selection of the optimal rank and one more strategy for an/the optimal value of ε (an alternative for the approach presented in chapter 2) for any concrete sequence *S*.

First of all, it is demonstrated that a higher value of ε may be better (a precise criterion for the comparison is defined) than a lower value of ε (but still higher than the machine *epsilon*). Let us construct an iterative sequence of the Logistic map (Eq. (13)) at $a = 3.59$ starting from $x_0 = 0.5$. Initially, let us fix $\varepsilon = 10^{-10}$ and $\overline{m} = 50$. A sequence of Hankel matrices $\left\{H^{(k)}\right\}$ is constructed and a sequence of determinants

$\left\{d^{(k)}\right\}$; $k = 2,3,\ldots$ is computed until $\left|d^{(k)}\right| < 10^{-10}$ or $k \geq 50$. It appears that $\left|d^{(16)}\right| < 10^{-10}$. The characteristic algebraic equation then yields 16 roots; all the roots are shown in Fig. 43(a) (it can be noted that all the roots are different). A unit radius circle in the complex plane is drawn in Fig. 43(a), which helps to interpret the modulus of each root.

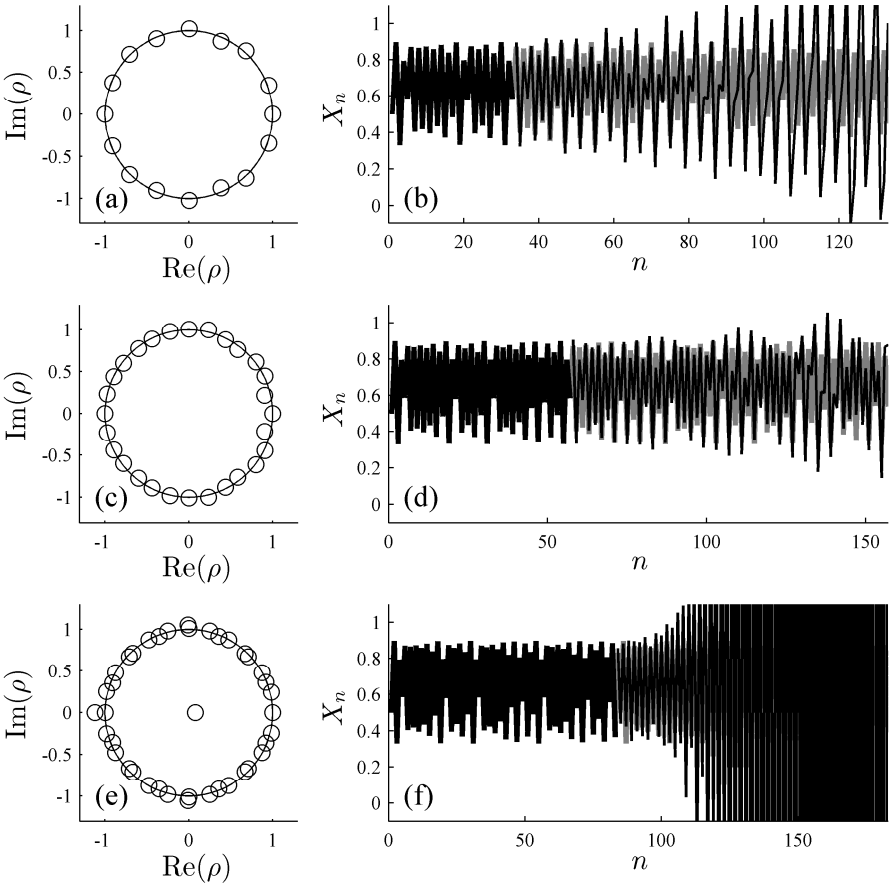

Fig. 43. Algebraic decomposition of transient processes of the Logistic map at $a = 3.59$ and $x_0 = 0.5$ at $\varepsilon = 10^{-10}$ (a, b); at $\varepsilon = 10^{-19}$ (c, d) and at $\varepsilon = 10^{-30}$ (e, f). The distribution of roots is shown in (a), (c) and (e); transient processes (thick gray solid lines), base fragments (thick black solid lines) and extrapolated sequences (thin black solid lines) are shown in (b) ($HrS = 16$); (d) ($HrS = 28$) and (f) ($HrS = 41$)

The base fragment of the sequence is thus $\left(x_0, x_1, x_2, \ldots, x_{29}, x_{30}\right)$. This fragment is plotted by using a thick black solid line in Fig. 43(b). The following Eq. (11) is employed to extrapolate the sequence for 100 steps into the future. The iterated sequence of the Logistic map is plotted by using a thin black solid line and the extrapolated sequence – a thin black solid line in Fig. 43(b). It can thus be

observed that the extrapolated sequence follows the evolution of the Logistic map quite well for about 20 steps, but errors start accumulating later.

Analogous numerical experiments are repeated for $\varepsilon = 10^{-19}$ (Fig. 43(c), (d)) and $\varepsilon = 10^{-30}$ (Fig. 43(e), (f)). In order to assess differences between iterated and extrapolated sequences, the measure of the extrapolation errors E – which is a standard RMSE (root mean square error) – is introduced:

$$E = \sqrt{\frac{1}{100}\sum_{n=2m-1}^{2m+98}\left(x_n - \tilde{x}_n\right)^2} \tag{54}$$

where $\tilde{x}_n$ denotes elements of the extrapolated sequence. It can be noted that $\tilde{x}_n$ would be equal to x_n for all $n \geq 2m-1$ if ε were equal to 0.

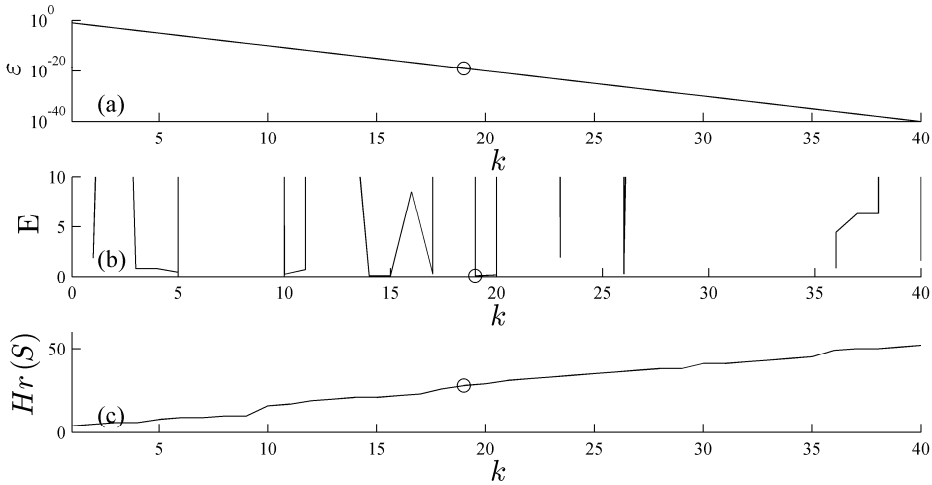

Fig. 44. The minimization of extrapolation errors for the Logistic map at $r = 3.59$ and $x_0 = 0.5$. Computations are performed for $\varepsilon = 10^{-k}$; $k = 1, 2, \ldots, 40$ (a); extrapolation errors are shown in (b); ranks are demonstrated in (c). Minimal extrapolation errors are achieved at $k = 19$ and are denoted by circles

It is clear that extrapolation error E depends on ε (Fig. 43). Therefore it is important to identify such ε which would result in the minimal E. The process of minimization of extrapolation errors at $r = 3.59$ and $x_0 = 0.5$ is illustrated in Fig. 44. Computations for $\varepsilon = 10^{-k}$; $k = 1, 2, \ldots, 40$ are performed (Fig. 44(a)). Extrapolation errors and ranks at different ε are shown in Fig. 44(b) and (c). The minimal value of extrapolation errors is achieved at $k = 19$ and is denoted by circles in Fig. 44(a), (b) and (c). It can be noted that all further computations are performed by using the above described technique for the adaptive selection of the optimal value of ε for each and every particular iterative sequence.

First, the effect of the initial condition on the algebraic decomposition of the solution of the Logistic map is demonstrated in Fig. 45. The value of the parameter $r = 3.55$ is selected; this results in a period-4 attractor after transient processes have

ceased down. Three different initial conditions are selected: $x_0 = 0.01$ (Fig. 45(a), (b)); $x_0 = 0.25$ (Fig. 45(c), (d)) and $x_0 = 0.5$ (Fig. 45(e), (f)). The distribution of roots is shown in Fig. 45(a), (c) and (e); transient processes are shown in Fig. 45(b), (d) and (f). It can be noted that extrapolations of iterative processes are so good that no visual differences can be observed between the solution and the extrapolated sequence after 100 steps.

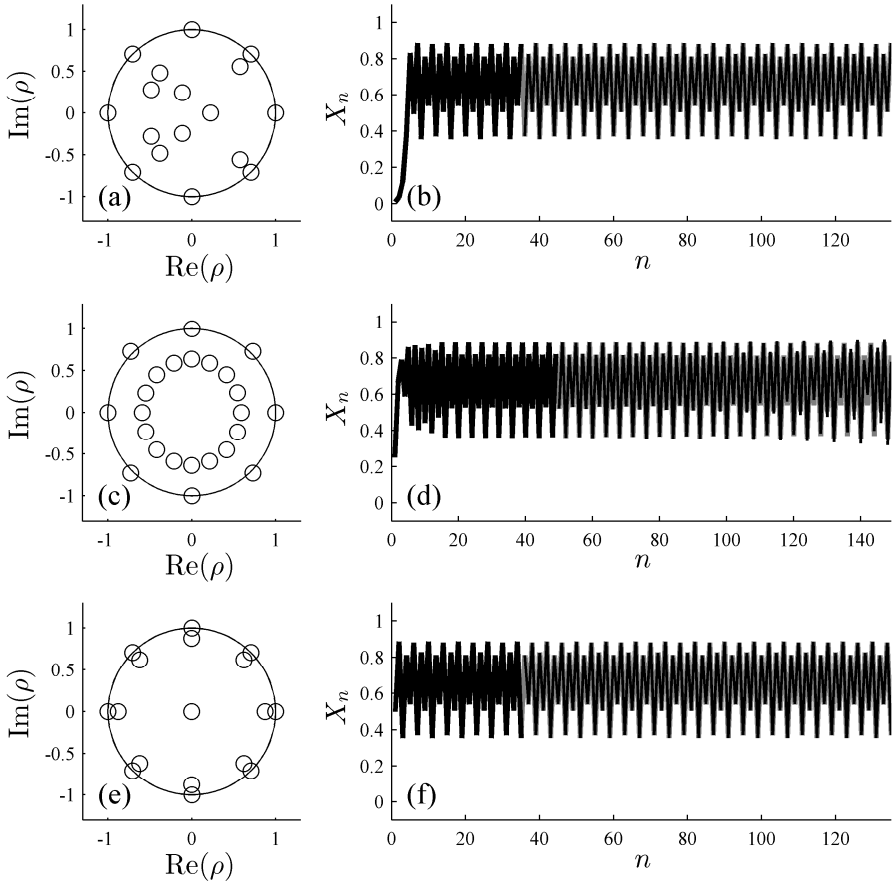

Fig. 45. Algebraic decomposition of transient processes of the Logistic map at $r = 3.55$ and $x_0 = 0.01$ (a, b); $x_0 = 0.25$ (c, d) and $x_0 = 0.5$ (e, f). The distribution of roots is shown in (a), (c) and (e); transient processes (thick gray solid lines), base fragments (thick black solid lines) and extrapolated sequences (thin black lines coinciding with thin black lines) are shown in (b) ($HrS = 17$; $\varepsilon = 10^{-36}$); (d) ($HrS = 24$; $\varepsilon = 10^{-36}$) and (f) ($HrS = 17$; $\varepsilon = 10^{-36}$)

2-dimensional plots of the rank as a function of the parameter a and the initial condition x_0 are used in (Ragulskis and Navickas, 2011) in order to reveal the intertwined structure of the stable and the unstable manifold and the manifold of non-asymptotic convergence of the Logistic map. Since the primary object of the

section is to explore the onset of chaos by using algebraic techniques, the same initial condition $x_0 = 0.5$ is fixed for all the values of parameter r.

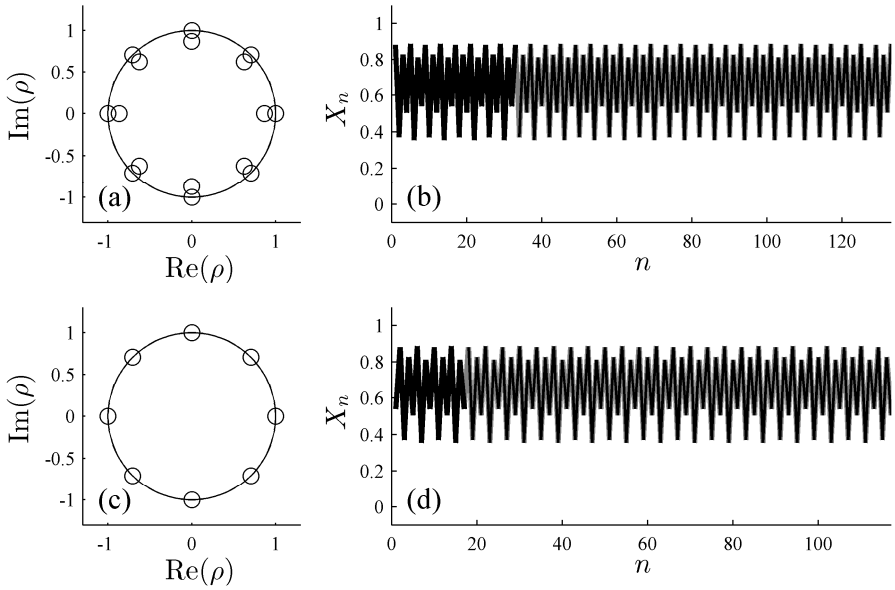

Fig. 46. Algebraic decomposition of iterated sequences produced by the Logistic map at $r = 3.55$ and $x_0 = 0.5$ as the 5 initial steps are omitted (a, b) and the first 500 steps are omitted (c, d). The distribution of roots is shown in (a) and (c); transient processes (thick gray solid lines), base fragments (thick black solid lines) and extrapolated sequences (thin black lines coinciding with thin black lines) are shown in (b) ($HrS = 16$; $\varepsilon = 10^{-36}$) and (d) ($HrS = 8$; $\varepsilon = 10^{-36}$)

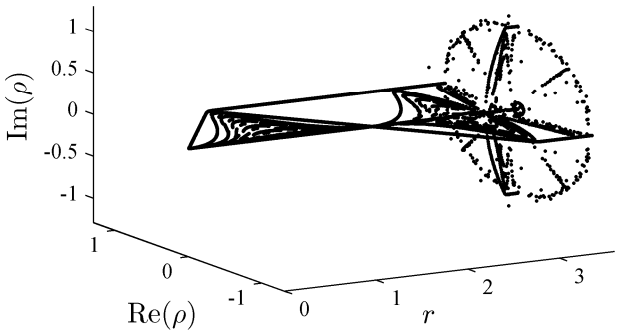

Fig. 47. The distribution of roots of the characteristic algebraic equation for the Logistic map in the range $0 < r < 3.6$

Before continuing with the variation of r, the effect of transient processes to the algebraic decomposition of the solution is investigated (Fig. 46). The value of parameter r is still the same as in the previous experiment; $x_0 = 0.5$. But now the

first 5 steps are omitted (Fig 46(a), (b)) and then the initial 500 steps (Fig. 46(c), (d)) of the iterative process are also skipped. The algebraic complexity of the analyzed iterative sequences becomes simpler when initial transient processes are omitted (let us compare this to Fig. 45(e), (f)). Lemma 2 is well illustrated with Fig. 45(e), (a), (c). Roots with the modulus lower that 1 become zero when transient processes are not considered. The periodic attractor (the length of the period is 8 iterates) is represented by 8 different roots located on the unit radius circle on the complex plane; all the roots are real or complex conjugate. The ratios $\arg(\rho_k)/2\pi$; $k = 1,2,\ldots,8$ read: 0; $\frac{1}{8}$; $\frac{1}{4}$; $\frac{3}{8}$; $\frac{1}{2}$; $-\frac{3}{8}$; $-\frac{1}{4}$ and $-\frac{1}{8}$; the least common multiple of denominators is $p = 8$, which corresponds to the length of the period.

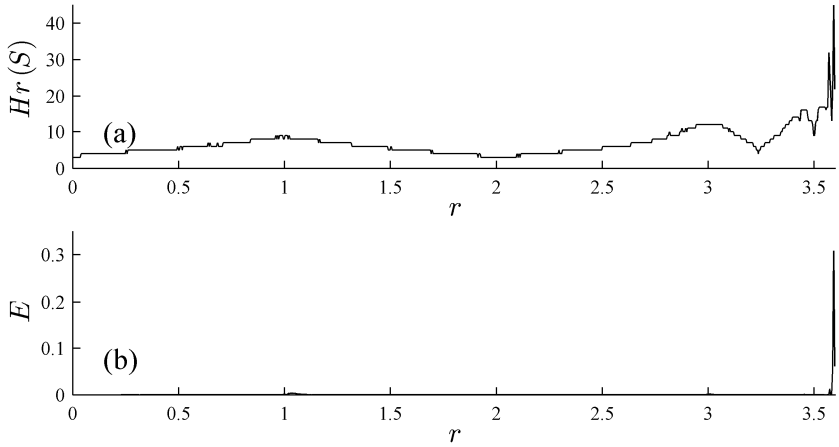

Fig. 48. The variation of the rank of the algebraic representation of the solution of the Logistic map (a) and extrapolation errors (b) in the range $0 < r < 3.6$

Nevertheless, the onset of chaos is explored here by not omitting transient processes because, first of all, it is quite complicated to identify at which concrete step a transient process ceases down, and, secondly, the length of transient processes varies with r. Since the object of the investigation is an algebraic approach towards the onset of chaos, the iterative process of the Logistic map at different values of r ($0 < a < 3.6$) starts, the optimal algebraic representation of every iterative process is computed, and the roots in the complex plane are plotted for every discrete value of r. The computational experiments are limited at $r = 3.6$ because the Logistic map approaches the chaotic regime where the algebraic representation cannot be useful any more (a chaotic sequence does not have a rank). The produced 3D image is shown in Fig. 47 (each dot here represents a single root of the characteristic algebraic equation).

The evolution of the rank of the algebraic representation of the solution and extrapolation errors is shown in Fig. 48. It is interesting to note that the rank of the solution abruptly jumps over the computational limit (Fig. 48(a)) as the solution becomes chaotic. Extrapolation errors also grow because an algebraic progression cannot represent a chaotic solution (Fig. 48(b)).

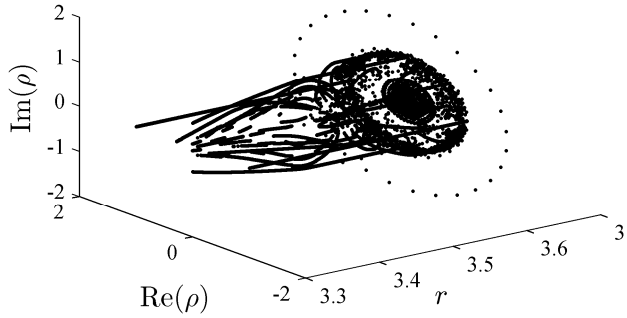

Fig. 49. The distribution of roots of the characteristic algebraic equation for the Logistic map in the range $3.3 < r < 3.6$

In order to visualize the onset of chaos in more detail, computational experiments are repeated and zoom the image of the distribution of roots in the range $3.3 < r < 3.6$ (Fig. 49). One can observe intricate transitions of roots in the complex space until the regular structure of the distribution of roots is lost when the parameter r approaches 3.6. As mentioned previously, Fig. 49 is produced by stepwise incrementing of parameter r.

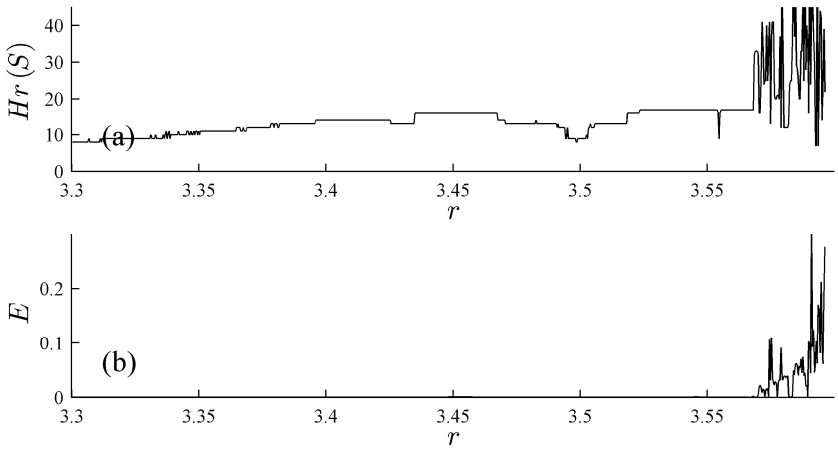

Fig. 50. The variation of the rank of the algebraic representation of the solution of the Logistic map (a) and extrapolation errors (b) in the range $3.3 < r < 3.6$

It is of interest to note that the correlation between the distribution of roots at two consequent discrete values of parameter r is high until the Logistic map approaches the zone of chaotic solutions. There is no observable correlation left between the roots of algebraic representations of solutions at the consequent discrete value of parameter r as the system approaches the chaotic attractor; the variation of the rank and extrapolation errors become unpredictable there as well (Fig. 50).

4.1.3. Numerical Experiments with Real-world Time Series

So far algebraic techniques for the exploration of the onset of chaos in discrete iterative systems have been explored here. The applicability of the presented algebraic technique for real-world time series will be demonstrated in this section. The ability to reconstruct the approximating algebraic model of the time series (especially if this series is chaotic and/or contaminated with inevitable noise) would enable the algebraic extrapolation of the time series into the future. The concept of skeleton algebraic sequences is dealt with in (Ragulskis et al., 2011) for the prediction of complex real-world time series. Direct adaptive decomposition of the real-world time series into algebraic primitives (by using the algorithm presented in Section 3) would offer an alternative approach for the construction of an adaptive prediction algorithm.

Two standard real-world time series were selected for computational experiments: (1) the normalized monthly mean temperatures in southwestern mountain region over a time period starting in the year 1932 (Hyndman) and (2) an excerpt from normalized daily net retail sales (Hyndman). Fig. 51(b) shows the best extrapolation (in terms of RMSE) of the normalized monthly mean temperatures in the southwestern mountain region for 100 steps into the future; the distribution of the roots is shown in Fig. 51(a). The best algebraic approximation is reached at $\varepsilon = 10^{-12}$ and $HrS = 21$; this results in the extrapolation error $E = 0.245$.

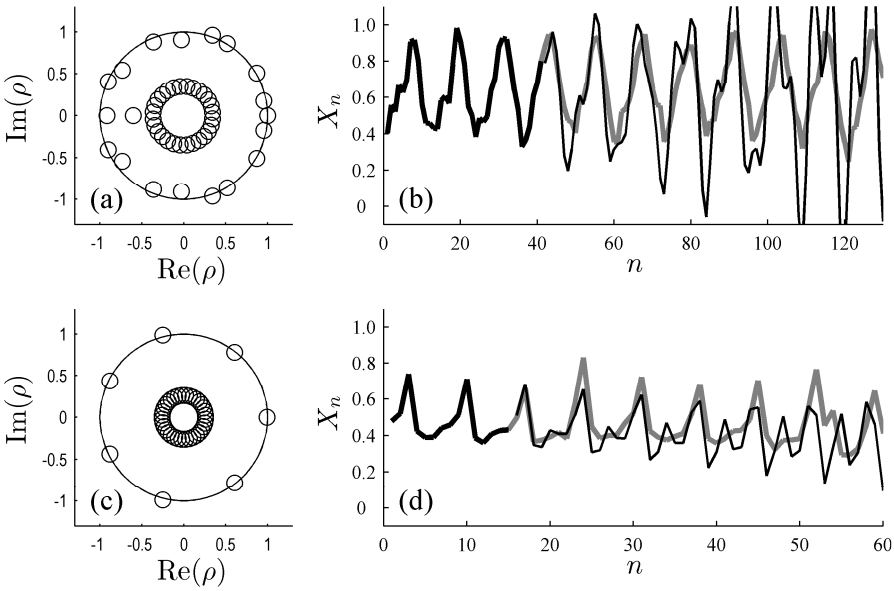

Fig. 51. Algebraic extrapolation of real-world time series: the normalized monthly mean temperatures in the southwestern mountain region over a time period starting in the year 1932 (a, b) and an excerpt from normalized daily net retail sales (c, d). The distribution of the roots is shown in (a) and (c); transient processes (thick gray solid lines), base fragments (thick black solid lines) and extrapolated sequences (thin black lines) are shown in (b) ($HrS = 21$; $\varepsilon = 10^{-12}$) and (d) ($HrS = 8$; $\varepsilon = 10^{-4}$)

Fig. 51(d) shows the best algebraic extrapolation of the excerpt from normalized daily net retail sales. We should note that this time series is short and that there is not enough data to compute the error of extrapolation for 100 steps into the future. The best approximation is reached at $\varepsilon = 10^{-4}$ and $HrS = 8$ which results in the extrapolation error $E = 0.112$.

4.2. The Reconstruction of Skeleton Sequences Based on the *H*-rank

The algorithm for the reconstruction of the model of LRS from a sequence $\{x_j\}_{j=0}^{+\infty}$ is more complex if the order of LRS is not known beforehand. Hankel transform of $\{x_j\}_{j=0}^{+\infty}$ yields the sequence $\{h_j\}_{j=0}^{+\infty}$ where $h_j = \det H_j$ and $H_j = (x_{k+l-2})_{1\le k,l\le(j+1)}$ is a Hankel catalecticant matrix (matrix dimensions are $(j+1)\times(j+1)$). If there exists such $n \ge 1$ that $h_n \ne 0$ but $h_k = 0$ for all $k \ge n+1$, then $\{x_j\}_{j=0}^{+\infty}$ is LRS, its order is n , and auxiliary equation 2 now reads:

$$\begin{vmatrix} x_0 & x_1 & \cdots & x_n \\ x_1 & x_2 & \cdots & x_{n+1} \\ \cdots & \cdots & \cdots & \cdots \\ x_{n-1} & x_n & \cdots & x_{2n-1} \\ 1 & \rho & \cdots & \rho^n \end{vmatrix} = 0. \tag{55}$$

As mentioned previously, only the case when roots of (55) are all distinct is considered here. Then the recurrence is uniquely described by (6).

Example 1. Let us consider a period-4 sequence $\{1,0,-1,0,1,\ldots\}$ (we should note that periodic sequences comprise only a small fraction of the set of all possible LRS). It is clear that the order of this sequence is 2 because $\begin{vmatrix} 1 & 0 & -1 \\ 0 & -1 & 0 \\ -1 & 0 & 1 \end{vmatrix}$ and all higher determinants are equal to 0. Then, the auxiliary equation reads:

$$\begin{vmatrix} 1 & 0 & -1 \\ 0 & -1 & 0 \\ 1 & \rho & \rho^2 \end{vmatrix} = -\left(1+\rho^2\right) = 0. \tag{56}$$

Two distinct roots read: $\rho_1 = i$; $\rho_2 = -i$. Coefficients μ_k are determined from:

$$\begin{bmatrix} 1 & 1 \\ \rho_1 & \rho_2 \end{bmatrix} \cdot \begin{bmatrix} \mu_1 \\ \mu_2 \end{bmatrix} = \begin{bmatrix} 1 \\ 0 \end{bmatrix}; \mu_1 = \frac{1}{2}; \mu_2 = \frac{1}{2}. \tag{57}$$

Thus, finally,

$$x_j = \frac{1}{2} i^j + \frac{1}{2}(-i)^j ; j = 0,1,2,\ldots. \tag{58}$$

Let us use this period-3 sequence and construct the following Hankel matrix:

$$H_4 = \begin{bmatrix} 1 & 0 & -1 & 0 & 1 \\ 0 & -1 & 0 & 1 & 0 \\ -1 & 0 & 1 & 0 & -1 \\ 0 & 1 & 0 & -1 & 0 \\ 1 & 0 & -1 & 0 & 1 \end{bmatrix} \tag{59}$$

SVD of H_4 results in identical matrices U and V because $H_4^T H_4 = H_4 H_4^T$. The equality $\left|H_4^T H_4 - \lambda I\right| = 0$ yields the eigenvalues of $H_4^T H_4$:

$$\left|H_4^T H_4 - \lambda I\right| = \begin{vmatrix} 3-\lambda & 0 & -3 & 0 & 3 \\ 0 & 2-\lambda & 0 & -2 & 0 \\ -3 & 0 & 3-\lambda & 0 & -3 \\ 0 & -2 & 0 & 2-\lambda & 0 \\ 3 & 0 & -3 & 0 & 3-\lambda \end{vmatrix} = \lambda^3\left(13\lambda - \lambda^2 - 36\right) = 0; \tag{60}$$

$$\lambda_1 = 9,\ \lambda_2 = 4 \text{ and } \lambda_{3,4,5} = 0.$$

Lemma 3. Let $\left\{x_j\right\}_{j=0}^{+\infty}$ be an LRS and its order be n. Let H_j be a $(j+1)$ order Hankel matrix of $\left\{x_j\right\}_{j=0}^{+\infty}$. Then the number of singular values of H_j not equal to zero is not higher than n.

The proof is as follows. Without the loss of generality let us assume a non-increasing order of the absolute values of the eigenvalues of H_j: $\left|\lambda_1\right| \geq \left|\lambda_2\right| \geq \ldots \geq \left|\lambda_{j+1}\right|$.

We should note that $H_j = H_j^T$; thus singular values σ_k are the square roots of eigenvalues of H_j^2 which are equal to λ_k^2, $k = 1,\ldots,l$ where l is the number of distinct eigenvalues (Starzak, 2013). Then $\sigma_k = \left|\lambda_k\right|$, $k = 1,\ldots,j+1$ since the singular values are computed without taking multiplicity into account.

Let us consider $j \leq n-1$. The order of $\left\{x_j\right\}_{j=0}^{+\infty}$ is n. Thus $\det(H_j) \neq 0$; $\lambda_1\lambda_2\ldots\lambda_{j+1} \neq 0$, and the number of zero singular values is 0.

Now, let us suppose that $j > n-1$. The nullity of H_j reads: $nul\left(H_j\right) = j+1-rank\left(H_j\right) = j+1-n$. The multiplicity of the zero eigenvalue of a matrix is equal to its nullity; thus $\sigma_1,\ldots,\sigma_n \neq 0$; $\sigma_{n+1},\ldots,\sigma_{j+1} = 0$.

End of Proof.

Lemma 3 implies that SVD of the Hankel matrix of a sequence can be used as an effective computational tool for the determination of its order – if only this sequence is a LRS. However, every real-world time series is contaminated with inevitable noise. Thus the order of a real-world time series is infinite as even the evolution of the underlying model is governed by a LRS.

Let us assume that $\left\{x_j\right\}_{j=0}^{+\infty}$ is an order n LRS and $\left\{\varepsilon_j\right\}_{j=0}^{+\infty}$ is a discrete random variable. Then sequence $\left\{x_j+\varepsilon_j\right\}_{j=0}^{+\infty}$ is not a LRS – however small the additive noise is (otherwise $\left\{\varepsilon_j\right\}_{j=0}^{+\infty}$ would be a LRS – which contradicts the definition of a random variable). In other words, the computational procedure described in Lemma 1 is not applicable for the detection of the order of LRS – if only the investigated sequence is a real-world time series. Another approach is required for real-world time series.

Properties and computational aspects of the pseudospectrum of a square matrix are discussed in detail in (Wright and Trefethen, 2002). Similar reasoning in respect of the pseudo-order of LRS could help to understand the effects introduced by the additive noise.

The spectrum of a square matrix A denoted as $\Lambda\left(A\right)$ is the set of $z \in \mathbb{C}$ where the resolvent $\left(zI-A\right)^{-1}$ does not exist or is unbounded (Trefethen, 1999) where I is the identity matrix. The ε -pseudospectrum of A is the set

$$\Lambda_\varepsilon\left(A\right) = \left\{z \in \mathbb{C} : z \in \Lambda\left(A+E\right) \text{ for some } E \text{ with } \left\|E\right\| < \varepsilon\right\} \tag{61}$$

for each $\varepsilon > 0$. As an analogy to the classical definition of the spectrum of a square matrix, the *H*-spectrum of the LRS as the set of roots of auxiliary equation (55) is defined:

$$P\left(x_0, x_1, \ldots, x_{2n-1}\right) = \left\{\rho_k\right\}_{k=1}^{n}. \tag{62}$$

Then the ε -*H*-spectrum of a square Hankel matrix is defined as:

$$P_\varepsilon\left(x_0, x_1, \ldots, x_{2n-1}\right) = P\left(x_0+\varepsilon_0, x_1+\varepsilon_1, \ldots, x_{2n-1}+\varepsilon_{2n-1}\right) \tag{63}$$

for some $\varepsilon_0, \varepsilon_1, \ldots, \varepsilon_{2n-1} \in \mathbb{R}$ so that $\left\|\varepsilon_0\, \varepsilon_1 \ldots \varepsilon_{2n-1}\right\|_2 \leq \varepsilon$.

Such a definition of the ε -*H*-spectrum *does* enable computational investigation of the effects introduced by the additive noise. In other words, such an approach helps us investigate such real-world time series where an underlying LRS is contaminated with noise.

We should note that the coefficients of auxiliary equation (55) are computed as cofactors in respect to the last line of determinant (55). But,

$$\det\left(A+\varepsilon E\right)=\det\left(A\right)+\det\left(A\right)tr\left(A^{-1}E\right)\cdot\varepsilon+O\left(\varepsilon^{2}\right). \tag{64}$$

In other words, the ε-*H*-spectrum converges continuously to the *H*-spectrum as $\varepsilon\to 0$ if only A is not singular (which is true if the size of the Hankel matrix does correspond to the order of the LRS). Also, all the roots of the perturbed sequence are either real numbers or complex conjugate numbers because the perturbation does not damage the symmetricity of the matrix.

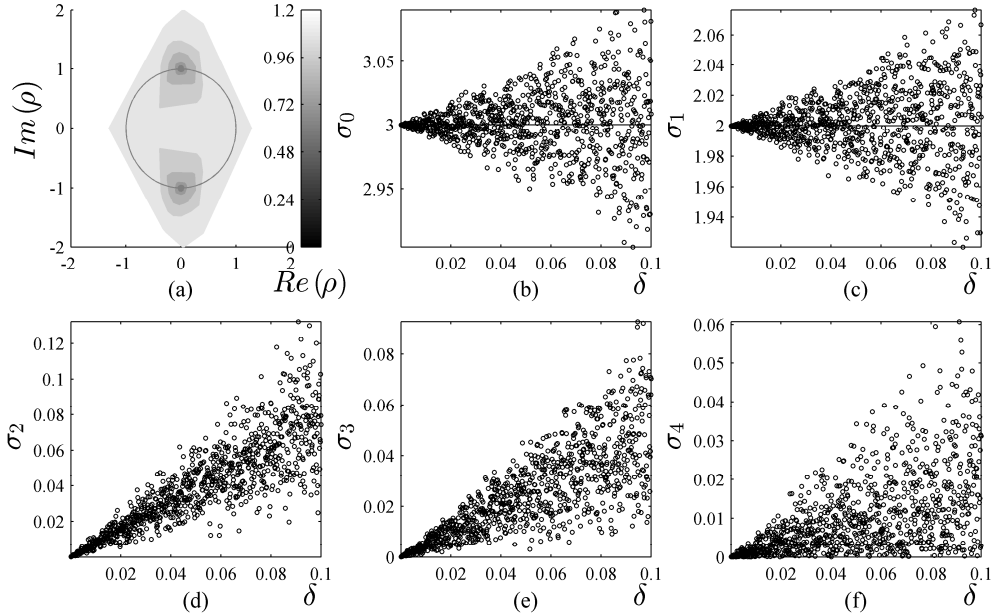

Fig. 52. The continuous convergence of ε-*H*-spectrum to the *H*-spectrum as $\varepsilon\to 0$. The distribution of roots of the auxiliary equation for the perturbed sequence in Example 2 is illustrated in part (a). The continuous convergence of SVD Eigenvalues σ_k; $k=\overline{0,4}$ of the perturbed matrix H_4 is illustrated in parts (b-f)

Example 2. Let us consider the same sequence from Example 1 – but perturb it by adding the external noise. Let us assume that $\varepsilon=0.1$. We should note that 4 elements of the sequence are required for auxiliary equation (55). Let us assume that $\tilde{\varepsilon}_0=0.1$; $\tilde{\varepsilon}_1=-0.5$; $\tilde{\varepsilon}_2=0.3$ and $\tilde{\varepsilon}_3=-0.2$ (it would be convenient to generate $\tilde{\varepsilon}_k$ as random numbers distributed uniformly over the interval $\left(-1,1\right)$). However, $\tilde{n}=\left\|\tilde{\varepsilon}_0\,\tilde{\varepsilon}_1\,\tilde{\varepsilon}_2\,\tilde{\varepsilon}_3\right\|_2\approx 0.6245\neq 0.1$. Here $\left\|\cdot\right\|_2$ is l^2-norm. The perturbation takes the form:

$$\varepsilon_k=\varepsilon\cdot\frac{\tilde{\varepsilon}_k}{\tilde{n}};k=\overline{0,3}. \tag{65}$$

Note that now $\|\varepsilon_0\ \varepsilon_1\ \varepsilon_2\ \varepsilon_3\|_2 = \varepsilon$. The perturbed auxiliary equation reads:

$$\begin{vmatrix} 1.0160 & -0.0801 & -0.9520 \\ -0.0801 & -0.9520 & -0.0320 \\ 1 & \rho & \rho^2 \end{vmatrix} = -0.9736\rho^2 + 0.1088\rho - 0.9037 = 0. \qquad (66)$$

Finally, $P_{0.1}(x_0, x_1, \ldots, x_{2n-1}) = \{0.0559 \pm 0.9618i\}$. Repeating this computational experiment many times helps to plot "clouds" of roots of perturbed auxiliary equations (Fig. 52a). Computational experiments illustrate the continuous convergence of the ε-*H*-spectrum to the *H*-spectrum as $\varepsilon \to 0$.

Similar computational experiments can be performed for the eigenvalues of $H_4^T H_4$. We should note that the length of the perturbation vector is 9 (H_4 is a square Hankel matrix of order 5). The perturbation does not damage the symmetricity of the matrix; the matrix remains catalecticant. SVD of H_4 produces 5 eigenvalues – all of them are shown in Fig. 52b, 52c, 52d, 52e and 52f accordingly. As an opposition to the previous experiment with the auxiliary equation, a single perturbation is performed for each and every discrete value of ε. It can be seen that SVD eigenvalues of the perturbed matrix do converge continuously to eigenvalues of H_4 as $\varepsilon \to 0$. Moreover, SVD of the Hankel matrix of a perturbed sequence can still be used as an effective computational tool for the determination of the order of the non-perturbed sequence – one just needs to set up the error level and count how many eigenvalues are higher than this error level. The techniques for the selection of this error level are discussed in the subsequent sections.

4.2.1. Weighted Moving Average and the Order of LRS

The classical moving average (MA) method transforms the original sequence $\{x_j\}_{j=0}^{+\infty}$ into sequence

$$\{y_j\}_{j=0}^{+\infty} = \left\{ \frac{1}{L} \sum_{s=0}^{L-1} x_{s+j} \right\}_{j=0}^{+\infty} \qquad (67)$$

where L is the width of the observation window.

The weighted moving average method WMA(L) differs from MA(L) in the sense that the weight coefficients w_s are not equal:

$$\{y_j\}_{j=0}^{+\infty} = \left\{ \sum_{s=0}^{L-1} w_{L-s} x_{s+j} \right\}_{j=0}^{+\infty}. \qquad (68)$$

The most popular WMA(L) is the exponential MA method. In the simplest form it is described by the recurrent relation:

$$y_j = \alpha x_j + (1-\alpha) y_{j-1};\ j = 2, 3, \ldots, \qquad (69)$$

where $\alpha \in (0;1)$ is a smoothing factor. Anterior samples exhibit lower significance in this model but are obligatory for the reconstruction of the original signal as opposed to MA.

Let us consider that $\{x_j\}_{j=0}^{+\infty}$ is a LRS. It is clear that WMA(L) does transform a LRS into a LRS. Equations (7) and (67) yield:

$$y_j = \sum_{s=0}^{L-1} w_{L-s} \sum_{k=1}^{r} \sum_{l=0}^{n_k-1} \mu_{kl} \binom{s+j}{l} \rho_k^{s+j-l} = \sum_{k=1}^{m} \sum_{t=0}^{n_k-1} \tilde{\mu}_{kt} j^t \rho_k^j \tag{70}$$

In general, the order of $\{y_j\}_{j=L-1}^{+\infty}$ can be higher than the order of $\{x_j\}_{j=0}^{+\infty}$. But it may happen that a particular combination of weight coefficients w_k and roots ρ_k may result in such situations when some of the expressions $\tilde{\mu}_{kr}$ which also depend on the coefficients w_s become equal to zero. In such cases, the order of the transformed LRS can become lower than the order of the original sequence.

Example 3. Let us consider a sequence of period-6. Let this sequence be described by the roots of the characteristic equation $\rho_k = e^{\frac{\pi}{3}(k-1)i}$, $k = \overline{1,6}$.

One must choose μ values in the way that makes y_j, $j = 1,2,\ldots$ be real numbers. Thus let us consider:

$$\begin{aligned} &\mu_1 = 0.5,\ \mu_2 = -0.2 + 0.1i,\ \mu_3 = 0.3 + 0.2i, \\ &\mu_4 = -0.3,\ \mu_5 = 0.3 - 0.2i,\ \mu_6 = -0.2 - 0.1i. \end{aligned} \tag{71}$$

The defined variables result in a period-6 sequence with the initial members:

$$\begin{aligned} &0.4,\ 0.3 - 0.3\sqrt{3},\ 0.1 + 0.1\sqrt{3}, \\ &1.8,\ 0.1 - 0.1\sqrt{3},\ 0.3 + 0.3\sqrt{3},\ldots \end{aligned} \tag{72}$$

Let us consider $L = 6$ and $w_i = \frac{1}{6}$, $i = \overline{1, L-1}$. It is natural that filtering the sequence yields a new constant sequence $\frac{1}{2}, \frac{1}{2}, \frac{1}{2}\ldots$.

But let us suppose that $L = 4$ and $\{w_i\}_{i=0}^{3} = \{0.1;0.4;0.4;0.1\}$. Now, the resulting new sequence is of period-6 but it still possesses 2 elements which are the same:

$$\begin{aligned} &0.38 - 0.08\sqrt{3},\ 0.8,\ 0.8, \\ &0.38 + 0.08\sqrt{3},\ 0.32 + 0.08\sqrt{3},\ 0.32 - 0.08\sqrt{3},\ldots \end{aligned} \tag{73}$$

The roots of the characteristic equation of the new sequence comprise ρ_k, $k=\overline{1,6}$ except that now there is no ρ_4.

4.2.2. WMA and Real-world Time Series

As discussed previously, the order of a real-world time series is infinite. But it has also been shown that SVD can be used for the identification of the order of a LRS contaminated by additive noise – if only this LRS does exist.

The optimization problem for short time series prediction is constructed in the following section.

4.2.3. Preprocessing

Given time series $\{x_j\}_{j=0}^{n}$ (this time series is not necessarily a LRS), let us set the order of the Hankel matrix m and the error level at $\varepsilon > 0$. Let us set the width of the observation window L and perform MA: $\{y_j\}_{j=L-1}^{n} = \left\{\frac{1}{L}\sum_{s=j-L+1}^{j} x_s\right\}_{j=L-1}^{n}$.

We thus construct the catalecticant Hankel matrix from $\{y_j\}_{j=L-1}^{n}$ (starting from y_{L-1}). Then we perform SVD of the Hankel matrix; SVD eigenvalues are denoted as $\{\sigma_k^2\}_{k=1}^{m}$. We compute the number of SVD eigenvalues greater than ε: $N_\varepsilon = \sum_{k=1}^{m}\delta_k$, where $\delta_k = \begin{cases} 1 \; if \;\; \sigma_k^2 \geq \varepsilon \\ 0 \; if \;\; \sigma_k^2 < \varepsilon \end{cases}$. We store MA weight coefficients $\left\{\frac{1}{L}\right\}_{j=1}^{L}$ and N_ε as the current best result.

4.2.4. The Optimization Strategy

The goal of the optimization procedure is to find such weight coefficients $\{w_j\}_{j=1}^{L}$ that the order of the WMA is the lowest possible: $\min\limits_{\{w_1,\ldots,w_L\}} N_\varepsilon$. Such an optimization problem has a trivial solution: $w_1 = \cdots = w_L = 0$. Additional constraints for the weight coefficients are required to make this a well-posed optimization problem. Natural requirements are set as follows:

$$\sum_{j=1}^{L} w_j = 1; \; w_j > 0 \text{ for all } j. \tag{74}$$

We should note that MA weight coefficients belong to the feasible set of the constrained optimization problem.

We find such weight coefficients of WMA which result in the minimum order of the LRS. Then we generate a vector of weight coefficients $\{w_j\}_{j=1}^{L}$ satisfying constraints (74) and perform WMA: $\{y_j\}_{j=0}^{+\infty} = \left\{\sum_{s=0}^{L-1} w_{L-s} x_{s+j}\right\}_{j=0}^{+\infty}$. We compute the

number of SVD eigenvalues of the Hankel matrix of the WMA sequence greater than ε : N_ε. If the value of N_ε is lower than the best stored value, we save the current vector of weight coefficients $\{w_j\}_{j=1}^{L}$ and N_ε as the best current arguments and the best current value of the target function. Otherwise, we execute the same iteration again.

The strategy for the generation of a sequence of weight coefficients $\{w_j\}_{j=1}^{L}$ is an intrinsic feature of the optimization algorithm – a wise selection of this strategy may guarantee an effective computational solution of the optimization problem (we should note that the defined target function maps $\mathbb{R}^n$ onto $\mathbb{N}_0$). However, neither deterministic strategies nor evolutionary approaches based on particle swarm optimization (PSO) or genetic algorithms (GA) can produce satisfactory results. This may be explained by the topology of the target function (a simple two-dimensional computational experiment at $L = 2$ is used for clarity).

Let us consider the chaotic Logistic map (Eq. (24)) at $r = 4$ and start from the initial condition $x_0 = 0.44$. Initially, constraints (74) are released, and it is only required that $0 \le w_j \le 1$; $j = 1,2$. N_ε is computed at the grid-points throughout the whole domain – the results are illustrated in Fig. 52a. It is clear that the global minimum is reached at $w_1 = w_2 = 0$.

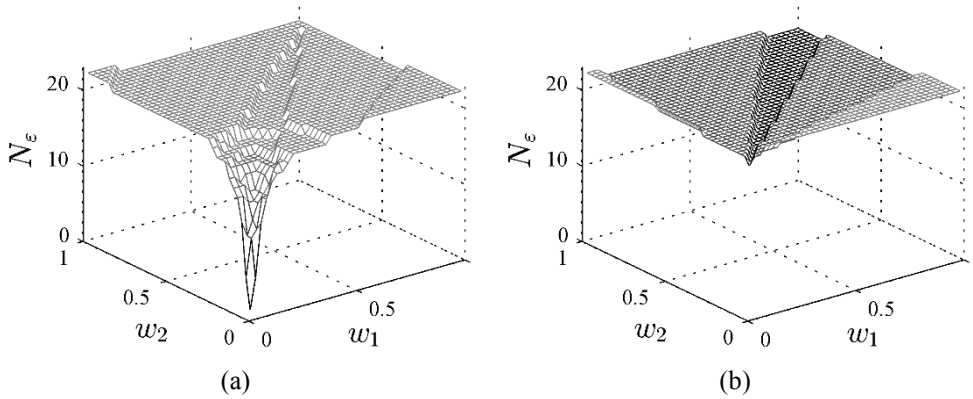

Fig. 53. The geometrical shape of the target function N_ε in respect to weight coefficients w_1 and w_2. The constraint $w_1 + w_2 = 1$ is released in part (a) and is in force (according to Eq. (75) in part (b)

We should note that the constraint $w_1 + w_2 = 1$ yields a feasible set which is geometrically represented as a line interval in the domain of Fig. 53a; the problem becomes a single variable optimization problem. In general, constraints (68) reduce the dimension of the optimization problem by one. However, the generation of a vector of the weight coefficients which does belong to the feasible set is not so straightforward if the dimension of the problem is higher than 2. For example, one could generate random values of w_1 and w_2 distributed uniformly in the interval

[0,1] – but $w_3 = 1 - w_1 - w_2$ does not always yield a feasible point in case of $L = 3$ (let us consider a situation when $w_1 = 0.9$ and $w_2 = 0.9$).

Therefore, the generation of numerical values of the weight coefficients $\{w_j\}_{j=1}^{L}$ is executed according to the following algorithm. First of all, a pre-selected search strategy algorithm is allowed to generate numbers $\{e_j\}_{j=1}^{L}$ with the only limitation $0 \le e_j \le 1$; $j = 1,\ldots,L$. Then, the weight coefficients are computed as follows:

$$w_j = \frac{e_j}{\sum_{k=1}^{L} e_k}; \; j = 1,\ldots,L. \tag{75}$$

Vector $\{e_j\}_{j=1}^{2}$ is allowed to span over the entire domain $[0,1]\times[0,1]$ in Fig. 53b. The resulting distribution of N_ε (Fig. 53b) clearly shows that the discontinuous surface of the values of the target function comprises relatively wide and flat zones (which is predetermined by the mapping $\mathbb{R}^n \to \mathbb{N}_0$). In other words, anti-gradient decent methods and even PSO or GA methods would fail to generate a sequence of points converging to a local minimum. Therefore, random Monte Carlo (MC) search strategy is selected for all further computational experiments.

4.2.5. Computational Experiments

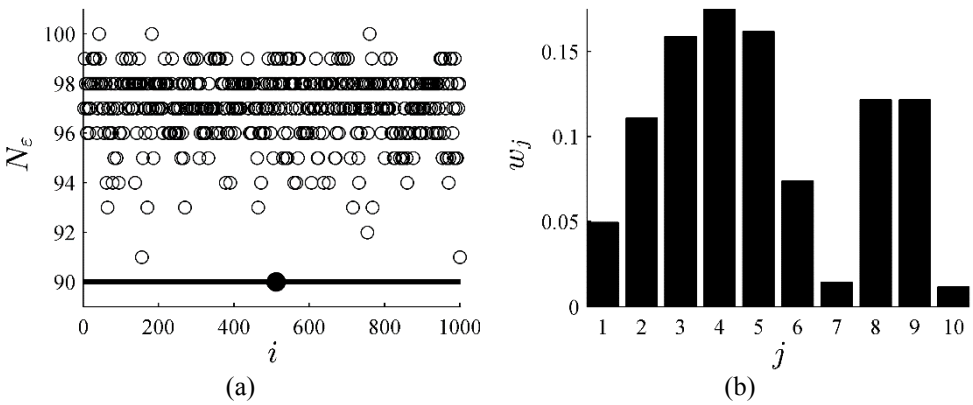

Fig. 54. A near optimal set of weight coefficients for the Gaussian noise; the width of the observation window is 10. 1000 MC trials are illustrated in part (a); the thick solid horizontal line denotes the result for the classical MA; the black dot shows the best result produced by random search. Part (b) illustrates the weight coefficients for the best result depicted as the black dot in part (a). Index i denotes an MC trial number; j is the weight coefficient index

Let us consider a random Gaussian noise time series with the zero mean and the standard deviation equal to 1. Let us take $L = 10$ and $\varepsilon = 0.1$. It is well-known that it is impossible to find the optimal embedding time delay vector for a random

noise sequence (Sauer et al., 1991) – it is hard to expect that WMA would produce better results compared to MA. As mentioned previously, MC techniques will be used for the generation of a vector of random weight coefficients according to (69). But, first of all, the pre-processing (MA) produces $N_\varepsilon = 89$ (this result is shown as a thin solid horizontal line in Fig. 54a). One thousand MC iterations are executed; the value of N_ε in each trial is visualized as an empty circle in Fig. 54a along the horizontal axis. It appears that 1000 MC trials cannot generate weight coefficients which would result in a lower value of N_ε than produced by MA. The weight coefficients resulting in the best N_ε are shown in Fig. 54b.

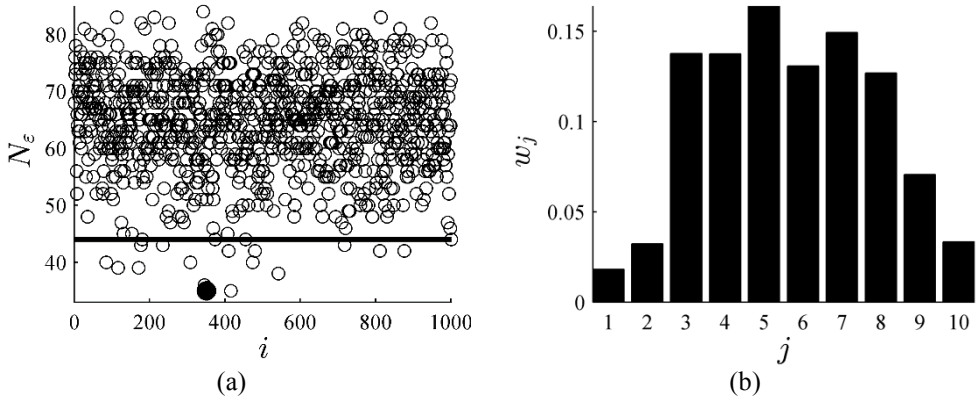

Fig. 55. A near-optimal set of weight coefficients for the synthetic time series contaminated with noise; the width of the observation window is 10. 1000 MC trials are illustrated in part (a); the thick solid horizontal line denotes the result for the classical MA; the black dot shows the best result produced by random search. Part (b) illustrates the weight coefficients for the best result depicted as the black dot in part (a)

Next, computational experiments with a synthetic sequence $x_j = \sin(j/10) + 0.01 \cdot rand_j$; $j = 0,1,\ldots$ are continued. Here $rand_j$ is a discrete normal Gaussian random variable $N(0,1)$ generated at the j-th step. Now, MA produces $N_\varepsilon = 43$. However, 1000 MC iterations manage to produce such weight coefficients which do result in a lower value of N_ε compared to MA (Fig. 55a). The best set of weight coefficients is illustrated in Fig. 55b.

4.3. Time Series Forecasting Based on the Algebraic WMA

4.3.1. The Forecasting Algorithm

As mentioned previously, MA techniques are often used as simple but effective time series forecasting tools. The ability to identify underlying algebraic relationships by varying the weight coefficients of WMA suggests an alternative approach for the time series prediction. The schematic diagram for such a WMA prediction technique is illustrated in Fig. 55.

Let x_0 be the value of the original sequence at the present time moment; the present and past values of the sequence are used to forecast x_1. The algorithm described in Section 4 is used to identify a set of near-optimal weight coefficients $\{w_j\}_{j=1}^{L}$; the weighted average $y_1 = \sum_{s=0}^{L-1} w_{L-s} x_{-s}$ is used as a direct estimate of x_1. We should note that the WMA forecasting becomes MA forecasting if only it appears that it is impossible to find a better set of weight coefficients than the MA coefficients (the preprocessing step in Section 4.1): $y_1 = \frac{1}{L}\sum_{s=0}^{L-1} x_{-s}$.

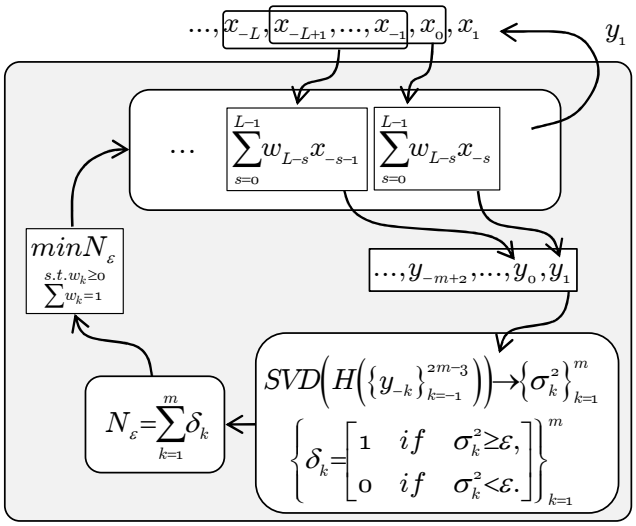

Fig. 56. The schematic diagram of AWMA prediction

The selection of parameter ε is considered in Section 4 – but the selection of the width of the observation window L has not been discussed yet. In fact, the strategy for the selection of L is straightforward. First of all, one needs to determine the optimal width of the observation window for MA prediction; the optimality criterion is the RMSE of MA prediction. Then, at each time step one should try to find such a set of weight coefficients which would result in a lower value of N_ε compared to the one produced by MA. One-step-forward WMA prediction is executed if the search was successful; the ordinary MA prediction is performed otherwise.

4.3.2. Computational Experiments

Quarterly percentage increase in the estimated resident population of Australia from September 1971 to June 1993 (also named as *erppc*) was chosen for computational experiments (the dataset is available online at the Time Series Data Library (Hyndman)).

Table 9. RMSE as a function of the observation window for MA prediction

L	2	3	4	5	6	7	8	9
RMSE	0.0749	0.0707	0.0689	0.0697	0.0709	0.0727	0.0739	0.0752

Table 9 shows RMSE for MA prediction at different values of the length of the observation window. The prediction was the most accurate with $L = 4$.

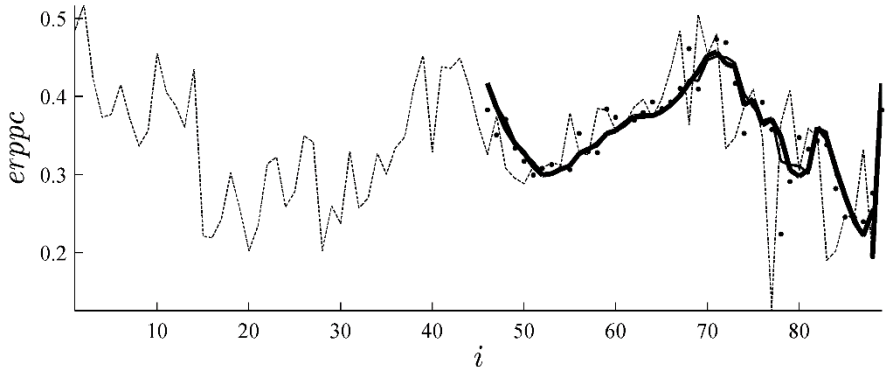

Fig. 57. The application of AWMA to *erppc* series in comparison to the standard moving average and ARIMA(1, 1, 2) at $L = 4$; $\varepsilon = 0.04$. The original data is plotted as the dotted line; MA(4) prediction is represented as the thin solid line; ARIMA(1, 1, 2) is shown with dots; AWMA is presented as the thick solid line

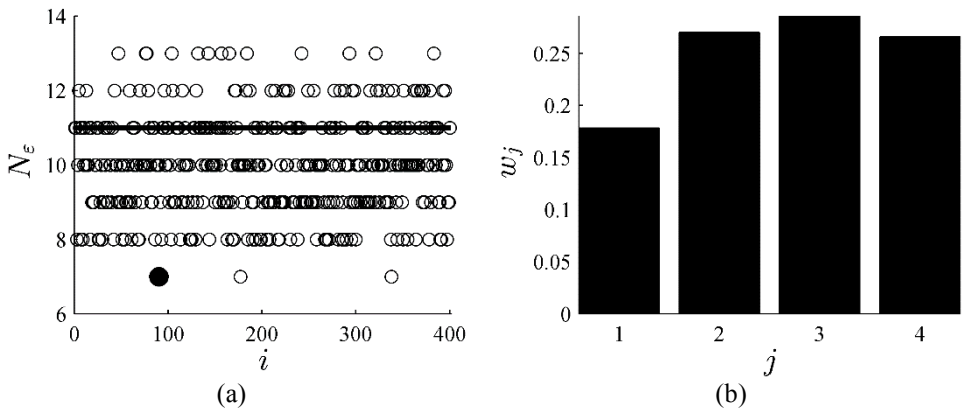

Fig. 58. A near-optimal set of weight coefficients for *erppc* at the first prediction step; $L = 4$. 400 MC trials are illustrated in part (a); the thick solid horizontal line denotes the result for the classical MA; the black dot shows the best result produced by random search. Part (b) illustrates the weight coefficients for the best result depicted as the black dot in part (a)

We should note that there exists a set of vectors of weight coefficients $\{w_j\}_{j=1}^{L}$ at the same optimal value of L. In order to minimize the prediction error as well as to minimize the algebraic complexity of the underlying skeleton sequence, one must fix a vector $\{w_j\}_{j=1}^{L}$ leading to the minimal prediction error. Not considering this

step reduces the algebraic complexity of the underlying skeleton sequence but does not guarantee the best prediction error.

AWMA results for the *erppc* series are shown in Fig. 57. Each prediction was generated by simulating 10000 sets of the weight coefficients for WMA and then minimizing the ranks of the underlying skeleton sequences. A near-optimal set of weight coefficients for *erppc* at the first prediction step is depicted in Fig. 58.

Results were compared to $\mathrm{MA}(4)$ and $\mathrm{ARIMA}(p,d,q)$. By testing various parameter values, the optimal time series model $\mathrm{ARIMA}(1,1,2)$ was obtained. The model resulted in MAPE of 0.1770. Prediction errors for MA and AMWA are 0.1774 and 0.1678 respectively. It should be noted that AWMA also outperforms the naïve prediction for this particular example. Here MAPE is provided instead of RMSE in order to better illustrate the relative differences between different error values.

4.4. Applications of *H*-ranks in Real World Magnetometer Data

Application of the algebraic decomposition of a sequence for real world data could be used with aims other than prediction of the time series. Algebraic decomposition and extrapolation of magnetic field intensity is discussed below. This solution could be employed for the reconstruction of short term signal losses as it preserves the underlying algebraic structure of the data.

4.4.1. Magnetometer Data Formats of the Intensity of a Magnetic Field

The data considered in this chapter is obtained from the magnetometer installed on the territory of the LUHS Institute of Animal Science in Baisogala (Lithuania). Table 10 shows the structure of the data which is being hourly recorded into a binary file in the form of a table.

Table 10. The data structure of magnetometer recordings

No.	Magnetic field intensity				Timestamp	Temp., C
	N/S direction	E/W direction	Vertical direction	Satellite data		
1	-134430	-83725	-	-271	1337915034	20
2	-12863	38269	-	-278	1337915034	21
...	...	...	...	...	...	...

The intensity of a local magnetic field is registered at a sampling rate of 130Hz. It should be mentioned that the current time value is stored as the whole number of seconds having elapsed since a particular moment of time in the past (it depends on the operating system) in a computer. As a result, each 130 timestamps are recorded as the same number representing a particular second. Thus the first step in processing the magnetometer data is to interpolate these values in order to obtain meaningful timestamps. This procedure is also necessary if synchronization with other signals is considered.

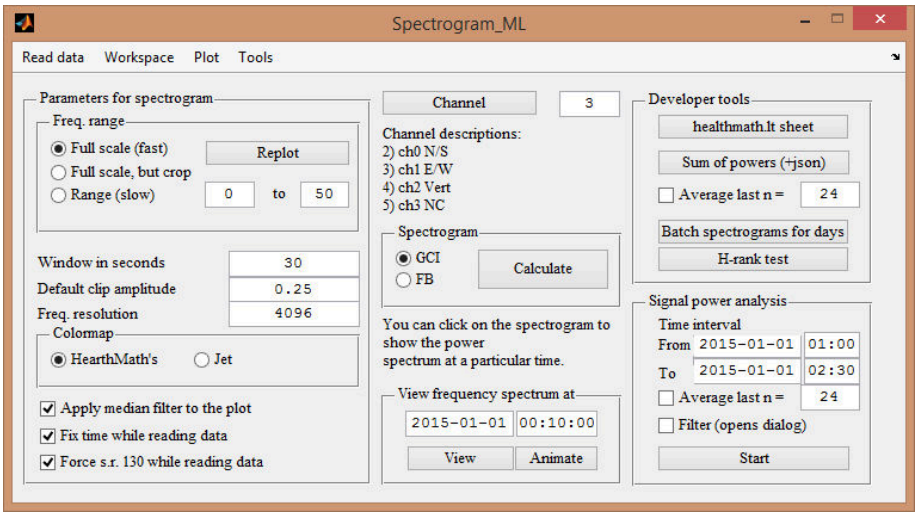

Fig. 59. Software created for extracting the magnetic field data, calculating the spectrograms, the power of a signal and for filtering the signal of the magnetic field intensity

The huge amount of raw data leads to the necessity of creating the software in order to process it. Matlab and its graphical user interface tool (guide) was used for this purpose. The main interface of the developed software is shown in Fig. 59.

4.4.2. Algebraic Reconstruction of the Magnetic Field Intensity Based on *H*-ranks

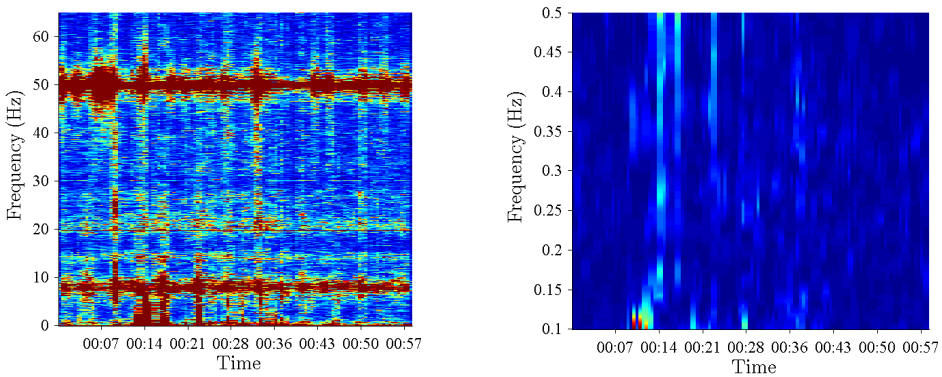

Fig. 60. Spectrograms for the time period of 1h on 21st of December 2014. (a) frequencies in $[0;65]$, (b) frequencies in $[0{,}1;0{,}5]$

By default Matlab's function *spectrogram* finds power spectral density in the frequency range 0 to the half of the sampling rate. Thus the frequency scale has the upper limit of 65 Hz provided the data sampling rate is 130 Hz. Fig. 60 depicts the spectrogram for a time period of 1h on the 21st of December, 2014. A noticeable peak at 50 Hz is due to the frequency of the Lithuanian power grid. The first of the Schumann resonances appear as peaks at frequencies around 7.83, 14.3 and 20.8 Hz.

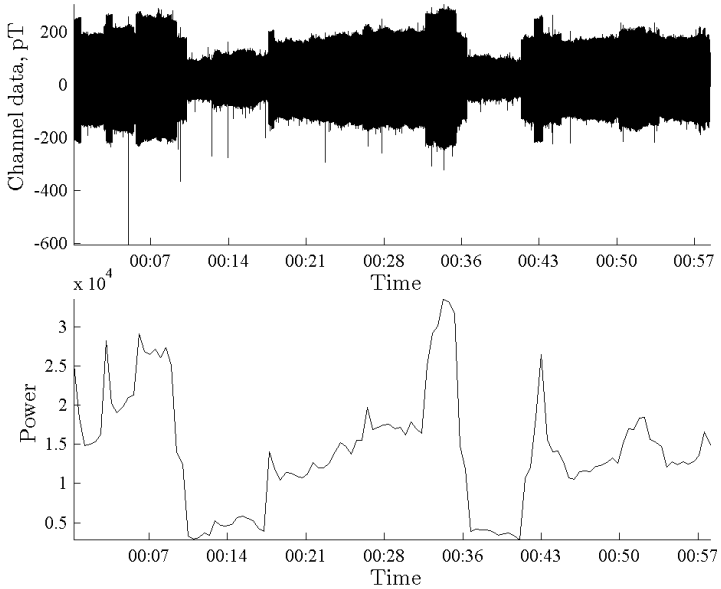

Fig. 61. Variation of the magnetic field and its power (classical squared RMS approach) for the time period of 1h on the 21st of December, 2014

Project partners from LSMU suggested the frequency intervals $[0;0,1]$, $[0,1;0,5]$, $[0,5;1]$, $[1;7]$ and $[7;50]$ to be considered according to the nature of particular human physiological processes. 3rd order Butterworth filter was used to analyze the signals.

All the data from the magnetometer located in Lithuania was analyzed during the research. Spectrograms were formed considering various resolutions in both time and frequency axes. The results are very similar in northerly-southerly and easterly-westernly directions. A historical data overview in the form of spectrograms and power charts was uploaded to www.healthmath.lt where project members can analyze them at any time.

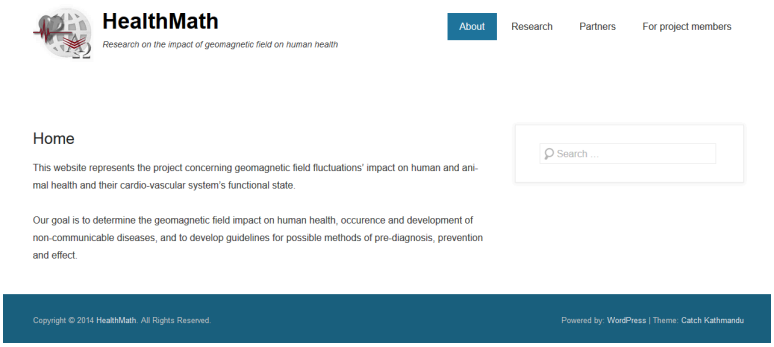

Fig. 62. The title page of www.healthmath.lt

Matlab's function *spectrogram* can calculate a spectrogram in a predefined interval of frequencies. It is achieved by passing the endpoints of the intervals to one of the parameters. The calculation time is considerably longer compared to the default frequency range. On the contrary, if one needs to evaluate the interval $[0;0,1]$, the results may be obtained faster by passing the endpoints of the interval. This is due to the fact that otherwise the interval must be highly discretized in order to get sufficient data from the cropped spectrogram. For such wider intervals as $[7;50]$, it is more efficient to firstly calculate the default spectrogram and then crop it to the interval. The software allows the user to choose one of the two methods described above.

The domain name www.healthmath.lt was purchased while working on the project. Also a website was created (Fig. 62). It acts as a platform for sharing magnetometer data and research information among the partners of the project. Historical data and special software are available there under a password. Additional cloud storages are used because the data of the year 2014 alone takes about 19 GB. The data is in zipped mat files in order to be ready for use with the developed software. Each file contains magnetic field intensities over a one-hour period. The software also features a batch conversion feature for dealing with the original zipped binary files which are initially recorded by the magnetometer.

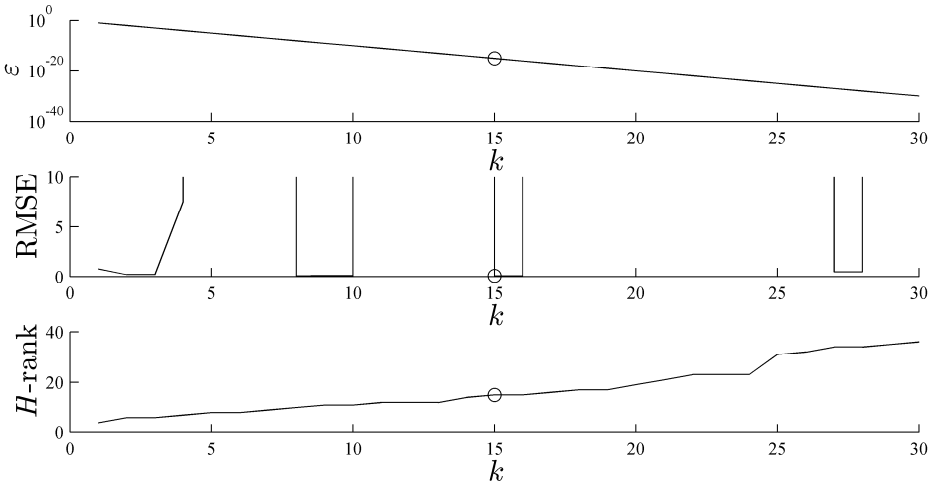

Fig. 63. The process of finding the optimal rank of the series representing the magnetic field intensity. Part (a) shows the variation of the value for machine *epsilon*. The corresponding RMSE between the real signal and the extrapolated result as well as the resulting *H*-rank are shown respectively in (b) and (c)

The magnetometer data of a 1-hour period starting from 12:00:02 recorded on January 01, 2016, is considered in order to illustrate the practical application of the algebraic reconstruction of a real world sequence.

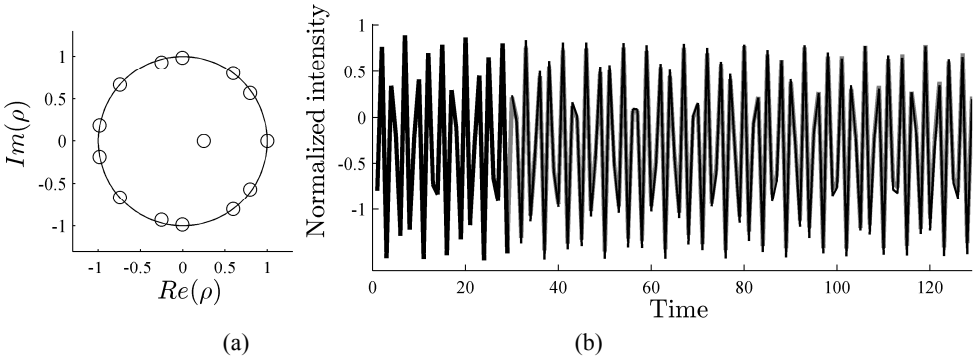

Fig. 64. Algebraic extrapolation of the magnetic field intensity. The distribution of roots is shown in (a); transient processes (thin gray solid lines), base fragments (thick black solid lines) and extrapolated sequences (thin black lines) are shown in (b)

The optimal *H*-rank for the series is 15 (Fig. 63(a)); the corresponding value for machine *epsilon* is 10^{-15}, and the best RMSE result was 0.0585.

The obtained optimal *H*-rank value was used to extrapolate the magnetic field intensity (Fig. 64). The data series must be normalized before the procedure. Otherwise, the results would be inadequate due to the buildup of computation errors.

By performing a number of computational experiments it was noted that the quality of the extrapolation for the magnetic field intensity is comparably higher than the one for discrete nonlinear maps. Fig. 65 shows that an extrapolated sequence still follows the pattern of the original time series after 500 iterations. We should note that 130 iterations correspond to a time period of 1 second.

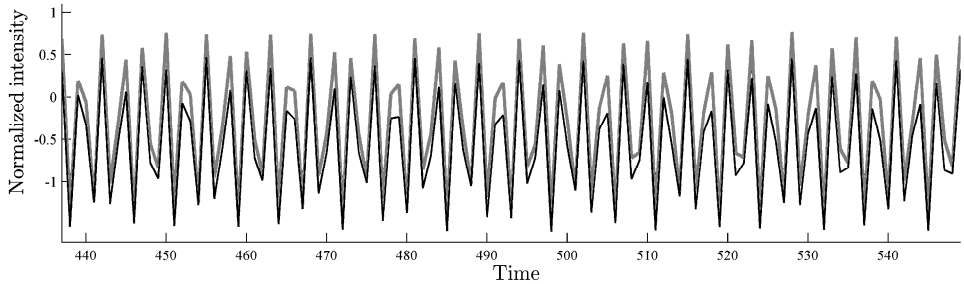

Fig. 65. Algebraic extrapolation of the magnetic field intensity. Transient processes are plotted as thin gray solid lines while extrapolated sequences are shown as the thin black lines

4.5. Conclusions

The algebraic technique based on Hankel matrices and the rank of a partial solution is proposed for the investigation of the onset of chaos in discrete nonlinear dynamical systems. The distribution of roots of the modified characteristic equation describes a measure of the complexity of the solution and is used for the characterization of the system's dynamics. The developed technique is applicable for steady-state attractors as well as for transient solutions.

The evolution of the distribution of roots as the system approaches to the chaotic regime reveals interesting properties of the system's dynamics. The inability of a deterministic algebraic technique to decompose a chaotic solution is represented by a computational blow-up of the rank and the stochastic distribution of characteristic roots on the complex plane. Such amplification of the algebraic complexity at the onset of chaos seems to be a universal feature of chaotic nonlinear systems and is demonstrated for a discrete dynamical system: the Logistic map.

An effective time series forecasting technique based on algebraic weighted moving average is proposed in this chapter. The weight coefficients are selected in such a way that the algebraic complexity of the resulting averaged time series is minimal. The complex optimization problem is solved by employing the random MC search strategy. The functionality and feasibility of the proposed short-time series forecasting technique is demonstrated by computational experiments with the real world time series.

The size of the algebraic model is automatically selected by minimizing the prediction errors produced by the classical MA for different observation windows. An alternative (but a much more time consuming one) approach would be to vary the observation window of the algebraic model independently of the MA results. Such an approach would probably result in even more precise predictions.

The algebraic decomposition of a sequence was applied for the real world magnetometer data. Despite the magnetic field intensity being a real world sequence (which does not have a rank), the decomposition yielded interpretable results. The extrapolated sequence follows the pattern of the original data series for more than 500 forward iterations. The practical significance of this result could be the possibility to use algebraic techniques in reconstructing short term signal losses.

FINAL CONCLUSIONS

1. It is demonstrated that *H*-rank computations produce interpretable results for error values smaller than the machine *epsilon*. A computational framework is developed for efficient construction of patterns of *H*-ranks for nonlinear dynamical systems.

2. It is shown that patterns of *H*-ranks can be used for the identification of the manifolds of non-asymptotic convergence in nonlinear dynamical systems.

3. The information provided by the patterns of *H*-ranks is proved to be useful for the manipulation or control of nonlinear dynamical systems. Patterns of *H*-ranks are used to identify pseudo stable structures of completely invertible dynamical systems. Manifolds in patterns of *H*-ranks enable to construct new control algorithms for transient processes in nonlinear systems.

4. The algebraic technique based on Hankel matrices is proposed for the investigation of the onset of chaos in discrete nonlinear dynamical systems. The distribution of roots of the modified characteristic equation describes a measure of the complexity of the solution and in turn characterizes the system's dynamics.

5. The proposed short-time series forecasting technique proved to be better in terms of MAPE of the prediction compared to the classical moving average forecasting technique. The proposed technique is based on the concept of the pseudorank of a predicted time series.

6. *H*-ranks are used for the algebraic analysis of the real world magnetometer data and the reconstruction of short term signal losses.

REFERENCES

1. AISSA, B., D. NADIR and M. AMMAR. An approach using stream cipher algorithm for image encryption and decryption. In *15th International Conference on Sciences and Techniques of Automatic Control and Computer Engineering (STA).* 2014, p. 498-503.
2. AITKEN, A. C. and A. C. AITKEN. *Determinants and matrices*. Oliver and Boyd Edinburgh and London, 1956.
3. AKHMET, M. and M. FEN. Chaotic period-doubling and OGY control for the forced Duffing equation. *Communications in Nonlinear Science and Numerical Simulation*, 2012, 17(4), 1929-1946.
4. AKHTAR, N. and S. N. KHAN. Optimization of SVD over Graphic Processor. In *International Conference on Information Systems and Computer Networks (ISCON).* IEEE, 2013, p. 177-179.
5. ALONSO, P., D. ARGUELLES, J. RANILLA and A. M. VIDAL. A multicore solution to Block-Toeplitz linear systems of equations. *The Journal of Supercomputing*, 2013, 65(3), 999-1009.
6. ALONSO, P., F. ARGUESO, R. CORTINA, J. RANILLA, et al. Non-linear parallel solver for detecting point sources in CMB maps using Bayesian techniques. *Journal of Mathematical Chemistry*, 2013, 51(4), 1153-1163.
7. ARNOLD, V. I. Small denominators. I. Mapping the circle onto itself. *Izvestiya Rossiiskoi Akademii Nauk. Seriya Matematicheskaya*, 1961, 25(1), 21-86.
8. AURENTZ, J. L., R. VANDEBRIL and D. S. WATKINS. Fast computation of the zeros of a polynomial via factorization of the companion matrix. *SIAM Journal on Scientific Computing*, 2013, 35(1), A255-A269.
9. BAHAR, S. Chaotic attractors generated by iterated function systems:'Harmonic decompositions' and the onset of chaos. *Chaos, Solitons & Fractals*, 1997, 8(3), 303-312.
10. BAYLIS, C. and R. J. MARKS. Small perturbation harmonic coupling in nonlinear periodicity preservation circuits. *IEEE Transactions on Circuits and Systems I: Regular Papers*, 2012, 59(12), 3034-3045. ISSN 1549-8328.
11. BHATTACHARJEE, S. and K. KUMAR. Parametric instability in the Watt governor with periodic loading. *European Journal of Physics*, 2014, 35(3), 035006. ISSN 0143-0807.
12. BOYLAND, P. L. Bifurcations of circle maps: Arnol'd tongues, bistability and rotation intervals. *Communications in Mathematical Physics*, 1986, 106(3), 353-381.
13. BORDYUGOV, G., A. E. GRANADA and H. HERZEL. How coupling determines the entrainment of circadian clocks. *The European Physical Journal B-Condensed Matter and Complex Systems*, 2011, 82(3), 227-234.
14. BRESTEN, C. L. and J.-H. JUNG. A study on the numerical convergence of the discrete logistic map. *Communications in Nonlinear Science and Numerical Simulation*, 2009, 14(7), 3076-3088.
15. BROER, H. W., H. M. OSINGA and G. VEGTER. Algorithms for computing normally hyperbolic invariant manifolds. *Journal of Applied Mathematics and Physics*, May, 1997, 48(3), 480-524.

16. CASTALDO, A. M., R. C. WHALEY and S. SAMUEL. Scaling LAPACK panel operations using parallel cache assignment. *ACM Transactions on Mathematical Software (TOMS)*, 2013, 39(4), 22.
17. CASTELLI, R. and J.-P. LESSARD. Rigorous numerics in Floquet theory: computing stable and unstable bundles of periodic orbits. *SIAM Journal on Applied Dynamical Systems*, 2013, 12(1), 204-245.
18. CHEN, K.-Y. Combining linear and nonlinear model in forecasting tourism demand. *Expert Systems with Applications*, 2011, 38(8), 10368-10376.
19. CHIARELLA, C. The cobweb model: Its instability and the onset of chaos. *Economic modelling*, 1988, 5(4), 377-384.
20. CHICONE, C. C. *Ordinary differential equations with applications*. Springer, 1999.
21. CHIRIKOV, B. V. A universal instability of many-dimensional oscillator systems. *Physics Reports*, 1979, 52(5), 263-379.
22. CHOI, S.-Y. and E. K. LEE. Scaling behavior at the onset of chaos in the logistic map driven by colored noise. *Physics Letters A*, 1995, 205(2), 173-178.
23. CHRISTIANSEN, F. and H. H. RUGH. Computing Lyapunov spectra with continuous Gram-Schmidt orthonormalization. *Nonlinearity*, 1997, 10(5), 1063.
24. CORADDU, M., M. LISSIA and R. TONELLI. Statistical descriptions of nonlinear systems at the onset of chaos. *Physica A: Statistical Mechanics and its Applications*, 2006, 365(1), 252-257.
25. DE JONG, L. S. Numerical aspects of recursive realization algorithms. *SIAM Journal on Control and optimization*, 1978, 16(4), 646-659.
26. DE MOURA, F., U. TIRNAKLI and M. LYRA. Convergence to the critical attractor of dissipative maps: Log-periodic oscillations, fractality, and nonextensivity. *Physical Review E*, 2000, 62(5), 6361.
27. DEADMAN, E., N. J. HIGHAM and R. RALHA. Blocked Schur Algorithms for Computing the Matrix Square Root. *Lecture Notes in Computer Science*, 2013, 7782, 171-182.
28. DELLNITZ, M. and A. HOHMANN. A subdivision algorithm for the computation of unstable manifolds and global attractors. *Numerische Mathematik*, 1997, 75(3), 293-317.
29. DONFACK, S., S. TOMOV and J. DONGARRA. Dynamically balanced synchronization-avoiding LU factorization with multicore and GPUs. In *Parallel & Distributed Processing Symposium Workshops (IPDPSW), 2014 IEEE International.* 2014, p. 958-965.
30. DONG-XIAO, N., S. HUI-FENG and D. W. DESHENG. Short-term load forecasting using bayesian neural networks learned by Hybrid Monte Carlo algorithm. *Applied Soft Computing*, 2012, 12(6), 1822-1827.
31. DUBICKAS, A. and A. NOVIKAS. Linear recurrence sequences without zeros. *Czechoslovak Mathematical Journal*, 2014, 64(3), 857-865.
32. EASTON, J. F., C. R. STEPHENS and M. ANGELOVA. Risk factors and prediction of very short term versus short/intermediate term post-stroke mortality: A data mining approach. *Computers in biology and medicine*, 2014, 54, 199-210.

33. ESCALONA, J., J. V. JOSÉ and P. TIESINGA. Entrainment, Arnold tongues, and duality in a periodically driven integrate-and-fire model. *Neurocomputing*, 2002, 44, 91-96.

34. EVERSON, R. M. Chaotic dynamics of a bouncing ball. *Physica D: Nonlinear Phenomena*, April, 1986, 19(3), 355-383.

35. FAZEL, M., T. K. PONG, D. SUN and P. TSENG. Hankel matrix rank minimization with applications to system identification and realization. *SIAM Journal on Matrix Analysis and Applications*, 2013, 34(3), 946-977.

36. FEIGENBAUM, M. J. Some formalism and predictions of the period-doubling onset of chaos. *North-Holland Mathematics Studies*, 1982, 61, 379-394.

37. FENG, X., H. JIN, R. ZHENG and L. ZHU. Parallel singular value decomposition on heterogeneous multi-core and multi-GPU platforms. In *2014 Ninth International Conference on Digital Information Management (ICDIM).* 2014, p. 45-50.

38. FERMI, E. On the Origin of the Cosmic Radiation. *Physical Review*, April, 1949, 75(8), 1169-1174.

39. FERREIRA, B. B., M. A. SAVI and A. S. DE PAULA. Chaos control applied to cardiac rhythms represented by ECG signals. *Physica Scripta*, 2014, 89(10), 105203.

40. FERRELL, J. E., T. Y.-C. TSAI and Q. YANG. Modeling the cell cycle: why do certain circuits oscillate? *Cell*, 2011, 144(6), 874-885.

41. FIRMINO, P. R. A., P. S. DE MATTOS NETO and T. A. FERREIRA. Correcting and combining time series forecasters. *Neural networks*, 2014, 50, 1-11.

42. FOSTER, B., S. MAHADEVAN and R. WANG. A GPU-based approximate SVD algorithm. In *Parallel Processing and Applied Mathematics.* Springer, 2012, p. 569-578.

43. FRISON, G. and J. B. JORGENSEN. Parallel Implementation of Riccati Recursion for Solving Linear-Quadratic Control Problems. In *18th Nordic Process Control Workshop.* 2013.

44. GANDHI, B. K., A. C. SEKHAR and S. SRILAKSHMI. Cryptographic scheme for digital signals using finite state machine. *International journal of computer applications (September 2011)*, 2011.

45. GATES, M., A. HAIDAR and J. DONGARRA. Accelerating computation of eigenvectors in the nonsymmetric eigenvalue problem. *Lecture Notes in Computer Science*, 2015, 8969, 182-191.

46. GÉRARD, C. and A. GOLDBETER. The cell cycle is a limit cycle. *Mathematical Modelling of Natural Phenomena*, 2012, 7(06), 126-166.

47. GERARDO DE LA FRAGA, L. A very fast procedure to calculate the smallest singular value. In *Eighth International Conference on Advances in Pattern Recognition (ICAPR).* 2015, p. 1-4.

48. GIESL, P. Necessary conditions for a limit cycle and its basin of attraction. *Nonlinear Analysis: Theory, Methods & Applications*, 2004, 56(5), 643-677.

49. GLASS, L., M. R. GUEVARA, A. SHRIER and R. PEREZ. Bifurcation and chaos in a periodically stimulated cardiac oscillator. *Physica D: Nonlinear Phenomena*, 1983, 7(1), 89-101.

50. GLASS, L. and A. SHRIER. Functional Characterization of Oscillatory and Excitable Media. *Bulletin of mathematical biology*, 2014, 1-14. ISSN 0092-8240.

51. GONZÁLEZ-MIRANDA, J. M. Nonlinear dynamics of the membrane potential of a bursting pacemaker cell. *Chaos: An Interdisciplinary Journal of Nonlinear Science*, 2012, 22(1), 013123.

52. GOODMAN, R. H. and J. K. WRÓBEL. High-order bisection method for computing invariant manifolds of two-dimensional maps. *International Journal of Bifurcation and Chaos*, July, 2011, 21(7), 2017.

53. GRAY, A., I. STEWART and A. TENESA. Advanced complex trait analysis. *Bioinformatics*, 2012, 28(23), 3134-3136.

54. GRITLI, H., S. BELGHITH and N. KHRAIEF. OGY-based control of chaos in semi-passive dynamic walking of a torso-driven biped robot. *Nonlinear Dynamics*, 2014, 79(2), 1363-1384.

55. GUCKENHEIMER, J. and P. J. HOLMES. *Nonlinear oscillations, dynamical systems, and bifurcations of vector fields*. Berlin: Springer, 1983.

56. GUNTA, C., S. N. KHAN, K. SAHA and D. P. PAU. Acceleration of SVD routines in LAPACK. In *EUROCON, 2013 IEEE.* 2013, p. 1733-1737.

57. GUO, Y. and A. C. J. LUO. Analytical Predication of Complex Motion of a Ball in a Periodically Shaken Horizontal Impact Pair. *Journal of Computational and Nonlinear Dynamics*, December, 2011, 7(2), 21001-21009.

58. GUSTAVSON, F. G., J. R. HERRERO and E. MORANCHO. A square block format for symmetric band matrices. In *Parallel Processing and Applied Mathematics.* Springer, 2014, p. 683-689.

59. GUSTAVSON, F. G., J. WAŚNIEWSKI, J. J. DONGARRA, J. E. R. HERRERO, et al. Level-3 Cholesky factorization routines improve performance of many Cholesky algorithms. *ACM Transactions on Mathematical Software (TOMS)*, 2013, 39(2), 9.

60. GUSTAVSON, F. G., J. WAŚNIEWSKI and J. R. HERRERO. New level-3 BLAS kernels for cholesky factorization. In *Parallel Processing and Applied Mathematics.* Springer, 2012, p. 60-69.

61. HABIB, S. and R. D. RYNE. Symplectic Calculation of Lyapunov Exponents. *Phys. Rev. Lett.*, Jan, 1995, 74, 70-73.

62. HALE, J. K. and N. STERNBERG. Onset of chaos in differential delay equations. *Journal of Computational Physics*, 1988, 77(1), 221-239.

63. HILBORN, R. C. *Chaos and non-linear dynamics*. King's Lynn, Norfolk: Oxford University Press, 2000.

64. HYNDMAN, R. J. *Time Series Data Library*. Available from Internet: http://data.is/TSDLdemo. Accessed on 2012 01 16.

65. HO, B. and R. E. KÁLMÁN. Editorial: Effective construction of linear state-variable models from input/output functions. *at-Automatisierungstechnik*, 1966, 14(1-12), 545-548.

66. HOBSON, D. An efficient method for computing invariant manifolds for planar maps. *Journal of Computational Physics*, January, 1993, 104(1), 14-22.

67. HOLMES, P. J. The dynamics of repeated impacts with a sinusoidally vibrating table. *Journal of Sound and Vibration*, 1982, 84(2), 173-189.

68. HOLT, C. C. Forecasting seasonals and trends by exponentially weighted moving averages. *International Journal of Forecasting*, 2004, 20(1), 5-10.

69. HONGLER, M.-O., P. CARTIER and P. FLURY. Numerical study of a model of vibro-transporter. *Physics Letters A*, February, 1989, 135(2), 106-112.

70. HONGLER, M. O. and J. FIGOUR. Periodic versus chaotic dynamics in vibratory feeders. *Helvetica Physica Acta*, 1989, 62(1), 68-81.

71. HORTON, M., S. TOMOV and J. DONGARRA. A class of hybrid lapack algorithms for multicore and gpu architectures. In *Application Accelerators in High-Performance Computing (SAAHPC), 2011 Symposium on.* 2011, p. 150-158.

72. HUTT, A. Additive noise may change the stability of nonlinear systems. *EPL*, October, 2008, 84(3), 34003-34008.

73. JAFARZADEH, S., C. LASCU and M. S. FADALI. State estimation of induction motor drives using the unscented Kalman filter. *Industrial Electronics, IEEE Transactions on*, 2012, 59(11), 4207-4216.

74. JENSEN, M. H. Multifractal scaling structure at the onset of chaos: Theory and experiment. *Nuclear Physics B-Proceedings Supplements*, 1987, 2, 487-495.

75. JENSEN, M. H., P. BAK and T. BOHR. Complete devil's staircase, fractal dimension, and universality of mode-locking structure in the circle map. *Physical review letters*, 1983, 50(21), 1637.

76. JENSEN, M. H. P. G., P. BAK and T. BOHR. Transition to chaos by interaction of resonances in dissipative systems. I. Circle maps. *Physical Review A*, 1984, 30(4), 1960.

77. JI, Q. and Y. LU. Bifurcations and Continuous Transitions in a Nonlinear Model of Intracellular Calcium Oscillations. *International Journal of Bifurcation and Chaos*, 2013, 23(02).

78. JIA, C., L. WEI, H. WANG and J. YANG. Study of track irregularity time series calibration and variation pattern at unit section. *Computational intelligence and neuroscience*, 2014, 2014.

79. JIN, Y. and H. HU. Stabilization of traffic flow in optimal velocity model via delayed-feedback control. *Communications in Nonlinear Science and Numerical Simulation*, 2013, 18(4), 1027-1034.

80. JOSEPH, S. K., P. M. INES and M. A. F. SANJUAN. Effect of the phase on the dynamics of a perturbed bouncing ball system. *Communications in Nonlinear Science and Numerical Simulation*, August, 2012, 17(8), 3279-3286.

81. KAAGSTROM, B., D. KRESSNER and M. SHAO. On aggressive early deflation in parallel variants of the QR algorithm. In *Applied Parallel and Scientific Computing.* Springer, 2012, p. 1-10.

82. KAHAN, W. IEEE standard 754 for binary floating-point arithmetic. *Lecture Notes on the Status of IEEE*, 1996, 754(94720-1776), 11.

83. KOSTELICH, E. J., J. A. YORKE and Y. ZHIPING. Plotting stable manifolds: error estimates and noninvertible maps. *Physica D: Nonlinear Phenomena*, June, 1996, 93(3-4), 210-222.

84. KOWALIK, Z. J., M. FRANASZEK and P. PIERANSKI. Self-reanimating chaos in the bouncing-ball system. *Physical Review A*, May, 1988, 37(10), 4016-4022.

85. KRAUSKOPF, B. and H. OSINGA. Growing 1D and quasi-2D unstable manifolds of maps. *Journal of Computational Physics*, October, 1998, 146(1), 404-419.

86. KRENTS, A. A., D. A. ANCHIKOV, N. E. MOLEVICH and A. V. PAHOMOV. Spiral waves in large aperture laser model. In *Laser Optics.* IEEE, 2014, p. 1-1.

87. KURAKIN, V. Linear complexity of polinear sequences. *Discrete Applied Mathematics*, 2001, 11(1), 1-51.

88. KURZAK, J., P. LUSZCZEK, M. FAVERGE and J. DONGARRA. Programming the LU Factorization for a Multicore System with Accelerators. In *High Performance Computing for Computational Science-VECPAR 2012.* Springer, 2013, p. 28-35.

89. KUZNETSOV, A., S. KUZNETSOV and I. SATAEV. A variety of period-doubling universality classes in multi-parameter analysis of transition to chaos. *Physica D: Nonlinear Phenomena*, 1997, 109(1), 91-112.

90. KUZNETSOV, S. V. An approach of the QR factorization for tall-and-skinny matrices on multicore platforms. In *Applied Parallel and Scientific Computing.* Springer, 2013, p. 235-249.

91. LAN, Y. Cycle expansions: From maps to turbulence. *Communications in Nonlinear Science and Numerical Simulation*, 2010, 15(3), 502-526.

92. LANDAUSKAS, M., J. RAGULSKIENĖ and M. RAGULSKIS. H-rank as a control tool for discrete dynamical systems. In *AIP Conference Proceedings.* 2012, vol. 1479, p. 2098.

93. LANDAUSKAS, M. and M. RAGULSKIS. Clocking convergence to a stable limit cycle of a periodically driven nonlinear pendulum. *Chaos*, 2012, 22(3), 1054-1500.

94. LANDAUSKAS, M. and M. RAGULSKIS. Clocking convergence to Arnold tongues - the H-rank approach. In *AIP Conference Proceedings.* 2013, vol. 1558, p. 2457-2460.

95. LANDAUSKAS, M. and M. RAGULSKIS. A pseudo-stable structure in a completely invertible bouncer system. *Nonlinear Dynamics*, 2014, 78(3), 1629-1643.

96. LEE, W. T. and H. J. YEOM. A study of baseline noise elimination of heart sounds using Kalman filter. In *Computer Applications for Graphics, Grid Computing, and Industrial Environment.* Springer, 2012, p. 285-290.

97. LI, F., C. CHONG, J. YANG, P. G. KEVREKIDIS, et al. Wave transmission in time-and space-variant helicoidal phononic crystals. *Physical Review E*, 2014, 90(5), 053201.

98. LICHTENBERG, A. J., M. A. LIEBERMAN and R. H. COHEN. Fermi acceleration revisited. *Physica D: Nonlinear Phenomena*, September, 1980, 1(3), 291-305.

99. LIEBERMAN, M. A. and A. J. LICHTENBERG. Stochastic and Adiabatic Behavior of Particles Accelerated by Periodic Forces. *Phys. Rev. A*, April, 1972, 5(4), 1852-1866.

100. LIN, J., W.-Z. GAO, Y.-Z. SUN, L. CHENG, et al. Fast simulation approaches for power fluctuation model of wind farm based on frequency domain. In *Power Electronics and Machines in Wind Applications (PEMWA), 2012 IEEE.* 2012, p. 1-7.

101. LINAGE, G., F. MONTOYA, A. SARMIENTO, K. SHOWALTER, et al. Fibonacci order in the period-doubling cascade to chaos. *Physics Letters A*, 2006, 359(6), 638-639.

102. LTAIEF, H., P. LUSZCZEK and J. DONGARRA. Profiling high performance dense linear algebra algorithms on multicore architectures for power and energy efficiency. *Computer Science-Research and Development*, 2012, 27(4), 277-287.

103. LUO, A. C. J. and Y. GUO. *Vibro-impact Dynamics*. Wiley, 2013.

104. LUO, A. C. J. and R. P. S. HAN. The dynamics of a bouncing ball with a sinusoidally vibrating table revisited. *Nonlinear Dynamics*, 1996, 10(1), 1-18.

105. MA, R., S. J. HU and H. H. XU. Very Short-Term Wind Speed Prediction of a Wind Farm Based on Artificial Neural Network. In *Advanced Materials Research*. 2013, vol. 608, p. 677-682.

106. MA, Z., S. AHUJA and C. W. ROWLEY. Reduced-order models for control of fluids using the eigensystem realization algorithm. *Theoretical and Computational Fluid Dynamics*, 2011, 25(1-4), 233-247. ISSN 0935-4964.

107. MAFFEZZONI, P., Z. ZHANG and L. DANIEL. A study of deterministic jitter in crystal oscillators. *Circuits and Systems I: Regular Papers, IEEE Transactions on*, 2014, 61(4), 1044-1054.

108. MANIKANDAN, M. S. and K. SOMAN. A novel method for detecting R-peaks in electrocardiogram (ECG) signal. *Biomedical Signal Processing and Control*, 2012, 7(2), 118-128.

109. MCGUINNESS, M., Y. HONG, D. GALLETLY and P. LARSEN. Arnold tongues in human cardiorespiratory systems. *Chaos: An Interdisciplinary Journal of Nonlinear Science*, 2004, 14(1), 1-6.

110. MITARAI, N., U. ALON and M. H. JENSEN. Entrainment of noise-induced and limit cycle oscillators under weak noise. *Chaos: An Interdisciplinary Journal of Nonlinear Science*, 2013, 23(2), 023125.

111. MOCENNI, C., A. FACCHINI and A. VICINO. Comparison of recurrence quantification methods for the analysis of temporal and spatial chaos. *Mathematical and Computer Modelling*, 2011, 53(7), 1535-1545.

112. MONTI, M., T. MEYER, C. TSCHUDIN and M. LUISE. Signal processing applied to chemically inspired communication protocols. In *IEEE International Conference on Communications (ICC)*. IEEE, 2012, p. 1144-1148.

113. MOORE, G. and E. HUBERT. Algorithms for constructing stable manifolds of stationary solutions. *IMA Journal of Numerical Analysis*, 1999, 19(3), 375-424.

114. MUIR, T. *A Treatise on the Theory of Determinants*. Courier Corporation, 2003.

115. NAN, X., Q. LI, D. QIU, Y. ZHAO, et al. Short-term wind speed syntheses correcting forecasting model and its application. *International Journal of Electrical Power \& Energy Systems*, 2013, 49, 264-268.

116. NAVICKAS, Z. and L. BIKULČIENĖ. Expressions of solutions of ordinary differential equations by standard functions. *Mathematical Modelling and Analysis*, 2006, 11(4), 399-412.

117. NEWMARK, N. M. A method of computation for structural dynamics. *Journal of Engineering Mechanics*, 1959, 85, 67-94.

118. NUSSE, H. E. and J. A. YORKE. *Dynamics: Numerical Explorations*. New York: Springer, 1998.

119. OLYAEI, A. A. and M. R. GHAZAVI. Stabilizing slider-crank mechanism with clearance joints. *Mechanism and Machine Theory*, 2012, 53, 17-29.

120. OLYAEI, A. A. and C. WU. Controlling chaos using a system of harmonic oscillators. *Physical Review E*, 2015, 91(1), 012920.

121. ORDONEZ, C., N. MOHANAM, C. GARCIA-ALVARADO, P. T. TOSIC, et al. Fast PCA computation in a DBMS with aggregate UDFs and LAPACK. In *Proceedings of the 21st ACM international conference on Information and knowledge management.* 2012, p. 2219-2223.

122. OSTLUND, S., D. RAND, J. SETHNA and E. SIGGIA. Universal properties of the transition from quasi-periodicity to chaos in dissipative systems. *Physica D: Nonlinear Phenomena*, 1983, 8(3), 303-342.

123. OTT, E., C. GREBOGI and J. A. YORKE. Controlling chaos. *Physical review letters*, 1990, 64(11), 1196.

124. PALIVONAITE, R. and M. RAGULSKIS. Short-term time series algebraic forecasting with internal smoothing. *Neurocomputing*, 2014, 127, 161-171.

125. PARK, H. and L. ELDEN. Matrix Rank Reduction for Data Analysis and Feature Extraction. 2003.

126. PEÑA, R., J. NÚÑEZ and A. MEDINA. Using a Newton method and LAPACK libraries to initialize electromagnetic transient simulations in power systems. *Simulation Modelling Practice and Theory*, 2014, 42, 12-18.

127. PIERAŃSKI, P. and J. MALECKI. Noisy precursors and resonant properties of the period-doubling modes in a nonlinear dynamical system. *Phys. Rev. A*, July, 1986, 34(1), 582-590.

128. PYRAGAS, K. Continuous control of chaos by self-controlling feedback. *Physics Letters A*, 1992, 170(6), 421-428.

129. PUSTILNIKOV, L. D. On Ulam's problem. *Theoretical and Mathematical Physics*, 1983, 57, 1035.

130. RAGULSKIS, M., K. LUKOSEVICIUTE, Z. NAVICKAS and R. PALIVONAITE. Short-term time series forecasting based on the identification of skeleton algebraic sequences. *Neurocomputing*, 2011, 74(10), 1735-1747.

131. RAGULSKIS, M. and Z. NAVICKAS. The rank of a sequence as an indicator of chaos in discrete nonlinear dynamical systems. *Communications in Nonlinear Science and Numerical Simulation*, 2011, 16(7), 2894-2906.

132. RAGULSKIS, M., Z. NAVICKAS, R. PALIVONAITE and M. LANDAUSKAS. Algebraic approach for the exploration of the onset of chaos in discrete nonlinear dynamical systems. *Communications in Nonlinear Science and Numerical Simulation*, 2012, 17(11), 4304-4315. ISSN 1007-5704.

133. ROBLEDO, A. Universal glassy dynamics at noise-perturbed onset of chaos: a route to ergodicity breakdown. *Physics Letters A*, 2004, 328(6), 467-472.

134. ROSA, C., M. J. CORREIA and P. C. RECH. Arnold tongues and quasiperiodicity in a prey-predator model. *Chaos, Solitons & Fractals*, 2009, 40(4), 2041-2046.

135. SAKTHIVEL, G. and S. RAJASEKAR. Diffusion dynamics near critical bifurcations in a nonlinearly damped pendulum system. *Communications in Nonlinear Science and Numerical Simulation*, 2012, 17(3), 1303-1311. ISSN 1007-5704.

136. SALAM, A. and D. WATKINS. Structured QR algorithms for Hamiltonian symmetric matrices. *Electronic Journal of Linear Algebra*, 2011, 22(1), 36.

137. SANDERS, J. A., F. VERHULST and J. A. MURDOCK. *Averaging methods in nonlinear dynamical systems*. Springer, 2007.

138. SAUER, T., J. A. YORKE and M. CASDAGLI. Embedology. *Journal of statistical Physics*, 1991, 65(3-4), 579-616. ISSN 0022-4715.

139. SCHILDER, F. and B. B. PECKHAM. Computing Arnold tongue scenarios. *Journal of Computational Physics*, 2007, 220(2), 932-951.

140. SHIH, J.-R., Y. HU, M.-C. HSIAO, M.-S. CHEN, et al. Securing M2M with post-quantum public-key cryptography. *Emerging and Selected Topics in Circuits and Systems, IEEE Journal on*, 2013, 3(1), 106-116.

141. SKALICKY, S., S. LOPEZ, M. LUKOWIAK, J. LETENDRE, et al. Linear algebra computations in heterogeneous systems. In *IEEE 24th International Conference on Application-Specific Systems, Architectures and Processors (ASAP)*. 2013, p. 273-276.

142. SRINATH, R., A. SARKAR and A. S. SEKHAR. Parametrically Excited Vibration in Rolling Element Bearings. In *INTER-NOISE and NOISE-CON Congress and Conference Proceedings*. Institute of Noise Control Engineering, 2014, vol. 249, p. 2987-2992.

143. STARZAK, M. E. *Mathematical methods in chemistry and physics*. Springer Science & Business Media, 2013. ISBN 148992082X.

144. STPICZYŃSKI, P. Fast solver for Toeplitz bidiagonal systems of linear equations. *Annales UMCS Sectio AI Informatica*, 2015, 1(1), 1-7.

145. STROGATZ, S. H. *Nonlinear dynamics and chaos: with applications to physics, biology, chemistry, and engineering*. Westview press, 2014.

146. TENNYSON, J. and S. C. FARANTOS. Routes to vibrational chaos in triatomic molecules. *Chemical physics*, 1985, 93(2), 237-244.

147. TONELLI, R. and M. CORADDU. Numerical study of the oscillatory convergence to the attractor at the edge of chaos. *The European Physical Journal B-Condensed Matter and Complex Systems*, 2006, 50(1), 355-359.

148. TRAVERSA, F. L. and F. BONANI. Oscillator noise: a nonlinear perturbative theory including orbital fluctuations and phase-orbital correlation. *Circuits and Systems I: Regular Papers, IEEE Transactions on*, 2011, 58(10), 2485-2497.

149. TRAVERSA, F. L. and F. BONANI. Improved harmonic balance implementation of Floquet analysis for nonlinear circuit simulation. *AEU-International Journal of Electronics and Communications*, 2012, 66(5), 357-363.

150. TREFETHEN, L. N. Pseudospectra of linear operators. *SIAM review*, 1997, 39(3), 383-406.

151. TREFETHEN, L. N. Computation of pseudospectra. *Acta Numerica*, 1, 1999, 8, 247-295. ISSN 1474-0508.

152. TREFETHEN, L. N. and D. BAU III. *Numerical linear algebra*. Siam, 1997.

153. ÜNAL, A. An algebraic criterion for the onset of chaos in nonlinear dynamical systems. *Nonlinear Analysis: Theory, Methods & Applications*, 1989, 13(7), 753-765.

154. V. L. KURAKIN, A. S. K., A. V. MIKHALEV and A. A. NECHAVEV. Linear complexity of polinear sequences. *Journal of Mathematical Sciences*, 1995, 76, 2793-2915.

155. VAN ZEE, F., R. VAN DE GEIJN and G. QUINTANA-ORTI. Restructuring the QR algorithm for performance. *ACM Trans. Math. Soft.. Submitted*, 2013.

156. VON BRENTANO, P. and N. ZAMFIR. On a measure of the complexity of nuclear states and the onset of chaos. *Physics Letters B*, 1992, 297(3), 219-222.

157. WANG, J., M.-M. HU, P. GE, P.-Y. REN, et al. A Forecasting Model for Short Term Tourist Arrival Based on the Empirical Mode Decomposition and Support Vector Regression. In *Proceedings of 2013 4th International Asia Conference on Industrial Engineering and Management Innovation (IEMI2013)*. 2014, p. 1009-1021.

158. WIESENFELD, K. and N. B. TUFILLARO. Suppression of period doubling in the dynamics of a bouncing ball. *Physica D: Nonlinear Phenomena*, May-June, 1987, 26(1-3), 321-335.

159. WRIGHT, T. G. and L. N. TREFETHEN. Pseudospectra of rectangular matrices. *IMA Journal of Numerical Analysis*, 2002, 22(4), 501-519.

160. WU, X. Is the Hamiltonian geometrical criterion for chaos always reliable? *Journal of Geometry and Physics*, 2009, 59(10), 1357-1362.

161. XIA, L. and Q. XUE-DONG. Mixed Programming of Fortran and C/C++ in Linux. *Modern Computer*, 2012, 5, 018.

162. ZASLAVSKY, G. M. The simplest case of a strange attractor. *Physics Letters A*, December, 1978, 69(3), 145-147.

LIST OF SCIENTIFIC PUBLICATIONS ON THE THEME OF THE DISSERTATION

Papers in Master List Journals of the Institute of Scientific Information (ISI)

1. Landauskas, Mantas; Ragulskis, Minvydas. A pseudo-stable structure in a completely invertible bouncer system // Nonlinear dynamics. Dordrecht : Springer. ISSN 0924-090X. 2014, vol. 78, iss. 3, p. 1629-1643. DOI: 10.1007/s11071-014-1546-3. [Science Citation Index Expanded (Web of Science); Compendex; SpringerLINK]. [IF: 2,419, AIF: 1,656 (E, 2013)]. [M.kr. 09P].
2. Ragulskis, Minvydas Kazys; Navickas, Zenonas; Palivonaitė, Rita; Landauskas, Mantas. Algebraic approach for the exploration of the onset of chaos in discrete nonlinear dynamical systems // Communications in Nonlinear Science and Numerical Simulation. Amsterdam : Elsevier Science. ISSN 1007-5704. 2012, Vol. 17, iss. 11, p. 4304-4315. [Science Citation Index Expanded (Web of Science)]. [IF: 2,773, AIF: 1,559 (E, 2012)]. [M.kr. 09P].
3. Landauskas, Mantas; Ragulskis, Minvydas Kazys. Clocking convergence to a stable limit cycle of a periodically driven nonlinear pendulum // Chaos. Melville, NY : American Institute of Physics. ISSN 1054-1500. 2012, Vol. 22, iss. 3, p. [1-7]. DOI: 10.1063/1.4748856. [Science Citation Index Expanded (Web of Science)]. [IF: 2,188, AIF: 1,386 (E, 2012)]. [M.kr. 09P].

Papers in Proceedings List of the Institute of Scientific Information

4. Landauskas, Mantas; Ragulskienė, Jūratė; Ragulskis, Minvydas. H-rank as a control tool for discrete dynamical systems // International conference of numerical analysis and applied mathematics (ICNAAM), Kos, Greece, September 19-25, 2012. Melville, NY : American Institute of Physics, 2012. (AIP Conference Proceedings, Vol. 1479, ISSN 0094-243X), ISBN 9780735410916. p. 2098-2101. DOI: 10.1063/1.4756604.
5. Landauskas, Mantas; Ragulskis, Minvydas. Clocking convergence to Arnold tongues - the H-rank approach // ICNAAM 2013 : 11th International Conference of Numerical Analysis and Applied Mathematics 2013, 21-27 September 2013, Rhodes, Greece : AIP proceedings. Melville, NY : American Institute of Physics, 2013. (AIP Conference Proceedings, Vol. 1558. pt. 1, ISSN 0094-243X), ISBN 9780735411845. p. 2457-2460. DOI: 10.1063/1.4826038.

Papers in journals indexed in other international databases

6. Navickas, Zenonas; Landauskas, Mantas; Šmidtaitė, Rasa; Ragulskis, Minvydas. The Ho-kalman model as a transformer of linear recurring sequences // Global journal of pure and applied mathematics. Delhi : Research India Publications. ISSN 0973-1768. 2015, vol. 11, no. 1, p. 99-119.

Papers in other peer-reviewed journals

7. Landauskas, Mantas; Ragulskis, Minvydas. Clocking convergence to Arnold tongues – the circle map revisited // Lietuvos matematikos rinkinys : Lietuvos matematikų draugijos darbai. Serija B / Lietuvos matematikų draugija, Vilniaus universitetas. Vilnius : Vilniaus universitetas. ISSN 0132-2818. 2012, t. 53, p. 54-59.

SL344. 2016-01-29, 15,5 leidyb. apsk. l. Tiražas 12 egz. Užsakymas 30.
Išleido Kauno technologijos universitetas, K. Donelaičio g. 73, 44249 Kaunas
Spausdino leidyklos „Technologija“ spaustuvė, Studentų g. 54, 51424 Kaunas